Colloidal Synthesis of I-III-VI Semiconductor Nanocrystals and Study of Their Optical Properties

DISSERTATION

Zur Erlangung des akademischen Grades

Doctor rerum naturalium

(Dr. rer. Nat.)

Vorgelegt

Dem Bereich Mathematik und Naturwissenschaften

Der Technischen Universität Dresden

Von

Ankita Bora

Geboren am 28. Dezember 1992 in Cinnamara, Jorhat (Assam)

Eingereicht am: 02.05.2023

Defense am: 21.07.2023

1. Gutachter: Prof. Dr. Alexander Eychmüller,
2. Gutachter: Prof. Dr. Stefan Kaskel

Die Dissertation wurde in der Zeit von Oktober 2019 bis Mai 2023 in der Professur für Physikalische Chemie angefertigt.

মা আৰু দেউতালৈ

(To my parents)

Acknowledgements

List of Abbreviations

acac⁻	acetylacetonate
ATR-FTIR	attenuated total reflectance Fourier-transform infrared spectroscopy
CE	cation exchange
CGSe	Cu-Ga-Se
CIS	Cu-In-S
CISe	Cu-In-Se
CZISe	Cu-Zn-In-Se
CZIS	Cu-Zn-In-S
DDT	1-dodecanethiol
DMF	dimethyl formamide
DOS	density of states
EDXS	energy-dispersive X-ray spectroscopy
fcc	face centered cubic
FWHM	full width at half maxima
HAADF-STEM	high-angle annular dark-field scanning TEM
HOMO	highest occupied molecular orbital
HSAB	hard soft acid base
ICP-OES	inductively coupled plasma-optical emission spectroscopy
LCAO	linear combination of atomic orbitals
LED	light emitting diode
LSC	luminescent solar concentrator
LUMO	lowest unoccupied molecular orbital
NC	nanocrystal
LSPR	localized surface plasmon resonance
MO	molecular orbital
NIR	near infrared
NPL	nanoplatelet
NS	nanosheet
ODE	octadecene
OlAm	oleylamine
PCE	power conversion efficiency

PL	photoluminescence
PLQY	photoluminescence quantum yield
QD	quantum dot
TBP	tri-n-butylphosphine
TEM	transmission electron microscopy
TOP	tri-n-octylphosphine
TOPO	tri-n-octyl phosphine oxide
TRPL	time-resolved photoluminescence
wrt	with respect to
XPS	X-ray photoelectron spectroscopy
XRD	X-Ray diffraction
0D	zero-dimensional
2D	two-dimensional
3D	three-dimensional

List of Figures

List of Tables

List of Chemicals

Chemical	Formula	Provider	Purity
Copper (II) acetylacetonate	$Cu(acac)_2$	Sigma-Aldrich	97%
Indium (III) acetate	$In(OAc)_3$	Sigma-Aldrich	99.99%
Se powder	Se	Sigma-Aldrich	99.99 %
Zinc (II) acetate	$Zn(OAc)_2$	Sigma-Aldrich	99.99 %
Ammonium sulfide solution	$(NH_4)_2S$	Sigma-Aldrich	20 wt.% in H_2O
1-Octadecene (ODE)	$C_{18}H_{36}$	Sigma-Aldrich	technical grade, 90%
Octylamine (OctAm)	$C_8H_{19}N$	Sigma-Aldrich	99%
Oleylamine (OlAm)	$C_{18}H_{37}N$	Sigma-Aldrich	70 %
1-Dodecanethiol (DDT)	$C_{12}H_{26}S$	Sigma-Aldrich	99%
Triethyloxonium tetratfluoroborate	Et_3OBF_4	Sigma-Aldrich	≥ 97%
Zinc bromide	$ZnBr_2$	Sigma-Aldrich	99.99%
Tri-n-octylphosphine (TOP)	$C_{24}H_{51}OP$	VWR	97%
Hexane	C_6H_{14}	VWR	97%
N-methylformamide (MFA)	C_2H_5NO	Acros Organics	99%
Extra dry acetonitrile	C_2H_3N	Acros Organics	99.9%
1-Butylamine	$C_4H_{11}N$	Alfa Aesar	99%
Dimethylformamide (DMF)	C_3H_7NO	Fischer Chemicals	analytical reagent grade
Chloroform	$CHCl_3$	Sigma-Aldrich	
Indium (III) chloride	$InCl_3$	Sigma Aldrich	99.99%
Zinc 2-ethylhexanoate	$C_{16}H_{30}O_4Zn$	Sigma Aldrich	17-19% Zn
Sulfur	S	Sigma Aldrich	99.98%
Tetrakis (acetonitrile)copper (I) hexafluorphosphate	$[Cu(CH_3CN)_4]PF_6$	Sigma Aldrich	97%
Zinc diethyldithiocarbamate	$Zn(DDTC)_2$	Sigma Aldrich	99%
Zinc acetate dihydrate	$Zn(OAc)_2 \cdot 2H_2O$	Sigma Aldrich	≥99%
Thiourea	CH_4N_2S	Sigma Aldrich	95%
Triethylene glycol dimethyl ether	$C_8H_{18}O_4$	Sigma Aldrich	99%
Formamide (FA)	CH_3NO	Fischer Chemicals	99.5%
Tetrahydrofuran (THF)	C_4H_8O	Acros Organics	99.9%
Methanol	CH_3OH	VWR	99.9%
Toluene	$C_6H_5CH_3$	Sigma-Aldrich	≥ 99.7 %
Tetrachloroethylene (TCE)	C_2Cl_4	Sigma-Aldrich	99%

Table of Contents

1 Introduction

The study of nanocrystals (NCs) has been a very intriguing topic for scientists for quite some time and it has emerged as one of the most fascinating fields of modern science. Since 1857, when Faraday chemically synthesized the first Au NCs, the appealing properties, particularly tuneable colours of nano-sized crystals, have gained significant attention.[1] Historically, in the medieval era, the colour tuneability of crystals was used to impart different colours in stained glass which can be seen today in church windows. Baking glass with gold and silver salts at different temperatures and for different times yielded stained glass with different colours. The origin of these colours was later attributed to the phenomenon of localized surface plasmon resonance (LSPR) arising due to the collective oscillation of conduction band electrons at the surface of the metal nanoparticles.[2] The progress in the field of microscopy and the development of transmission electron microscopy (TEM), and thus the ability to view these small crystals on the nanometer scale and determine their accurate sizes, became another important contributor to the advancements in this field and gradually modern nanoscience took rapid pace in the early 1980s. The discovery of the most appealing feature of semiconductor NCs, the 'quantum confinement effect' leading to the ability to tune the electronic energy states and optical transitions by adjusting their size and shape, has paved the way for further research advances in this field.[1] To this end, pioneer work was done by A. Ekimov,[3] A. Efros,[4] T. Itoh,[5] and co-workers in the study of the size effects of the optical spectra of CuCl NCs embedded in alkali-halide matrices. Additionally, Brus et al. provided experimental and theoretical evidence of the quantum size effect of the properties of CdS NCs.[6, 7] Synthetic and experimental studies on semiconductor NCs received even more exposure after 1993 when Bawendi group introduced a tool for precise control of the size of colloidal NCs known as the 'hot-injection approach', wherein monodisperse CdSe NCs were synthesized at high reaction temperatures in high boiling organic solvents.[8] Since then, continuous research has been dedicated to unfolding new horizons of this field. Interesting optical and electronic properties have been harvested in a plethora of applications, while new classes of compounds and morphologies have also been studied. While there existed a gap between research advances in this field and commercialisation of the applications developed in the laboratory on a small scale, a breach of this gap was accomplished when Samsung introduced semiconductor NCs as colour converters in their devices. They use InP-based NCs acting as a light-emitting material in their QLED TV screens. *Figure 1.1* depicts a photo of an exhibition held by Samsung showcasing the origin of

quantum dots (QDs) using stained glass and Samsung SUHD TV screens, which is an apt representation of size tuneable optical properties of NCs, harvested in various applications over time. After this breakthrough by Samsung, continuous fundamental research to achieve better shape and size distribution, and enhanced luminescence properties of the NCs continues in this field. Along with this, attempts to employ semiconductor NCs in a plethora of applications in various fields, e.g., in photovoltaics, optoelectronics, sensing, and bioimaging, is a topic of rigorous research.[9] For instance, solar cells with high power conversion efficiencies (PCE) have been fabricated using semiconductor NCs.[1, 10] Along with it, NCs have been used as luminescent solar concentrators (LSCs), being integrated with solar cells, result in higher PCE.[11, 12] Biological applications of NCs constitute using them as fluorescent probes for various tasks of biological research that include in vivo-imaging and cell-labelling.[13]

Figure 1.1 *'Origin of quantum dots' an art piece displayed by Samsung in collaboration with German scientists where they used 45 Samsung's SUHD TVs with QD display and 9000 shards of stained glass.[14]*

Although a wide range of semiconductor NCs have been synthesized successfully, the ones studied most extensively are the II–VI and IV–VI semiconductors, such as CdSe and PbS NCs, which have been harvested for optoelectronic and biomedical applications.[10, 15] Despite the establishment of well-developed synthetic routes to these NCs and their appealing properties, the toxicity of cadmium and lead imposes serious limitations for using them in some particular applications, especially those involving exposure to biological systems.[16] This requires exploring alternatives to these materials that can replicate the optical properties of the II-VI and IV-VI NCs and potentially replace them in various applications.[17] This has led to a

considerable effort to find alternative luminescent and photoactive metal chalcogenide compounds consisting of earth-abundant and less toxic elements. Amongst several options, I−III−VI$_2$ semiconductor QDs have proven themselves as outstanding candidates to serve as an alternative to their more toxic counterparts.[13, 18] Their benign composition makes them best fit to be used in biological systems for bioimaging and drug delivery, which is one of the major applications of semiconductor nanoparticles.[19]

Various approaches to prepare semiconductor NCs have been explored, with direct synthesis emerging as the most used route to II-VI-based NCs with the advantages of its simple setup and rapid reaction rate.[20] However, in the case of I-III-VI NCs, the presence of multiple reactive species generated from several reactive precursors with varied reactivity poses a problem for the use of the direct synthesis method.[21, 22] Synthesis of I-III-VI-based NCs with this pathway suffers from inhomogeneities in size and shape of the ensemble along with the formation of by-products in addition to the desired particles. An alternative to the direct synthesis is the partial cation exchange (CE) pathway, wherein first binary NCs are synthesized, which then serve as the host template for incoming cations, which replace some of the host cations, leading to multicomponent ternary or quaternary semiconductor NCs with composition depending on the number of guest cations introduced.[23] Employing this strategy also enables the realization of metastable crystal phases and off-stoichiometric compositions of NCs, which are not possible through direct methods, in which thermodynamically favoured phases and compositions are achieved.[24] This route of CE presents a feasible pathway for the synthesis of I-III-VI-based NCs with better size and shape control, opening the door to unique compositions and crystal phases.

Along with size and composition, the dimensionality/morphology of NCs has emerged as a useful tool for tuning their optical properties. Thus, research on II-VI group of semiconductor NCs has shown that change in dimensionality of the NCs, i.e., the variation from zero-dimensional (0D) through one-dimensional (1D) to two-dimensional (2D) can lead to unique optical properties due to variation of electronic confinement of exciton and band gaps in these structures. Such anisotropic shapes arise from the growth restricted (or facilitated) in certain crystallographic directions. One major example of unique optical properties of 2D NCs is the extremely narrow photoluminescence (PL) spectra of CdSe nanoplatelets (NPLs), as compared to 0D CdSe QDs.[25] However, as compared to the II-VI family, 2D I-III-VI NCs are scarcely studied and very few of them exhibit PL. Therefore, exploration of synthetic methods

to obtain 2D NCs of I-III-VI compounds might reveal intriguing optical properties and, therefore, should be investigated.

This thesis focuses on the development of synthetic strategies for morphologically vivid Cu-In-S- (CIS) and Cu-In-Se- (CISe) based NCs belonging to the I-III-VI family of semiconductors, which can be utilized as a less toxic alternative in various applications. The work is divided into three parts. In the first part, the development of a synthetic pathway for quaternary Cu-Zn-In-Se (CZISe) NCs, starting with binary $Cu_{2-x}Se$ NCs via partial CE was carried out. This work aims at eliminating inhomogeneities in the size and composition of the NCs synthesized, to result in narrow PL spectra. Also, a one-step simultaneous injection of In- and Zn-precursors offers the possibility of enhancing PL intensity instead of an additional step of the shell growth, which is generally required for higher PL intensities in this class of materials. Additionally, surface modification of the synthesized NCs, wherein the long-chain organic ligands on the parent NCs are replaced with shorter ligands, was carried out. This is a necessary tool for enhancing carrier mobility, which in fact is essential for all electronic applications of NC-solids in, e.g., solar cells and photodetectors. Moving to different morphologies, the second part of the thesis deals with the anisotropic growth of Cu-Zn-In-S (CZIS) NPLs, with the aim of synthesizing high-quality emissive 2D materials of this class of compounds. A seed-mediated approach was adopted for the synthesis of CIS NPLs followed by a subsequent partial CE with Zn to enhance the PL intensity. Synthetic strategies were adopted to achieve a better shape control of the NPLs, aiming to obtain unstacked NPLs. An additional step of the shell overcoating with ZnS was carried out to increase the PL intensity and improve their stability. The third part of the thesis is dedicated to the development of a synthetic approach to CZISe NPLs with the aim of pushing their PL further into the near infrared (NIR) range, which can be achieved due to the narrower band gap of bulk CISe, as compared to bulk CIS. CISe-based 2D NCs exhibiting PL are not reported yet and thus synthesizing these NIR-emitting NCs is of particular interest. Extending PL into the NIR range enables increasing the scope of these NCs since NIR emitters are of significant use in biological systems and telecommunications. Thus, this thesis offers synthetic strategies for three materials belonging to the I-III-VI group of semiconductors, exhibiting distinct optical properties, namely, CZISe NCs, CZIS NPLs, and CZISe NPLs.

2   Fundamental Concepts of Semiconductor Nanocrystals

Abstract*: Semiconductor nanoscience is an interesting branch of science that involves interdisciplinary knowledge of both physical and chemical aspects of materials. Colloidal synthesis of the NCs requires knowledge of organometallic chemistry, while understanding photophysical mechanisms and consequently device fabrication using these NCs require knowledge of semiconductor physics and engineering. In this chapter, fundamental concepts of semiconductor NCs necessary in the context of this thesis are explained.*

2.1   Band structure of semiconductor NCs and quantum confinement

Semiconductor NCs are small crystals with dimensions in the range of 1-100 nm with discrete energy levels, as opposed to their bulk counterparts.[26] They can be considered as intermediate species between small molecules and bulk crystals. An energy band of a bulk semiconductor is made up of a multitude of molecular orbitals (MO) formed from the linear combination of corresponding atomic orbitals (LCAO). Although discrete, the energy difference between these MOs in a bulk semiconductor is negligible, thus forming a continuum. The energy difference between the filled low-energy band (valence band) and the empty high-energy band (conduction band) is called the *band gap* (E_g).[27] As and when the size of the crystal decreases and it enters the *nano regime* the energy difference between individual MOs as well as the band gap increases. In general, this phenomenon can be termed as the *quantum confinement effect.* [28] *Figure 2.1* depicts the evolution of band structures on moving from bulk structured to nanostructured crystals.
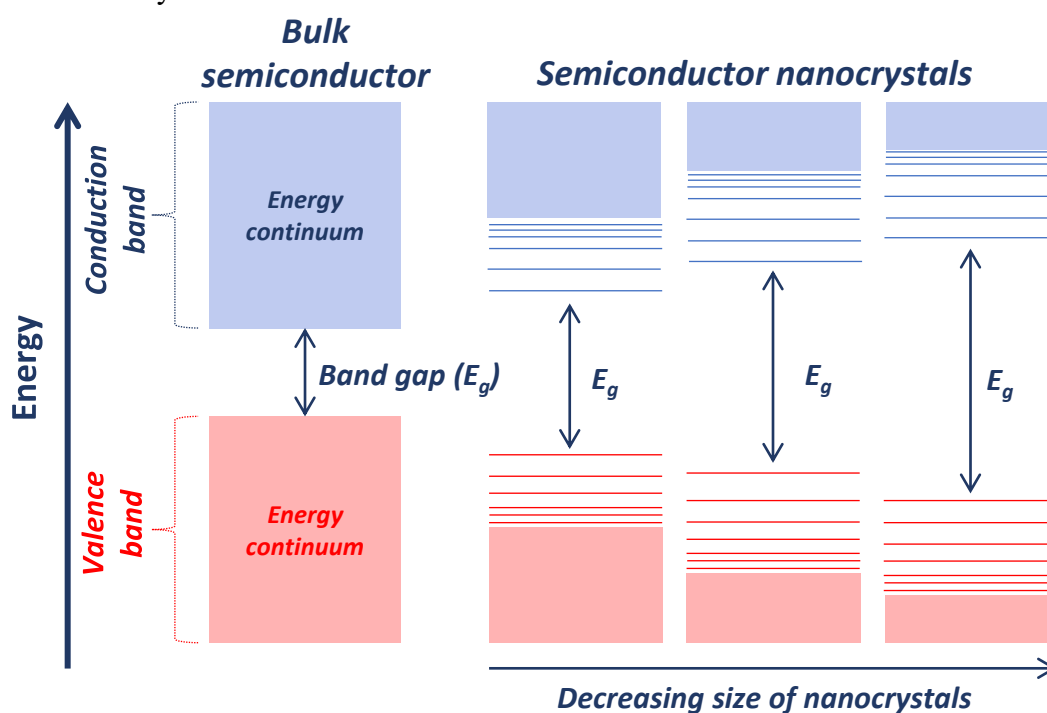
Figure 2.1 Variation of band structure from bulk to nanosized semiconductors.

Upon absorption of a photon, an electron from the valence band in a semiconductor can be excited to the conduction band. The resulting electron and hole are electrostatically attracted to each other, forming an electron-hole pair called an *exciton*. An exciton occupies a finite space in the crystal, which varies depending on the material, and the radius of this allowed space is called the *exciton Bohr radius (a_B)*.[27] It is described as,

$$a_B = \frac{\epsilon_0 \epsilon_r h^2}{\pi \mu e^2} \qquad (1)$$

where ϵ_0 *and* ϵ_r are the permittivity of free space and relative permittivity of the semiconductor, μ is the reduced mass of the electron and hole, and e is the charge of the electron. Thus, the Bohr radius is dependent on the effective mass of the electron and hole and consequently is different for different materials. Therefore, the nano regimes of different materials are also different. Quantum confinement effect becomes more significant as the NC size approaches the Bohr radius. At particle size much larger than a_B, the exciton is not confined and so the continuum in the bands remains. When the particle size is less than the a_B, the exciton becomes confined, and the energy gap increases.[28] For a spherical crystal with radius R, the band gap ($E_g(R)$) is described by the *Brus equation*, and this also demonstrates the size effect of quantum confinement. It is described as,

$$E_g(R) = E_g + \frac{h^2}{8R^2}\left(\frac{1}{m_e} + \frac{1}{m_h}\right) - \frac{1.8e^2}{4\pi\epsilon_0\epsilon_r R} \qquad (2)$$

where E_g is the bulk band gap, h is the Plank's constant, m_e and m_h are the effective mass of electron and hole, ϵ_r is the bulk optical dielectric constant or relative permittivity, and ϵ_0 is the permittivity of free space. According to the second term of the equation, the band gap is inversely proportional to R^2 and increases as the size decreases. The third term shows the opposite relation, which is due to the increase in Coulombic interaction. However, when R is in the nano regime of a few nanometers, the second term dominates, and the band gap increases as the R or size of the crystal decreases. Thus, this behavior is described by a particle in a box model, wherein the energy level spacing increases as the length of the box decreases. The expressions discussed above are applicable for spherical NCs (or QDs), which are spatially confined in all three dimensions and are known as 0D NCs. In addition to this, in practice, various shapes of NCs have been explored leading to different spatial confinement. In the case of quantum confinement within two dimensions (such as in nanorods),

unrestricted carrier motion is allowed in only one direction, i.e., along the length, and the exciton is confined in the remaining directions. Nanorods, nanotubes, and nanowires are examples of 2D confinement known as 1D NCs. The third case is quantum confinement and quantization within only one dimension (*quantum well*) with unrestricted carrier motion in two other dimensions. NPLs, and nanosheets (NSs) are examples of 1D confinement and are known as 2D NCs. In bulk materials, the exciton is not confined, and free motion is allowed in all dimensions and consequently these are *three-dimensional materials*. Dimensionality can also be explained in terms of *density of states* (DOS), as depicted in *Figure 2.2*.[29] DOS describes the number of electronic states available per given energy. For a bulk material, wherein excitons are free to move in all dimensions, a 3D DOS can be derived which is proportional to $\sqrt{E}$. *Figure 2.2a* shows the variation of DOS with energy for bulk materials. In 2D nano systems, the exciton is free to move in two dimensions while being confined in one dimension, which results in a DOS which is independent of energy ($\propto E^0 = constant$). If there are several confined states within a 2D quantum well, then the DOS is a step function, as depicted in *Figure 2.2b*. For quantum rods and wires (1D), the exciton is confined in two dimensions, while having free motion along their length, resulting in 1D DOS with inverse square energy dependence. *Figure 2.2c* shows this dependence which reveals that the DOS increases in fixed amounts and decreases between every step. Lastly, a 0D QD with excitons confined in all three dimensions exhibits 0D DOS with states allowed at only certain energy levels.[27] *Figure 2.2d* shows a DOS for a 0D system which depicts a variation like that of a δ function.
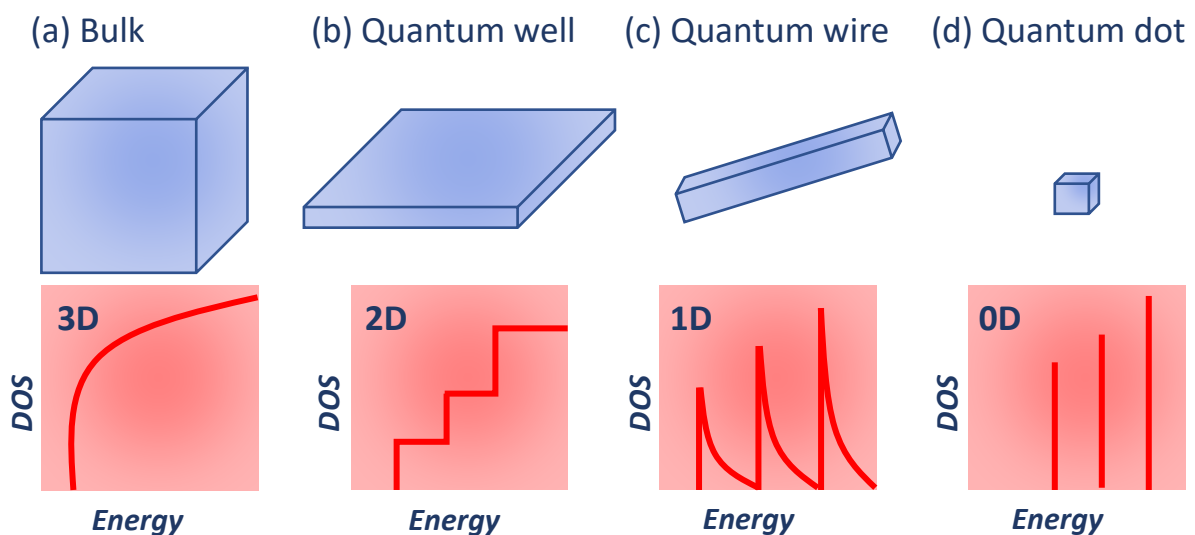
Figure 2.2 *DOS for 3D bulk (a), 2D quantum well (b), 1D quantum wire (c), and 0D QD (d).*

The difference in quantum confinement for 0D, 1D, and 2D NCs reflects its shape dependence. If an exciton is confined within all dimensions, then its restricted motion results in higher quantization of energy levels leading to an increase in the band gap. Consequently, as the confinement is restricted to only one or two dimensions, the free movement of exciton increases, thus leading to a decrease in the band gap.[30] *Figure 2.3* shows the variation of the band gap of CdSe QDs, quantum wells, and quantum wires with the length of the confined dimension. Considering a fixed length of the confined dimension, i.e., d_B, the band gap for the QD (0D) is the widest followed by quantum wire (1D), and then by quantum well (2D).[28]
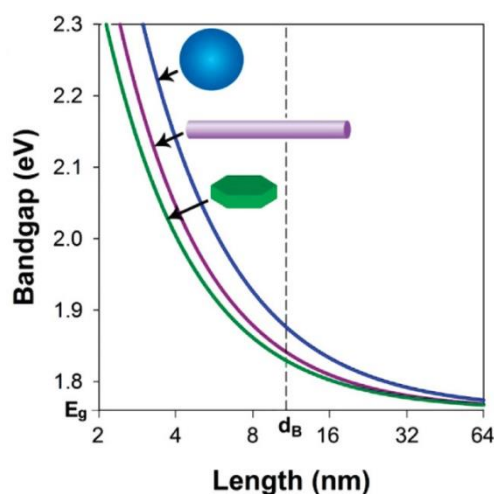
Figure 2.3 *Variation of band gap for NCs with different confinements. Reprinted from ref. 28 with permission. Copyright © 2010, American Chemical Society.*

2.2   Optical properties of semiconductor NCs

The study of optical properties of semiconductor NCs translates from the inherent properties of bulk semiconductors. The filled valence band with electrons and empty conduction band separated by the band gap are the ground state of a semiconductor. Absorption of a photon with energy greater than the band gap results in the excitation of an electron to the conduction band, leaving a positively charged hole in the valence band. This is known as *photoexcitation*. Optical absorption processes in semiconductors obey the conservation of energy and momentum, and consequently, transitions can be direct or indirect depending on the material. Following conservation of momentum, a photon (k_{hv}) is considered to have almost zero momentum and consequently the sum of the individual momenta of electron (k_e) and hole (k_h) at the moment of the formation of electron-hole pair should be zero, i.e., $\Delta k = k_e + k_h = k_{hv} \approx 0$.[31] In such cases, the electron can simply be excited from the valence band to the conduction band by absorption of a portion of energy equal to or greater than the band gap value. Semiconductors

in which such direct transitions are allowed are known as *direct band semiconductors*. In another situation, direct transitions can be forbidden, and in this case a phonon is involved in momentum conservation. These are known as *indirect band semiconductors,* in which the electron absorbs the photon and resides in a virtual state till a phonon of appropriate energy is available for the scattering process.[27] *Figure 2.4* illustrates the differences in electronic band structures of a direct and indirect semiconductor.
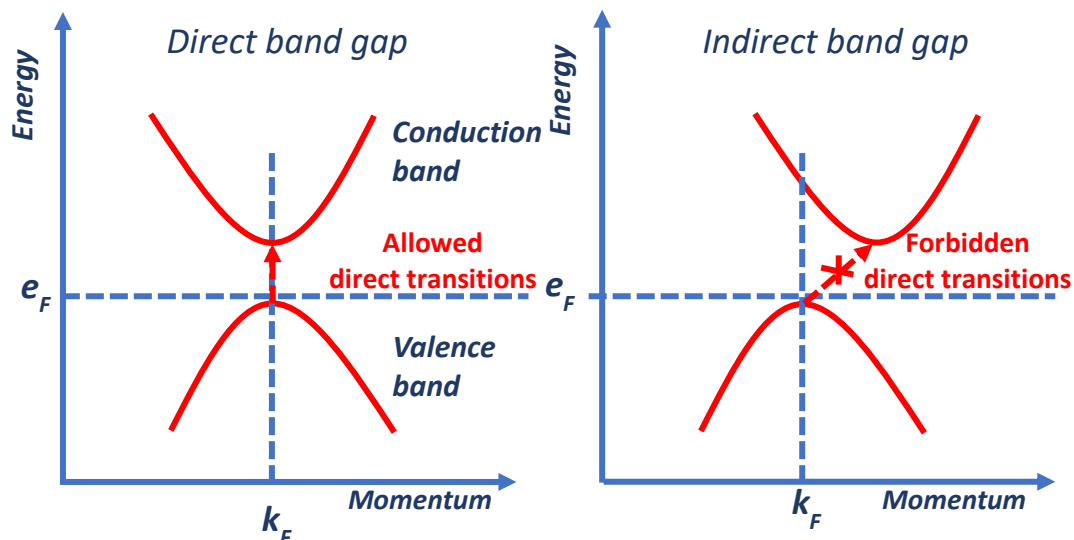
Figure 2.4 *Direct and indirect semiconductors. Adapted from ref. 31 with permission. Copyright © 1999, Springer-Verlag Berlin Heidelberg. e_F is the Fermi level of the semiconductor and k_F is the Fermi wave vector.*

In direct band gap semiconductor NCs, e.g., CdSe QDs once the electron is excited (purple arrow in *Figure 2.5a*) to the conduction band, its fate can be different according to the pathway taken. In cases when the energy absorbed by the electron is higher than the band gap, the electron is excited to higher levels of the conduction band, and subsequently this excited (hot) electron tends to lower its energy by transitioning into lower energy levels of the conduction band. This process, taking place without the dissipation of photon energy, is known as *cooling* or *relaxation (*green arrow in *Figure 2.5a)*. When an excited electron dissipates energy and reunites with a hole, the process is known as *recombination*. In cases when an excited electron in the conduction band edge travels back to a hole at the valence band edge, with the release of photon energy giving rise to photon-induced luminescence, commonly known as *photoluminescence* (PL), the electron-hole recombination is known as *radiative recombination (Figure 2.5b)*. The energy of the emitted photons most often is less than the excitation photon giving rise to *Stokes shift,* which is the energy difference in absorption and PL maxima. In some cases, however, it can also happen

that the electron does not travel to the valence band directly but proceeds through an intermediate trap state introduced due to lattice vacancies or impurities. The trapped electron can then finally recombine with the valence band hole which occurs without photon emission and, therefore, is known as *non-radiative recombination (Figure 2.5c)*. This trap-assisted non-radiative recombination is also known as *Shockley-Read-Hall recombination*. Intermediate energy states can also act as trap centers for a hole, and in this case an excited electron can recombine with the trapped hole non-radiatively. Along with lattice vacancies, surface trap states, which are represented by defects introduced due to missing surface atoms or dangling bonds on some surface atoms can also serve as the origin of non-radiative decay pathways. As the crystal becomes smaller, the fraction of atoms located on the surface increases and so does the number of unbound atoms, introducing surface traps, which, if lie within the band gap, act as centers of non-radiative recombination.[32, 33] In addition to non-radiative recombination, trap states in some cases can also be associated with radiative recombination i.e., with the release of photon energy, resulting in trap emission. E.g., in very small CdSe NCs, this trap state emission appears as a separate broad peak in their PL spectra, which arises from Se^{2-} rich facets weakly bound to basic ligands leading to a poor passivation of trap states.[28] *Auger recombination* is another non-radiative process involving three carriers wherein the energy dissipated in the process of an electron-hole recombination is provided to another free carrier. In the Auger recombination depicted in *Figure 2.5d*, the energy released from the electron-hole recombination is provided to another electron, which then can then excite to higher energy levels in the conduction band, and finally cool down to the conduction band edge by the release of thermal energy. Adopting synthetic strategies which facilitate the elimination of non-radiative recombination pathways can lead to enhanced photon emission, most often quantified with a *photoluminescence quantum yield* (PLQY), which essentially is the ratio between number of photons emitted and absorbed. Thus, PLQY is not an intrinsic property of a material but depends on the conditions and parameters adopted for the synthesis of particular NCs.
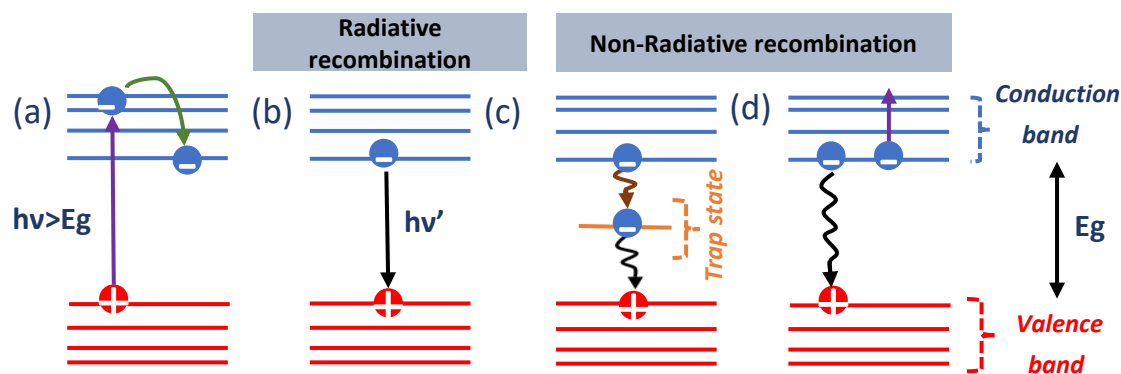
Figure 2.5 *Processes of excitation (purple arrow) and relaxation (green arrow) (a), radiative recombination (b), trap-assisted recombination (c), Auger recombination (d). v is the frequency of absorbed light and v' is the frequency of emitted light.*

For semiconductor NCs, the size dependency of optical properties is a very important aspect that is still being studied and exploited for various applications. This arises due to quantum confinement discussed in *Section 2.1,* which means that the band gap widens as the size of a NC decreases. Consequently, absorption and emission exhibit a blue shift, i.e., a shift to higher energy or shorter wavelengths. Thus, proper control of the size of NCs enables tuning their optical properties over a wide range of wavelengths, as shown in *Figure 2.6* for CdSe/ZnS core/shell NCs. In accordance with the size effect, the CdSe/ZnS NCs reported by Rogach et al. exhibit blue emission for the smallest size of 1.7 nm, and the largest CdSe/ZnS NCs with a size of 5 nm exhibit red PL.[34] Size tuneable optical properties have also been explored in the case of I-III-VI semiconductor NCs, which is the main class of materials studied in this thesis. For example, Allen et al. reported the synthesis of CISe QDs in the size range of 2 nm to 3.5 nm with a shift of PL from red to NIR range.[35] Li et al. synthesized CIS/ZnS QDs with emission in the range of 590 nm to 900 nm for an increase in QD size from 2 nm to 4 nm.[16] Exploitation of size tuneability of optical band gaps of semiconductor NCs has made them suitable light emitting materials in several of applications including light emitting diodes (LEDs) and biological markers which constitute some of the major applications of semiconductor NCs.[32]
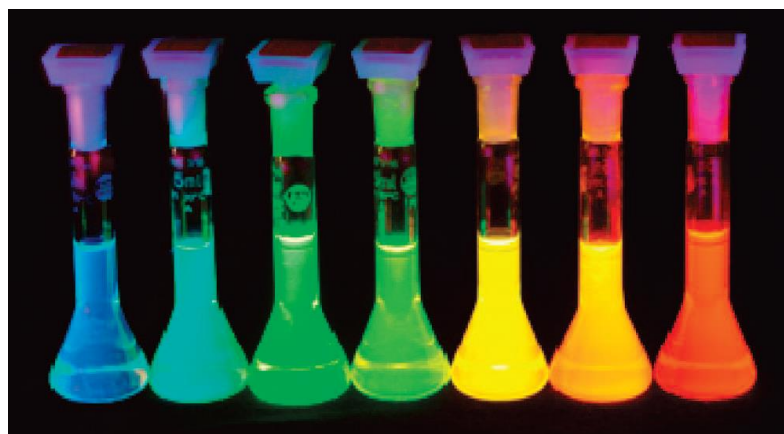
Figure 2.6*. Size-tuneable optical properties of CdSe/ZnS core/shell NCs. Reprinted from ref. 34 with permission. Copyright ©2002 WILEY-VCH Verlag GmbH & Co. KGaA, Weinheim.*

2.3   Core/shell NC heterostructures

As discussed in the previous section, the surface of a NC can have crystal lattice defects or/and dangling bonds. These unshared atomic orbitals give rise to energy levels within the band gap

of the NC. The intermediate levels within the band gap of the NC are detrimental to their PLQY, since these can act as centers for non-radiative recombination of the exciton. Thus, it becomes very important to heal these defects on the surface of the NC and one strategic way of achieving this is the overgrowth of a shell of a different semiconductor material around the NC core. This growth of a shell serves two purposes: first is passivating the dangling bonds on the surface and healing crystal lattice defects, thus leading to PLQY enhancement; and second is improving stability to the NC, protecting it from aerial oxidation and photodegradation.[16, 36] Depending on the energy offsets between the highest occupied molecular orbital (HOMO) and lowest unoccupied molecular orbital (LUMO) of the two semiconductor materials in a core/shell system, there can be differences in carrier localization between the core and the shell material, leading to three different types of their arrangement, i.e., *Type I*, *Quasi Type II*, and *Type II*.[37]

A Type I system consists of a shell material that has a wider band gap than the core material and, in this case, the exciton is completely confined within the core, as schematized in *Figure 2.7*. Examples of this type of core/shell system include CdSe/ZnS and CIS/ZnS, wherein ZnS acts as a shell material with a wide band gap of 3.4 eV[16] which is larger than the band gap of CdSe (1.76 eV)[38] and CIS (1.5 eV)[20]. A quasi Type II core/shell system is characterized by partial delocalization of the exciton to the shell. Although CdSe/CdS couple can be considered as a Type I band alignment, the energy offset is too small for the complete confinement of the exciton in the core, leading to a partial leakage of the electron wave function to the shell material, while the hole remains confined in the core, as depicted in *Figure 2.7* for quasi Type II core/shell system. Thus, in this case, one charge carrier is localized and the other is delocalized over the entire heterostructure. This kind of a core/shell system facilitates the tuning of its optical properties with a variation of the shell thickness. Other examples of this type of alignment include ZnSe/CdSe and PbSe/CdSe NCs.[39, 40] A staggered band arrangement of core and shell material belongs to the Type II core/shell system, wherein the band gap of the core/shell system is narrower than any of the individual band gaps of the participating materials. This type of band arrangement leads to a spatially indirect exciton, meaning the hole and the electron are localized separately in the core and the shell. Example of this type of heterostructure include CdTe/CdSe and CdSe/ZnTe NCs.[41, 42] In this case, overgrowth of the shell leads to narrowing of the band gap, consequently resulting in a red shift of the emission wavelength and thus enabling the tuning of the optical properties within a broader range than the range obtained with either of the constituting materials.[37]
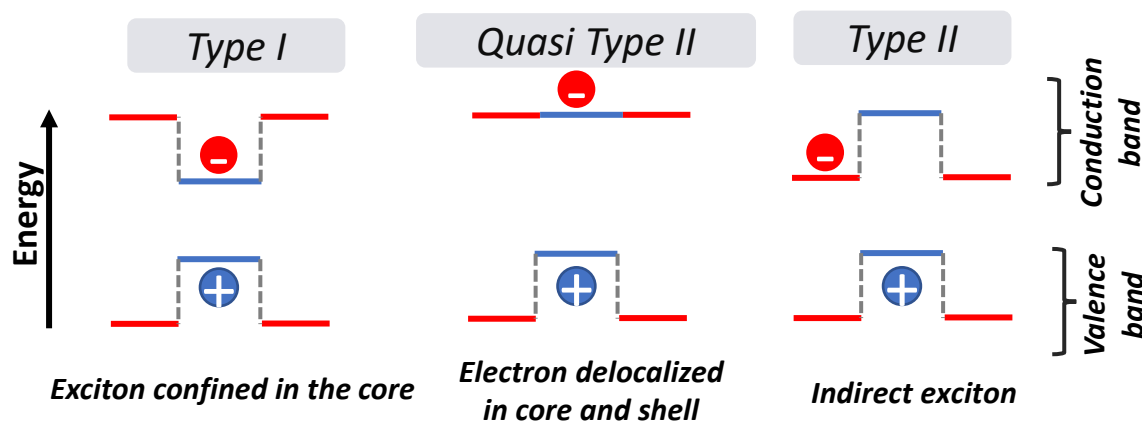
Figure 2.7 Exciton confinement in Type I, Quasi Type II and Type II core/shell heterostructures. Adapted from ref. 37 with permission. Copyright © 2010, Royal Society of Chemistry.

Appropriate selection of a shell material also necessitates the consideration of lattice constants of both materials, such that the lattice mismatch between the materials involved should be minimized. The lattice constant of a semiconductor describes the spacing of atoms in a crystal. If it so happens that the lattice constants of both materials are very different, then the mismatching positions of atoms at the interface can cause an interfacial strain leading to defect states which again is detrimental for the PLQY of the NCs. Thus, both energy offsets and lattice mismatch between the two materials are taken into consideration while designing a core/shell system. For example, ZnS is a suitable shell material for CdSe to construct a Type I system, which enables its PLQY enhancement, since ZnS has a broader band gap of 3.4 eV than CdSe with 1.76 eV. However, they have a lattice mismatch of 12% which prevents the growth of ZnS shell thicker than 2-3 monolayers. While CdS has a narrower band gap (2.42 eV) than ZnS, its lattice mismatch with CdSe is much lesser, 3.9%, which makes it also a suitable shell material.[37] Thus, a bargain between the both parameters should be made in view of the desired properties to obtain a suitable core/shell heterostructure. In addition to this, other factors like the reactivity of precursors, surface chemistry of core NCs, and reaction conditions all play significant roles in the growth of the shell, and thus all must carefully be optimized.[36]

2.4 Colloidal synthesis of semiconductor NCs

Several methods and techniques for the synthesis of NCs, like chemical vapor deposition, molecular beam epitaxy, laser ablation, magnetron sputtering, etc., have been developed.[26] Amongst the variety of synthetic approaches available, colloidal synthesis of semiconductor NCs, wherein they are grown in a liquid phase and then can be dispersed in suitable solvents with the aid of proper surface ligands or surfactants is a simple and facile method, which does

not require complex and expensive equipment and can be implemented in nearly any chemistry lab.[1, 43] As opposed to colloidal synthesis in the aqueous phase, colloidal synthesis in organic phase allows for the use of high boiling organic solvents, which, in turn, enables tuneability of reaction temperature over a wide range, thus resulting in fine-tuning of the NC size and shape. In the following, the colloidal synthesis of semiconductor NCs in the organic phase will be discussed. This method yields NCs constituting an inorganic core and the outer organic ligand shell, as illustrated in *Figure 2.8.*

Inner inorganic core
Origin of electronic and optical properties

Outer protective ligand shell
- ***Provides colloidal stability***
- ***Passivate trap states***
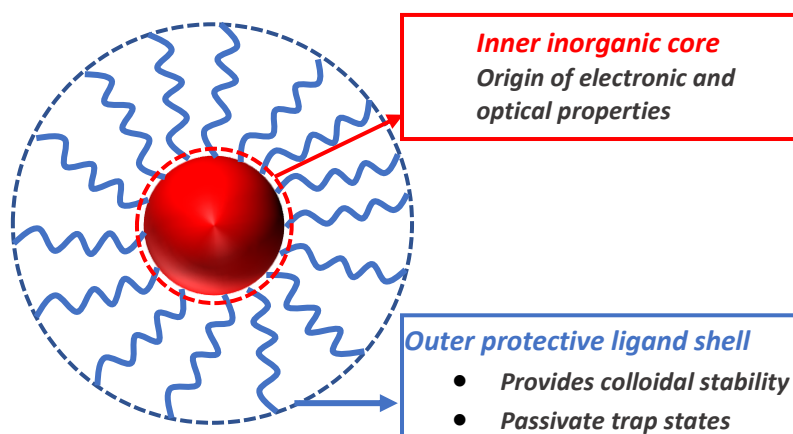
Figure 2.8 *A colloidal semiconductor NC with inorganic core and ligand shell.*

Thus, the design of a synthesis of colloidal NCs will include considerations of the inorganic core, the ligand shell, and the interaction between the core and the ligand shell. Various semiconductor materials belonging to metal pnictides of I_3-V, II_3-V_2, and III-V groups (e.g., InP, InAs), metal chalcogenides of II-VI group (CdSe, CdS, ZnSe),[44-46] IV-VI group (PbSe, PbS),[47, 48] and I-III-VI group (CIS, CISe),[49-51] and metal/organo lead halide perovskites of I–IV–VII group (CsPbBr$_3$)[52] have constituted the inorganic core of colloidal NCs. This inorganic core is responsible for the varied optical and electronic properties of the NCs, which are also indeed affected by the ligands on the surface. An organic ligand typically contains a polar head, which has an affinity to the NC surface and a non-polar organic chain. The combined roles of a ligand in the synthesis include providing a medium for the reactants to form molecular precursors, stabilizing NCs in colloidal form through sufficient repulsive forces (steric or electrostatic), and passivating the trap states on the core surface, which act as centres for non-radiative recombination (see *Section 2.2*).[43] Thus, careful choice of an appropriate ligand or a mixture of ligands, playing the mentioned roles, leads to the formation of high-quality NCs.

In early syntheses, the ligand and NC surface interacted with a dative bond between neutral electron donor with metal atoms, e.g., the case of interaction of tri-n-octyl phosphine oxide (TOPO) molecules with surface cadmium atoms of CdSe. However, in due course of time other molecules which act as neutral acceptors, bound ion pairs, and ionic species have been used as surface ligands. Taking this covalent bond classification in the field of NCs, Owen grouped ligands in terms of the number of electrons involved in bonding and the electron donor or acceptor nature of ligands, as illustrated in *Figure 2.9*.[53] Here, ligands acting as neutral two-electron donors with a lone electron pair that coordinates surface metal atoms are termed as *L-type ligands* (e.g., phosphines, phosphine oxides, and amines). *X-type ligands* in a neutral form are species that have an odd number of valence-shell electrons, requiring one electron from the NC surface site to form a two-electron covalent bond. Examples of X-type ligands include carboxylates (RCOO⁻), thiolates (RS⁻), and phosphonates (RPO(OH)O⁻), and inorganic ions (such as Cl^-, $InCl_4^-$, AsS_3^{3-}), or bound ion pairs (for example $NEt_4^+I^-$). *Z-type ligands* (e.g., $Pb(OOCR)_2$ and $CdCl_2$) are neutral electron acceptors with an unoccupied orbital that coordinates surface nonmetal atoms.[53, 54]

X-type
Terminates lattice

L-type
Neutral-donor

X-type
Bound ion pair

Z-type
Neutral-acceptor

X= RCO_2^-, Cl^-, RS^- etc.
L= PR_3, NH_2R etc.
MX_2= $Cd(O_2CR)_2$, $CdCl_2$, $Pb(SCN)_2$ etc.
$[X]^-[HB]^+$= $[Cl]^-[HPBu_3]^+$,$[S]^{2-}2[H_4N]^+$, $[In_2Se_4]^{2-}2[N_2H_5]^+$ etc.

● = Metal *(Cd, Pb etc.)*
● = Chalcogenide *(S, Se etc.)*
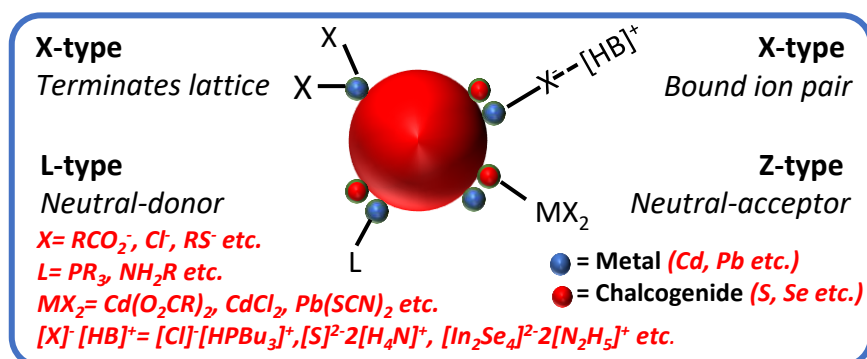
Figure 2.9 *Types of ligands. Adapted from ref. 54 with permission. Copyright © 2013, American Chemical Society.*

Another important aspect of the interaction between the ligand and the core, a ligand's propensity for a particular core material, can be understood through *Pearson's hard and soft acid base theory (HSAB)*.[55-57] According to this theory, Lewis acids and bases can be classified into hard and soft ones, where soft-soft and hard-hard acid-base interactions are favoured over soft-hard acid-base interactions. Thus, ligands that can be considered as Lewis bases, and cations on the surface of the NC core considered as Lewis acids will also interact according to this theory. This theory is explained in more detail in *Section 2.5*.

Growth mechanism of colloidal semiconductor NCs

To understand the formation mechanism of semiconductor NCs, one must first understand the phenomenon of nucleation and growth. *Nucleation* can be described as the assembly of a few atoms to form a small crystal that does not disintegrate into free atoms and is kinetically stable, or alternatively it is a thermodynamic system that tends to minimize its Gibbs free energy by attracting more and more monomer species. This process can also be interpreted as overcoming a certain energy barrier. Upon nucleation, the Gibbs free energy change for spherical NCs, assuming that it is an isotropic crystal without facets, can be expressed as the sum of the energetic gain due to bond formation and the total surface energy.

$$\Delta G = -\frac{4}{3}\pi r^3 |\Delta G_v| + 4\pi r^2 \gamma \quad (3)$$

Here, r is the radius of the nuclei formed, G_v is the Gibbs bulk free energy per unit volume and γ is the surface free energy per unit area. As shown in *Figure 2.10*, ΔG_c corresponds to a maximum in the plot of Gibbs free energy change vs. radius of the nucleus, which is essentially the activation energy that must be overcome for nucleation to occur.[43] The maximum ΔG_c is attained at a certain radius which is known as the *minimum critical radius* denoted by r_c in *Figure 2.10* and corresponds to the minimum size of the nucleus above which it can enter the growth stage while nuclei smaller than this size will redissolve into atoms in solution.
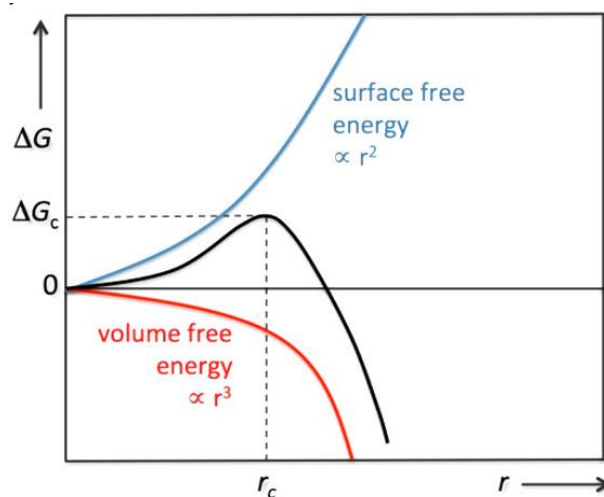
Figure 2.10 *Plot of Gibbs free energy vs. radius of nucleus. Reprinted from ref. 43 with permission. Copyright © 2016, American Chemical Society.*

After the nucleation, the *growth* phase can be described as the actual deposition of monomers on the growing crystal. For the addition of monomers, first, they must be transported to the surface of the NC, and second, they must react with the NC surface. The first process occurs through diffusion and thus the rate can be dominated by the diffusion coefficient D,

whereas the rate of the second process can be defined as simply the rate of reaction between monomers and the NC surface. In general, an excess of precursors is used to initiate growth and, therefore, the effect of diffusion can be neglected, and the rate solely depends on the rate of the reaction between free monomers and the NC surface. In this case, the growth regime is called a *reaction-controlled growth rate*.[26] During this time the growth rate is proportional to the surface area of the particle and during this stage a decrease in relative size distribution occurs. The growth rate can be expressed as,

$$\frac{dr}{dt} = kV_m(S_b - S_r) \quad (4)$$

Here, k is the reaction rate constant, V_m is the molar volume of the solid, S_b is the bulk concentration of the monomer, and S_r is the solubility of the particle as a function of its radius r. However, after some time, when the concentration of monomers decreases, the rate also becomes dependent on the diffusion of the monomers, and when this becomes the rate-limiting step then the growth rate is a '*diffusion-controlled growth rate*'.[26] The growth rate according to *Fick's law of diffusion* is given as

$$\frac{dr}{dt} = DV_m \left(\frac{1}{r} + \frac{1}{\delta}\right)(S_b - S_r) \quad (5)$$

where D is the diffusion coefficient and δ is the thickness of the diffusion layer.
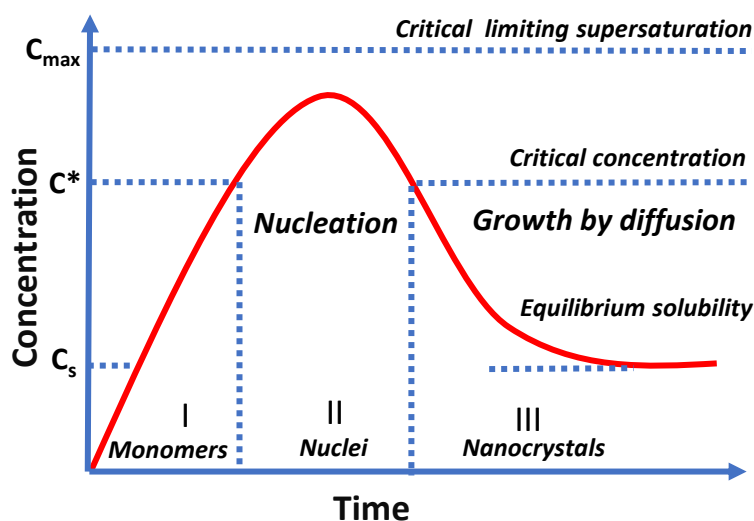
Figure 2.11 *LaMer model depicting the three phases of the NC formation. Adapted from ref. 26 with permission. Copyright © 2014, Royal Society of Chemistry.*

The relation between nucleation and growth of colloidal NCs was given by *LaMer* and is depicted in *Figure 2.11*.[58] According to this model, the formation process of NCs can be

divided into three phases: in the first phase, the concentration of monomers increases due to the availability of a large amount of precursors or change in reaction parameters. As and when the monomer concentration reaches the critical concentration C*, the second phase, nucleation, starts, wherein nuclei are formed by aggregation of monomers. The nucleation process terminates when the concentration of monomers falls below the critical concentration i.e., C*. The subsequent stage is the growth of the NCs by monomer deposition on existing nuclei until the monomer concentration decreases below the critical level. However, in actual scenario new nuclei other than the preexisting ones, undergoing the growth, can also be formed, which in turn can lead to a broad size distribution of NCs. One drawback of the LaMer model is that it does not take into consideration the evolution of size distribution during the growth. For diffusion-controlled growth rate, Sugimoto established the relation between the size distribution and growth rate with considerations of particle solubility based on the *Gibbs-Thomson equation,* and the model is depicted in *Figure 2.12a* .[59] It can be inferred from this model that when the size of the NCs is slightly larger than the critical radius then the smaller particles grow faster than the larger ones resulting in *focusing* of the size distribution. On monomer depletion after a certain period of time, the critical radius becomes larger than the average size. In this case, smaller particles start shrinking and eventually redissolve into monomers, which can then redeposit on larger particles. The dissolved monomers can deposit on smaller crystals resulting in larger particles. To prevent these particles from agglomeration, the addition of appropriate stabilizing agents becomes necessary, which ensures the appropriate steric repulsion between adjacent NCs to impart them colloidal stability in a solvent. This leads to *defocusing* of size distribution also known as '*Ostwald ripening*' which is a common contributor to the broad size distribution.[60] Experimental investigation of the relation of size distribution of NCs with growth rate for the synthesis of CdSe and InAs NCs was done by Alivisatos and coworkers, which is illustrated in *Figure 2.12b*.[61] According to their findings during the initial event of injection, after a certain time a narrow size distribution is observed (focusing), when the size of the particles is slightly larger than the critical radius. As the monomers are used up and the growth rate is diffusion controlled, resulting in low supersaturation of monomers, the size distribution broadens, resulting in defocusing of size distribution. A second event of injection of precursors after the broadening of the size distribution resulted in a second focusing regime. Thus, for size focusing it is essential to keep the average size slightly larger than the critical radius, which can be attained by a high supersaturation of monomers.
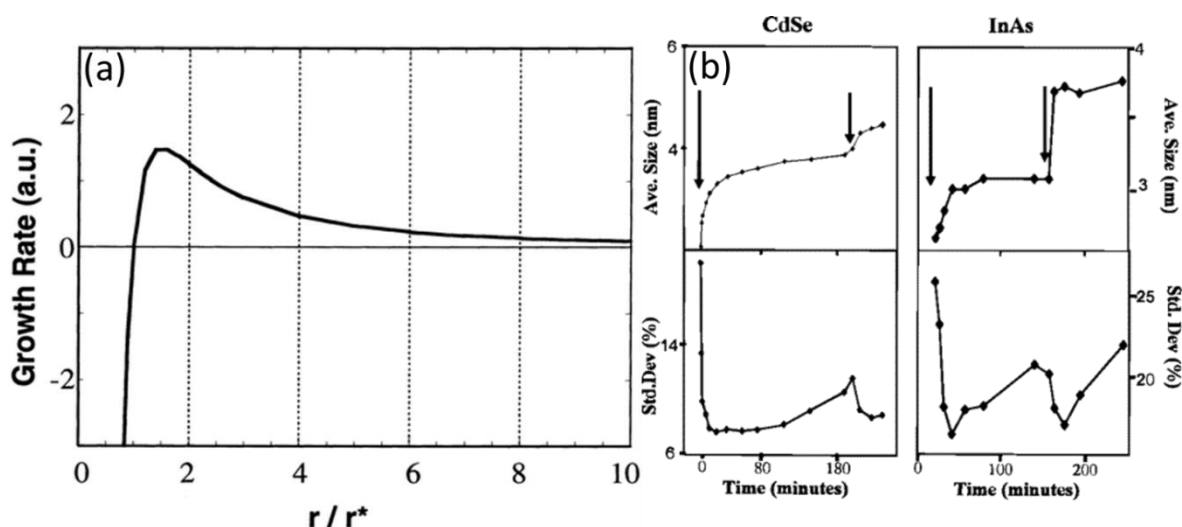
Figure 2.12 *Sugimoto model (a), size distribution of CdSe and InAs NCs with two injections of precursors denoted by arrows (b). Reprinted from ref. 61 with permission. Copyright © 1998, American Chemical Society.*

Hot-injection and heat-up methods of the NC synthesis

While size and shape distribution of NCs are dependent on several factors, including reaction temperature and time, reactivity and concentration of precursors, solvents, and surfactants used, the separation of the nucleation and the growth is the most effective pathway for obtaining a narrow size distribution, according to LaMer.[43] Separation in the nucleation and growth phases can be obtained by two methods of high-temperature synthesis, which facilitate the growth of monodisperse NCs: *hot-injection* and *heat-up* methods. In the hot-injection approach, separation of nucleation and growth is achieved through a 'nucleation burst', wherein the concentration of the monomers rapidly increases above the nucleation threshold on rapid injection of precursors at a high temperature. Most of these reactions are carried out in the presence of high-boiling organic solvents, like TOPO, tri-n-octylphosphine (TOP), 1-octadecene (ODE), alkane amines, alkanethiols, etc.[26, 32] This method was introduced first by Murray et al. in 1993 for the synthesis of considerably monodisperse cadmium chalcogenide NCs.[8] Organometallic cadmium precursor and chalcogenide precursors were prepared in high-boiling solvents of TOP and TOPO. Monodisperse CdSe(Te) particles were obtained by rapid injection of cadmium precursors into hot solvents at 300°C. This synthesis paved the way to the synthesis of monodisperse colloidal semiconductor NCs of the II-VI family and since then multiple reports with narrow size distribution and high PLQY have been published.

Consequently, the hot-injection method was adopted for I-III-VI semiconductor NCs by various researchers. Some of the early reports of the synthesis were given in 2008.[62-64] E.g.,

Allen et al. reported the synthesis of CISe NCs by heating metal halides in TOP and oleylamine (OlAm) to 200-280°C followed by injection of bis(trimethylsilyl)selenide.[35] Tang et al. also reported the synthesis of CISe, Cu-Ga-Se (CGSe), and Cu-In-Ga-Se (CIGSe) NCs, using a similar hot-injection approach.[65] As opposed to the hot-injection method, in the heat-up approach supersaturation of nucleation is achieved by in-situ formation of reactive species by increasing the temperature. Here, the precursors have a lower reactivity at low temperatures and upon reaching a particular temperature, a nucleation burst is attained, since the reactivity of the precursors increases at this temperature. Monodisperse high-quality CdSe NCs synthesized via heat-up method were reported by Cao et al.[44] Several reports on heat-up method are also available for I-III-VI NCs in which CIS(Se) NCs with various morphology and composition have been synthesized[16, 49-51] However, as compared to binary II-VI NCs, I-III-VI NCs synthesized via heat-up or hot-injection suffer from several drawbacks. Due to the complex multiple component system, wherein various cations involved have different reactivities with the chalcogen, additional by-products form and inhomogeneities in size arise, affecting shape and composition of the ensemble of the NCs.[21, 24, 66] An alternative synthesis pathway known as *cation exchange* (CE) discussed in the next section provides a suitable way of tackling the above mentioned drawbacks of the direct synthesis of I-III-VI-based semiconductor NCs.

2.5 Cation exchange

Since the above-discussed hot-injection and heat-up methods generally involve the reaction between all molecular precursors in one pot at the same time, they are termed as a direct synthesis. Over the years, it has enabled astonishing control over the NC size and shape and has been proven to be the best fit for obtaining binary II-VI and IV-VI semiconductor NCs.[21, 44] However, the urge to explore NCs with new morphologies, crystal phases, and compositions rises, facing limitations imposed by direct methods for obtaining such new materials. To overcome these limits, post-synthetic CE has emerged during last two decades as a fascinating alternative method for developing NCs, which would otherwise not have been possible through direct synthesis.[23, 24, 67] CE is a simple ion exchange reaction wherein the host cations of a template NC are replaced by guest incoming cations, while preserving the initial structure and anion sublattice of the crystal. The possibility of a complementary anion exchange is lowered in this process due to the larger size and low diffusivity of anions in a crystal lattice of the majority of metal chalcogenides.[24] When it comes to multicomponent synthesis of ternary and quaternary compositions of I-III-VI-based NCs, this method becomes significantly

advantageous, since their direct synthesis has various drawbacks, mainly inhomogeneous composition, size, and shape distribution of the NC ensemble. For example, in the synthesis of CISe, Cu^+ being a soft acid has a higher tendency to react with soft base Se^{2-}, as compared to the hard acid In^{3+}. This leads to the formation of $Cu_{2-x}Se$ first in the direct synthesis of CISe, multiplying the possibility of formation of additional by-products.[21, 68, 69]

The feasibility and outcome of CE largely depend on the thermodynamic and kinetic factors driving the reaction. The thermodynamic feasibility of a CE reaction can be estimated by taking into account the thermodynamic stability of reactant and product phases as well as the solvation of the cations in the solvent or ligating environment.[67] To understand the thermodynamics of a CE reaction, an ideal reaction involving monovalent cations can be described, as schematized in *Figure 2.13*. From this scheme, it can be inferred that an overall energy balance and resultant feasibility of such an ion exchange reaction can be determined, if the dissociation and association energies of A-X and B-X crystals and desolvation and solvation energies of B^+ and A^+ cations are known. Dissociation and association energies of a crystal can be defined in terms of *lattice energy* and *surface energy*, and it aids in estimating the thermodynamic stability of reactant and product phases. Lattice energy is the energy required for breaking a crystal into ions at absolute zero temperature. Thus, a higher lattice energy would mean a greater stability of a crystal, thus making it more difficult to dissociate. Consequently, the higher lattice energy of the product phase than the reactant phase would drive the process in the forward direction. Lattice energy (ΔH_{latt}) can be expressed as

$$\Delta H_{latt} = \frac{NMz_i z_j e^2}{r^+ r^-}\left(1 - \frac{1}{n}\right) \qquad (6)$$

Here, N is Avogadro's number, z_i and z_j are the integral charges of the ions, e is the electron charge, r^+ and r^- are the radii of cations and anions, respectively, n is the Born exponent and M is the Madelung constant. Thus, lattice energy depends on the charges and the radii of ions involved. Additionally, M in equation 6 is related to the spatial position of ions and thus this also makes the ΔH_{latt} dependent on the crystal structure. Consequently, this value will be different for different allotropes of the same material and its estimation becomes difficult, especially for metastable phases. When the calculation of lattice energies for a material is not possible, then the association and dissociation energies can be derived from the bond dissociation energies of the crystals. Another aspect of association and dissociation energies is the surface energies of the NCs. Upon nanostructuring, the surface-to-volume ratio largely increases, and this is reflected as an increase in surface energy in NCs, as compared to the bulk

surface energies. However, estimation of the surface energies is difficult since it is dependent on various factors, like the ligating environment and the chemical structure of different facets of the NC available for bonding with the surface ligands.[23]

$$A - X \quad + \quad B^+ \quad \longrightarrow \quad B - X \quad + \quad A^+$$

Desolvation   Solvation

Dissociation   Association
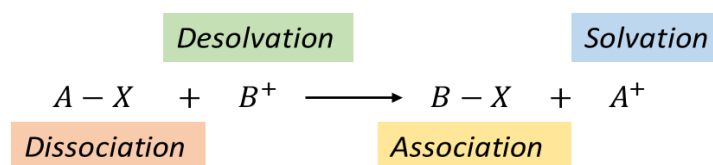
Figure 2.13 *Cation exchange reaction involving monovalent cations.*

Desolvation and solvation of the cations are another thermodynamic aspect that drives the CE reaction. These strongly depend on the solvating/ ligating environment of the solution in which the CE reaction takes place. A thermodynamic preference of an ion for a CE reaction in terms of lattice energy and entropy can be reversed under the influence of preferential ligation in solution. Preferential ligation or a ligand's affinity towards an ion can be understood by a qualitative concept of the HSAB principle proposed by Pearson.[55-57] According to this principle, Lewis acids and bases can be classified based on their hardness (η) into soft and hard acids and bases. Soft bases contain donor atoms with high polarizability and low electronegativity, while hard bases contain donor atoms with low polarizability and high electronegativity. Cations with a low positive charge and large size can be classified as soft acids, while cations with high charge and small size can be classified as hard acids. The HSAB principle also suggests the preferential interaction between soft acids with soft bases (soft-soft interaction) and likewise hard acids with hard bases (hard-hard interaction). Thus, the degree of hardness can work as a qualitative indicator of preferential cation binding with various ligands, which in turn can predict the outcome of a CE reaction.[70] This principle has been exploited to strategize many CE reactions in which the CE pathway can vary depending on the ligand environment, i.e., the presence of soft base or hard base. Cu-, Pb-, and Ag-chalcogenides contain Cu^+, Pb^{2+}, and Ag^+ cations which are soft acids, and their exchange with hard acids like Cd^{2+}, In^{3+}, and Zn^{2+} can be facilitated with the presence of a soft base in solution. It will preferentially bind with the soft cations leading to their extraction from the lattice, thereby facilitating the entry of the hard acids into the lattice. Soft bases, like tertiary phosphines[21, 71, 72] and carboxylates[73-75] have been widely exploited to enable these exchanges. Consequently, the opposite reaction, i.e., the exchange of hard acids like Cd^{2+} from chalcogenides with soft acids like Pb^{2+} can be facilitated in the presence of hard bases like alkylamines.[23, 76]

	Borderline	**Soft**
Acid	Cd^{2+}, In^{3+}, Ga^{3+} Fe^{3+}, Co^{3+}, Al^{3+} Sn^{4+}, Si^{4+} Mn^{2+}, Fe^{2+}	Cu^{2+} Zn^{2+} Sn^{2+} Ni^{2+} Co^{2+}	Cu^+, Ag^+ Au^+, Hg^+ Pb^{2+}, Pd^{2+} Pt^{2+}, Pt^{4+}
Base	OAc^-, Cl^- $acac^-$, NO_3^- OH^-, H_2O NH_3, $R\text{-}NH_2$	Br^- SO_3^{2-} N_3^- C_5H_5N	I^-, S^{2-} Se^{2-}, Te^{2-} DDT, TBP TOPO, TOP

Figure 2.14 *Classification of hard and soft acids and bases commonly used in semiconductor NC synthesis. Adapted from ref. 70 with permission. Copyright © 2017, American Chemical Society.*

While thermodynamic considerations offer a guide for determining the feasibility of a CE reaction, many of these reactions take place through non-equilibrium states and their outcome is kinetically controlled. The kinetic factors, determining the feasibility of a CE reaction are the activation barrier, rate of ion substitution at the surface, and rate of ion diffusion.[23] For colloidal NCs, the rate of ion substitution at the surface is faster than the rate of ion diffusion in the solid crystal. Thus, this solid-state ion diffusion in most cases is the rate-limiting step and determines the fate of a CE reaction. Its rate is governed by several factors, including the presence of vacancies and the possibility of diffusion through interstitial sites. These possibilities provide alternate routes of ion diffusion increasing its feasibility within the crystal.[23] Varying rates of diffusivity of ions and the miscibility of product and reactant phases results in various heterostructures obtained via CE which are represented in *Figure 2.15*.
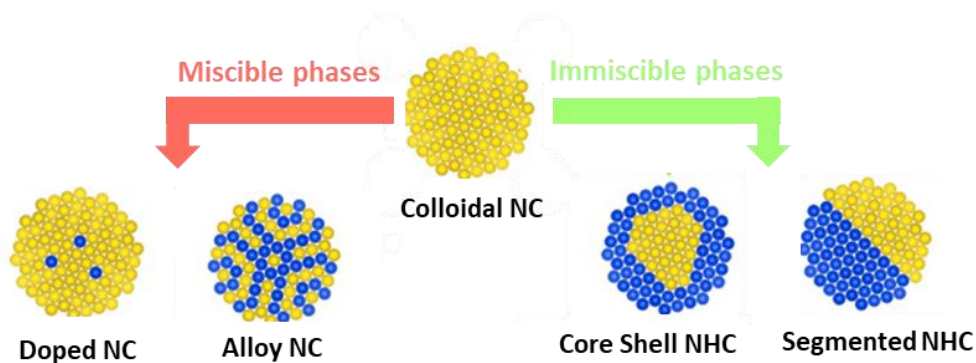
Figure 2.15 *Various possibilities of heterostructures via CE. Reprinted from ref. 23 with permission. Copyright © 2016, American Chemical Society.*

Thus, CE has been proven to be a powerful tool for developing a diverse pool of semiconductor NCs, including metastable crystal phases, unique morphologies, doped NCs, multi-compositional alloyed structures, and heterostructures which would not have been otherwise possible, using conventional direct synthesis methods.[24] Most attractive aspect of CE is the ability to attain metastable compositions and phases mostly by the preservation of the initial crystal phase and shape during the exchange. For instance, Li et al. demonstrated the preservation of the shape and crystal structure of a series of initial CdSe NCs with different morphologies and crystal structures after two sequential CE reactions. They carried out the first CE with Cu^+ to obtain Cu_2Se and thereafter with Zn^{2+} to synthesize ZnSe NCs with the same morphology and crystal phase as the starting NCs.[77] Along with complete exchange, partial CE has been instrumental in the synthesis of various ternary and quaternary compositions. Starting with $Cu_{2-x}S(Se)$ this approach has enabled substantial control over the size and shape of CIS,[68] CISe,[21] CZISe(Se),[20] and CZSSe[22] NCs. Inherently copper selenide(sulfide) can contain a large number of vacancies and this in turn boosts the exchange.[69]

2.6 Anisotropic growth of colloidal semiconductor NCs

Over the years along with 0D growth, 2D growth of NCs has been implemented leading to the development of differently shaped NPLs and NSs. 2D growth results in larger lateral dimensions, as compared to the thickness of the crystal, in some cases leading to a strong carrier confinement in one dimension, which may in turn exhibit unique optoelectronic properties. Owing to this, 2D NCs have been explored rigorously in recent years. By the thermodynamic aspect that a NC will always tend to minimize its total surface energy and surface area, the preferred shape of a material could theoretically be predicted from Wulff's construction.[78, 79] However, instead of the total surface energy, the equilibrium shape of a NC is determined by crystalline facets with minimum surface energy and their crystallographic orientation. Therefore, NCs with different facets might prefer different shapes and due to asymmetric bond strength and symmetry reasons they might also prefer to grow in one or two dimensions, resulting in anisotropic shapes such as nanorods and NPLs. However, during detailed investigations of the NC growth, it was also found that NCs can be synthesized in shapes other than their thermodynamically favored equilibrium shape.[78, 80] This growth proceeds through kinetically favored non-equilibrium conditions, which can be achieved via the manipulation of synthesis parameters. The shape, size, and crystal structure of the initial nuclei formed play a very important role in the determination of the NC shape. Non-equilibrium conditions lead to the formation of defects and polycrystalline nuclei, which then can introduce anisotropic

growth of the crystal leading to the formation of 2D NCs. This is termed *defect-induced anisotropy* and is one of the driving forces for breaking symmetry in a face-centered cubic (fcc) NC.[81]

Kinetic effects, like growth rate, also play an important role in shape control. During slow growth rate due to lower reaction temperature or slow addition of precursors, crystal growth proceeds by minimizing the energy of unfavorable facets via preferential growth along this facet, resulting in expression of low energy of facets.[81] On the other hand, when the growth rate is fast there is no preferential growth along any facet thus enabling the survival of high energy facets. Ligands can play a significant role in altering this NC growth direction, thus making anisotropic shapes available and this is known as *ligand-induced anisotropy*. This can occur through selective capping of certain facets of a growing NC with appropriate ligands, which then hinders their growth, as compared to others, thus leading to the 2D shapes. This effect is termed *chemical poisoning*. E.g., during the synthesis of CdSe NCs the presence of strong ligands, such as TOP and TOPO which have a strong affinity to surface cadmium ions on all facets, leads to a similar growth rate of all facets, resulting in a spherical shape of the particles.[82] This can be altered by adding phosphonic acid, which hinders the growth in the c axis of wurtzite lattice, leading to the formation of rod-shaped NCs.

Another approach for triggering anisotropic growth through ligands is the *soft template approach*. Long-chain organic ligands like alkylamines can dissolve metal salts like cadmium halides, forming ordered layers composed of metal salts and alkylamine.[81] This lamellar precursor can then serve as a soft template for 2D growth of a NC. Such a soft template approach was adopted by Son et al.[83] and Lui et al.[84] wherein they employed lamellar amine bilayers formed by dissolution of cadmium salts in alkylamine as templates for the synthesis of lamellar $(CdSe)_{13}$ nanoclusters which could then be transformed to 2D NSs or quantum belts respectively. Unbundling of these lamellar structures by addition of amines or sonication further resulted in individual 2D structures. The reaction temperature plays an important role in shape control using this approach, because beyond a certain temperature these ligand assemblies can decompose and no longer act as soft templates facilitating anisotropic growth. This method was employed to produce CdQ (Q= S/Se/Te),[85-87] ZnS,[88] as well as CuS[89] 2D NCs.

Another mechanism of anisotropic growth known as *oriented attachment* involves the reorganization of small individual NCs, such that they share a common crystallographic orientation.[90] This mechanism consists of several steps which involve the diffusion of small NCs to the vicinity of each other followed by a realignment of the adjacent NCs to decrease

the grain-grain boundary energy followed by desorption of ligands at the interface and the formation of a new crystal.[91] Weller and coworkers reported the synthesis of ultrathin PbS NSs via oriented attachment of small PbS NCs along the reactive {110} facet followed by reconstruction to result in flat surfaces.[92] The 2D growth took place explicitly in the presence of chloroalkanes according to pathway B and C depicted in *Figure 2.16*. In this case, oriented attachment led to 2D sheets with the assistance of an assembly of oleic acid ligands on the {100} facet that hindered the 3D growth. In the absence of chlorine containing co-solvents NS formation was not observed and instead larger 0D PbS NCs were observed as depicted in pathway A in *Figure 2.16*.
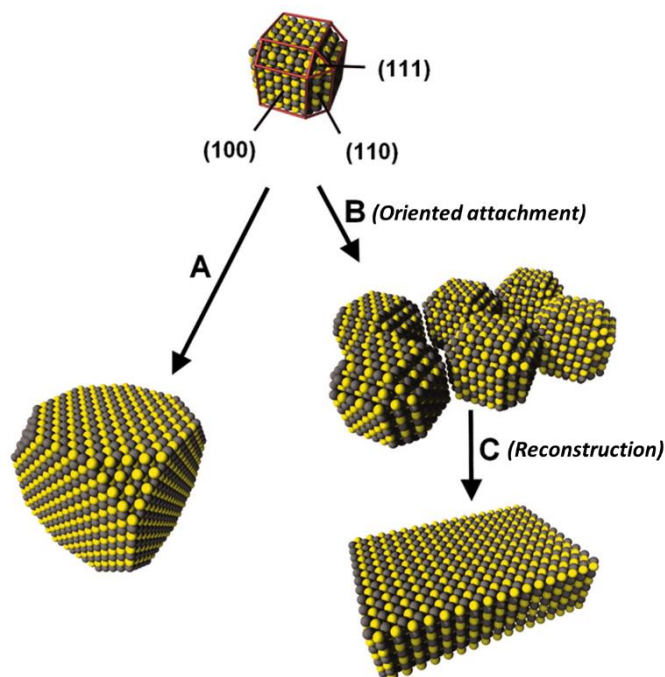
Figure 2.16 *Formation of PbS NSs via oriented attachment. Reprinted from ref. 92 with permission. Copyright © 2010, The American Association for the Advancement of Science.*

3 I-III-VI-Group-based Semiconductor Nanocrystals

Abstract: *Amidst a broad range of semiconductor NCs that are studied, this thesis delves into the study of I-III-VI-group-based semiconductor NCs. In this family, Cu-chalcogenide-based NCs, particularly CIS(Se)-based NCs, are of utmost importance. This chapter is dedicated to the description of synthetic advances carried out on the widely studied CIS(Se) NCs, including emerging 2D CIS(Se) NCs. Additionally, general characteristic optical properties of this class of materials and underlying mechanisms are also discussed.*

Most studied semiconductor NCs with exemplary optical properties, and narrow size and shape distribution belong to the II-VI or IV-VI groups of semiconductors. While these NCs have been used extensively in various applications owing to their bright luminescence, the drawback of this classes of materials is the presence of toxic elements like Cd and Pb.[21, 43] The search for alternatives to these materials continues and to this end, semiconductor NCs belonging to the I-III-VI group has been proven to be one of the best candidates.[49] In this class, the Cu-chalcogenide-based NCs are of utmost relevance, and this thesis focuses on CIS- and CISe-based NCs belonging to this group. These materials have significant differences to the II-VI and IV-VI groups both in bulk and nanoscale. Bulk I-III-VI crystal can be viewed as a derivative of cubic zinc-blende structure adopted by binary II-VI and IV-VI group materials, obtained by replacement of Zn^{2+} ions with the group I and III metals as illustrated in *Figure 3.1*.[93, 94]
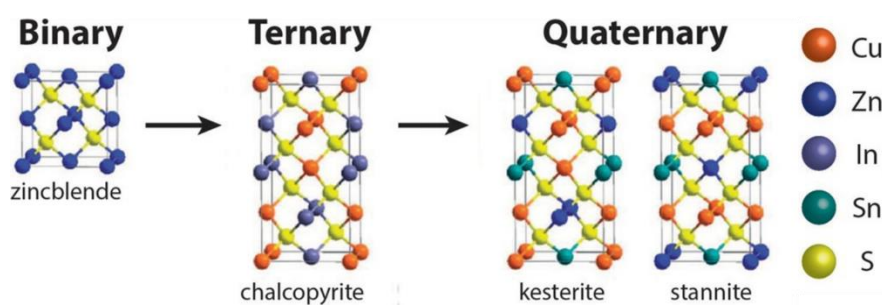
Figure 3.1 *Relationship between cubic zinc-blende structure adopted by II-VI semiconductors and crystal structures adopted by Cu-chalcogenide-based semiconductors. Reprinted from ref. 94 with permission. Copyright © 2016 WILEY-VCH Verlag GmbH & Co. KGaA, Weinheim.*

The presence of two non-isovalent cations leading to a reduced symmetry results in a larger primitive cell and lattice distortion, which in turn results in a tetragonal chalcopyrite structure of the bulk I-III-VI crystals.[95] Along with the chalcopyrite phase, nanostructured I-III-VI crystals also exist in the hexagonal wurtzite phase along with a wide range of off-stoichiometric

compositions. The off stoichiometry in these NCs is maintained with the presence of a large number of lattice defects in the crystal which contributes to their properties.[95] CIS NCs with a bulk band gap of 1.5 eV and exciton Bohr radius of 4.1 nm[20, 96] exhibit tuneable PL ranging from the visible to the NIR spectral range. The selenide counterpart, i.e., CISe NCs on the other hand with a narrower bulk band gap of 1.04 eV and exciton Bohr radius of 10.6 nm[21] enable the shift of the PL further into longer wavelengths of the NIR range. Thus, a variation of the chalcogenide along with fine tuning of size and composition enables the tuning of optical properties in a wide range of the spectrum (*Figure 3.2*). Consequently, this class of materials has been employed in a wide range of applications, especially in the fabrication of solar cells,[97, 98] LSCs,[99] photodetectors,[100] bioimaging, drug delivery,[16, 101] etc.
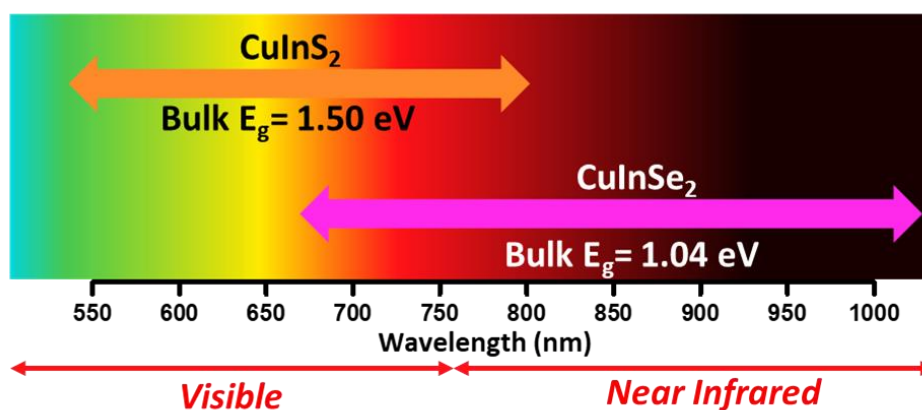
Figure 3.2. *Spectral range of CIS and CISe NCs.*

Synthetic advances of 0D CIS(Se)-based NCs

The employment of high-temperature hot-injection and heat-up methods for the synthesis of CdSe NCs with narrow size distribution and exemplary optical properties paved the way for using similar methods for CIS(Se)-based NCs as well. Early reports of these methods included synthesis by Allen et al., wherein CISe NCs were synthesized using bis(trimethylsilyl)selenide (Me$_3$Si)$_2$Se as a chalcogenide precursor with TOP and OlAm as coordinating solvents. They presented the first stoichiometric control of the CISe NCs synthesized with a variation of reaction temperature, which led in turn to the tuning of optical properties.[35] Tang et al. reported the synthesis of CISe, CGSe, and CIGSe NCs using commercial metal salts and Se powder dissolved in OlAm.[65] Using TOP-Se and trioctylphosphite complexes of CuI and InCl$_3$, Nose et. al synthesized CISe NCs with controlled size.[50] Single source precursors already containing Cu-S(Se) and In-S(Se) bonds, such as xanthates and dithiocarbamates, were also exploited for the synthesis of multicomponent CIS(Se) NCs.[62, 102]

One important aspect of the synthesis of CIS(Se)-based NCs to achieve a better size and shape control is balancing the reactivities of Cu- and In-precursors with respective chalcogenide sources. Alkanethiol-assisted synthesis, wherein long-chain thiols like 1-dodecanthiol (DDT), are employed to balance the reactivities of cations, has offered significant control over the size and shape of CIS(Se) NCs. Xie et al. designed the route to synthesize nearly monodisperse CIS$_2$ NCs with sizes ranging from <2 to 20 nm.[103] They found that Cu always formed Cu$_x$S (x=1–2) in the presence of solvents/ligands, like ODE, TOPO, amines, and carboxylates, even at low temperatures when InS could not be formed, thus showing that the reactivity of Cu is much higher than that of In. Thus, they used alkylthiol which is a soft base to suppress the reactivity of Cu, and, depending on the ratio of the alkylthiol and Cu, they could tune the ratio of Cu:In in the synthesized CIS$_2$ NCs. Zhong et al. synthesized CISe NCs, using DDT as a ligand and ODE as a non-coordinating solvent. They found that at a relatively low temperature of 180°C they could synthesize high-quality CISe QDs and at a higher temperature of 230°C CISe NPLs were formed.[104]

Various syntheses of CIS(Se) NCs employing DDT as a ligand have been put forward over the years, leading to high-quality CIS(Se) NCs.[95, 105-107] At high temperatures, DDT decomposes and can be used as a source of sulphur for the synthesis of CIS NCs which has been exploited in many heat-up approaches.[49, 108, 109] At the same time, the presence of DDT in the synthesis of CISe NCs at relatively high temperatures can result in the formation of quaternary CISeS NCs.[21] It is difficult to avoid its usage though, as it also plays the role of a reducing agent that prevents the oxidation of Cu$^+$ in the reaction and, therefore, is essential for the synthesis.[21] In addition to thermodynamically favoured tetragonal CIS(Se) NCs generally synthesized, the hexagonal wurtzite crystal structure was reported for CIS NCs by Pan et al. for the first time. They synthesized monodisperse CIS NCs with tuneable structures of zinc-blende and wurtzite, using a hot-injection approach at 200°C by employing diethyldithiocarbamate precursors of Cu and In, and OlAm as an activating agent and a ligand, and DDT or oleic acid as capping ligands. Oleic acid yielded CIS NCs with zinc-blende structure and DDT yielded CIS NCs with wurtzite structure.[62] Consequently, wurtzite CISe NCs were synthesized by Norako et al. for the first time by injecting diphenyl diselenide into a hot solution of CuCl and In(acac)$_3$ at 180°C for 3 hours.[110]

Growing ZnS shell with a wider band gap on the CIS(Se) NCs leads to a type I core/shell structure, yielding strongly emitting NCs with high PL QY. Li et al. proved the significant enhancement of PLQY from 8% of the core CIS NCs to 60% of the CIS/ZnS core/shell NCs, which were then used as fluorescent probes for in-vivo imaging.[16] They used a zinc-precursor,

which consisted of a mixture of zinc stearate in ODE and zinc xanthate in dimethyl formamide (DMF) and a shell growth temperature of 230°C. Cassette et al. reported the enhancement of PLQY from 4% in CISe core NCs to 43% in the CISe/ZnS core/shell NCs.[51] The shell growth was carried out employing zinc bis(ethylxanthoxanate) and zinc oleate at 180°C. Klimov group reported CIS/ZnS core/shell NCs with PLQY as high as 80%.[111] Thus, over the years, highly luminescent CIS(Se) NCs with ZnS shell have been synthesized with a majority of reports focusing on CIS-based NCs. Along with ternary compositions, quaternary compositions derived from CIS(Se) nanostructures have also been explored. In these cases, the presence of a larger number of reactive species further necessitates optimization of reaction parameters.[101, 112]

The emergence of CE pathway described in *Section 2.5* opened another route for achieving shape and size control, since in these reactions the anion sublattice of the template NCs is maintained throughout the exchange, leading to the preservation of the initial crystal structure in most cases, and, consequently, the resulting shape and size of the NCs remain unchanged. Capitalizing on these advantages, CIS(Se) NCs were synthesized with a partial CE approach, wherein only a part of the host cations was exchanged with the incoming guest cations, leading to a wide range of off-stoichiometric compositions and metastable crystal phases.[23] Starting with binary $Cu_{2-x}S(Se)$ a wide range of CIS(Se) NCs were synthesized.[21, 24] Tuning the composition of the NCs synthesized via CE is possible simply by varying the amount of Cu or In precursors used in the synthesis. In this way, starting with wurtzite $Cu_{2-x}S$ NCs Stam et al. applied the partial CE with In leading to the formation of luminescent CIS NCs with the wurtzite crystal phase.[113] TOP a soft base, was used for extraction of soft acid Cu^+ from the host lattice, whereupon the balance of extraction of Cu^+ ions and replacement with In^{3+} was maintained at a low temperature. The same group also reported the synthesis of luminescent $CISe_2/CIS_2$ dot-in-rod core/shell heterostructure, starting with CdSe/CdS dot-in-rod NCs, wherein the first exchange with Cu^+ yielded intermediate Cu_2Se/Cu_2S nanorods, followed by a sequential partial CE with In^{3+} to obtain the desired nanorods.[114] Akkerman et al. reported the synthesis of ternary CIS and quaternary CZIS NCs starting with $Cu_{2-x}S$.[68] In this process, a sequential addition of Zn-precursor to CIS NCs after Cu^+-to-In^{3+} CE led to the formation of a core/shell-like structure, resulting in luminescent NCs, whereas, combining both precursors in one pot yielded homogeneously alloyed quaternary CZIS NCs, which were non-emitting. In this case, the initial hexagonal structure of the Cu_2S NCs was preserved after the exchange. Highly emissive quaternary CZIS NCs with 80% PLQY were synthesized by De Trizio et al., starting with $Cu_{1-x}InS$ NCs prepared using a heat-up approach by heating CuI,

In(Ac)$_3$, and DDT at 230°C.[115] Initial tetragonal roquesite phase was preserved in this case. Starting with Cu$_{2-x}$Se Lox et al. synthesized CISe NCs following a partial CE pathway, which resulted in tuneable PL in the NIR range with a variation of the size of the synthesized NCs.[21] The initial shape of the NCs could be preserved in this case along with their crystal structure. Thus, CE serves as a suitable route for the synthesis of I-III-VI-based multicomponent NCs with a good control over their size, shape, and composition. Despite advances of CIS(Se) NCs there is still a lot of space for a further improvement of the synthesis of CISe NCs that would enable reaching longer wavelengths in the NIR range, since the emsission range in the NIR is still limited.

Synthetic advances of 2D I-III-VI semiconductor NCs

Studies on semiconductor 2D NCs have shown that they exhibit unique properties which are attributed to their anisotropic shape.[25, 81, 89, 116-119] Atomically flat NPLs or NSs have thicknesses which are smaller than the corresponding Bohr radius of several semiconductors, while having larger lateral dimensions leading to strong quantum confinement in only one direction, i.e., within their thickness.[20] A prominent example is CdSe NPLs, unique properties of which include exceptionally narrow PL, enhanced optical absorption, suppressed Auger-recombination, and giant oscillator strength.[25, 120, 121] Noteworthy that research on 2D NCs has been done mostly on binary metal chalcogenides, containing toxic Cd[25, 122, 123] and Pb[119, 121, 124] metals, and very scarcely explored in the case of multicomponent I-III-VI-based NCs. It is therefore reasonable to extend the study of anisotropic properties to this class of materials as well, which might also reveal interesting optical properties that are not in alignment with the widely studied 0D QDs.

Some synthetic strategies have already resulted in 2D I-III-VI-based NCs. E.g., Zhong et al. reported the synthesis of hexagonal CISe NPLs using DDT as a ligand and ODE as a non-coordinating solvent. They obtained small CISe$_2$ NCs at a lower temperature of 180°C, while at an elevated temperature of 210°C and a long reaction time of 3 h hexagonal plates with sharp edges were grown.[104] A mixture of triangular, hexagonal, and disk-like CISe NPLs were synthesized by Tang et al. in a one-pot approach using commercial salts of Cu, Se powder, and OlAm.[65] However, due to the disadvantages of direct methods in the synthesis of multicomponent NCs, several approaches have been explored to find alternatives to the direct synthesis of 2D I-III-VI-based NCs. The synthesis of CIS NSs via self-organization of smaller CIS NCs, driven by the change in the composition of the NCs, was carried out by Berends et al.[116] Template-mediated synthesis of ternary and quaternary NCs has been proven to be a facile

synthetic route in the case of small NCs, which has further been investigated in 2D NCs as well. Starting with covellite CuS, Liu et al. successfully synthesized ternary Cu-chalcogenide-based NPLs with various trivalent and tetravalent cations (In^{3+}, Ga^{3+}, Fe^{3+}, Sn^{4+}, and Ge^{4+}).[125] $Cu_{2-x}Se_yS_{1-y}$ NPLs were pre-synthesized by Lesnyak et al., which served as templates for subsequent partial CE with Zn^{2+} or/and Sn^{2+} ions leading to the formation of 2D CZSeS, CSnSeS, and CZSnSeS NCs with controlled composition.[22] Starting from ultrathin covellite CuS NPLs Wu et al. synthesized quite monodisperse ternary CIS and quaternary $CuIn_xGa_{1-x}S_2$ and Cu_2ZnSnS_4 NPLs at high temperatures. Similar CuS NPLs synthesized by Wu et al. were employed as templates by Lox et al. in the synthesis of alloyed photoluminescent CZIS NPLs and cookie-shaped CZIS/ZnS NPLs.[20] Shamraienko et al. synthesized binary PbSe, HgSe, ZnSe, SnSe, and quaternary Cu-Zn-Sn-Se NSs starting from thin CuSe NSs followed by either partial or complete exchange of host cations.[126]

Synthesis of ultrathin CISe NSs and NPLs derived via CE from 2D $Cu_{2-x}Se$ NCs using a dodecaneselenol precursor was reported by Berends et al.[127] A variation of reaction parameters enabled to control the shape of the $Cu_{2-x}Se$ NCs, which then served as templates for the synthesis of CISe NCs without altering their morphology. Ultrathin CISe NPLs with a thickness as small as 2 nm synthesized via partial CE were reported by Bi et al.[100] These template-mediated syntheses of I-III-VI-based NPLs were carried out starting with binary Cu-chalcogenide NPLs. An alternative to this route is the formation of CIS from In_2S_3. Following this strategy, Chen et al. recently reported the In_2S_3-template-assisted synthesis of CIS NPLs. They first carried out the synthesis of ultrathin hexagonal In_2S_3 NPLs which were then subjected to partial CE to incorporate In^{3+}, thereby forming CIS NPLs.[128] Yuan et al. applied a similar method, in which CZIS NPLs were synthesized via two subsequent CE reactions with Cu and Zn on the hexagonal template In_2S_3 NPLs.[129] The synthetic strategies developed for 2D I-III-VI NCs still suffer from poor size and shape control and low PL efficiencies. CIS-based 2D NCs with highly intensive inherent PL are rarely reported. Additionally, none of the reported CISe-based NPLs/NSs exhibit PL. Thus, development of synthetic pathways that enable the anisotropic growth of luminescent 2D I-III-VI NCs needs to be carried out.

PL mechanism and characteristic optical properties of I-III-VI-based semiconductor NCs.
Although extensive studies have been dedicated to developing synthetic strategies and plausible applications of Cu-chalcogenide-based nanomaterials, their light emission mechanism remains rather less understood. The unique optical properties of CIS(Se)-based NCs could not be explained by the simple band edge recombination, as observed in II-VI group

semiconductor NCs, resulting in well-defined absorption features, narrow emission ensemble bands, and small Stokes shift.[130] Various recombination mechanisms have been proposed for CIS(Se)-based NCs, including: 1) *donor–acceptor pair recombination,* in which both electron and hole are localized on defects forming intra-gap states[105] (*Figure 3.3a*); 2) *localized electron-valence band hole recombination,* in which the electron is localized on Cu antisite defects or sulphur vacancies[131, 132] (*Figure 3.3b*); 3) *conduction band electron- localized hole recombination,* in which a delocalized electron recombines radiatively with an intra-gap localized hole[111, 133] (*Figure 3.3c*); and 4) e*xciton fine structure model,* which is based on the intrinsic electronic structure of CIS(Se)[134] (*Figure 3.3d*). Among them the most accepted mechanism is the radiative recombination of a photoexcited delocalized conduction band electron and a localized hole residing in an intra-gap state often associated with off-stoichiometric effects that have been shown to enhance the emission efficiency.[135-137] This mechanism essentially can explain most characteristics of PL observed in CIS(Se)-based NCs.
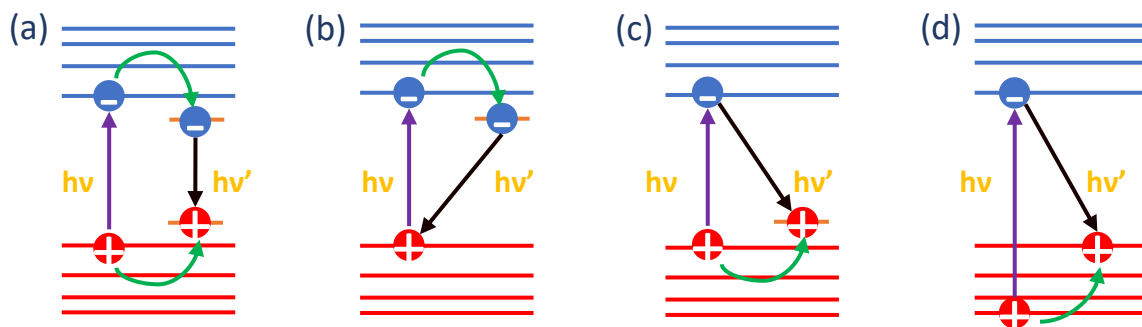
Figure 3.3 *Various mechanisms of radiative recombination in I-III-VI semiconductor NCs: donor–acceptor pair recombination (a), localized electron–valence band hole recombination (b), conduction band electron–localized hole recombination (c), exciton fine structure model (d). Purple, green, and black arrows indicate excitation, non-radiative transition, and radiative recombination respectively. v is the frequency of absorbed light and v' is the frequency of emitted light. Adapted from ref. 130 with permission. Copyright © 2019, American Chemical Society.*

Studies on Cu-doped II-VI NCs have suggested that the intra-gap states reside on copper atoms, and the similarities of their properties to I-III-VI$_2$ semiconductor NCs imply that emission centers in these NCs are also Cu-related and the intra-gap recombination centers are native defects of these materials.[135, 136] So far, the oxidation state of Cu in these emissive centers is still a question of debate. While some studies show that the emissive center is Cu$^+$, because Cu exists in +1 oxidation state in CIS NCs as indicated by X-ray photoelectron spectroscopy (XPS) studies, some studies also emphasize the importance of the presence of paramagnetic

Cu^{2+} defects for radiative exciton recombination.[133, 135-138] Spectro-electrochemical studies by Fuhr et al. have shown both the Cu^+ and Cu^{2+} centers to be emissive with the dominance of Cu^{2+} defects in Cu-deficient QDs and Cu^+ in stoichiometric QDs.[139]

The characteristic optical properties of I-III-VI NCs include featureless absorption, very long radiative lifetimes (100–500 ns), large Stokes shift (300–500 meV), and a large PL broadening (>300 meV of full width at half maximum (FWHM)).[130] Absorption spectra of I-III-VI-based NCs represent a featureless profile devoid of excitonic peaks, which can be attributed to their poor size, shape, and composition control.[21] Long radiative lifetimes and large Stokes shift are generally attributed to the intra-gap defects native to this class of materials, thus making them inherent properties observed in all studied samples. Berends et al. studied the origin of the radiative and non-radiative decay of CIS- and CIS-based NCs in detail and attributed long PL lifetimes of radiative decay to recombination of a delocalized electron with an intra-gap state localized hole, while non-radiative recombination was assigned to electron trapping on the surface defects of the NCs. The long radiative lifetimes of I-III-VI NCs were attributed to the fact that the wave functions of both, the delocalized conduction band electron, and the localized hole, overlap only to a small degree.[136]

The mechanism of PL broadening, however, does not have a cohesive explanation. Several studies have proposed different explanations for the origin of a broad PL.[133, 135, 139] Some suggested QDs' size polydispersity to be a plausible reason but that alone could not explain such broad PL and the obscure mechanism behind it led to a prediction that it is also an intrinsic property of the material. However, this speculation has been challenged by recent single-particle studies.[140, 141] Comparison of the PL line widths of a single-particle and a NC ensemble of $CuInS_2$/ZnS QDs by Zang et al. indicated that the broad PL is not an intrinsic property of these materials but a result of dot-to-dot variations in emission energy.[141] It was observed that even for a particularly narrow size distribution, the PL bandwidth of the single particle was approx. 60 meV as compared to the PL of the QD ensemble, which was approx. 300 meV. This suggests that despite a narrow size distribution the reason for broad PL can still be attributed to the ensemble heterogeneity in terms of its composition variation from particle to particle. This sample heterogeneity results in a large number of Cu-related emission centers which are positioned randomly. This random positioning results in varying energy contribution from the electron-hole coupling to the total PL energy, exhibiting a broad PL spectrum. Thus, in principle, the PL line widths of this class of materials can be reduced to the range of 100 meV. The challenge, however, is the development of synthetic strategies that will enable

reducing the sample heterogeneity and thus the random positioning of emissive centers in the entire QD ensemble, resulting in narrower PL bands comparable to Cd- and Pb-chalcogenide-based NCs. One of the objectives of this thesis was to develop synthetic strategies to result in Cu-chalcogenide-based NCs with homogenous size and composition, resulting in narrow PL band widths.

4   Experimental Section

Abstract *This chapter describes the experimental methodologies adopted for the synthesis of various I-III-VI semiconductor NCs. It is divided into four sections. The first three sections, i.e., Sections 4.1–4.3 give detailed account of the methodologies and reaction conditions adopted for the synthesis of Cu-Zn-In-Se QDs, Cu-Zn-In-S NPLs, and Cu-Zn-In-Se NPLs. Section 4.4 describes the methods of sample preparation and their characterization.*

All syntheses were conducted using a Schlenk line equipped with a vacuum pump and an inert gas supply. An illustration of the experimental setup is given in *Figure 4.1*
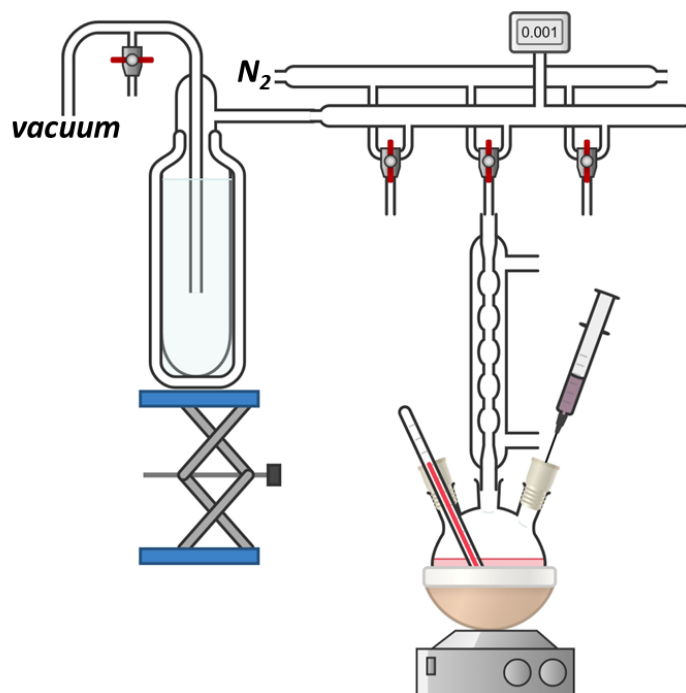
Figure 4.1 *Synthesis setup. (Designed in Chemix.org)*

4.1   Synthesis of Cu-Zn-In-Se NCs via Simultaneous Cation Exchange and their Surface Modification

4.1.1   Synthesis of Cu$_{2-x}$Se NCs

The parent Cu$_{2-x}$Se NCs were synthesized using a previously published protocol.[21] First, a Se-precursor solution was prepared by dissolving 790 (10 mmol) mg of Se powder in 5 mL of DDT and 5 mL of OlAm under vacuum at 50°C for 1 h. After the complete transformation of Se into a brown alkylammonium selenide, the precursor solution was cooled down and stored in the nitrogen-filled glove box. For the synthesis of Cu$_{2-x}$Se NCs, 0.5254 g (2 mmol) of Cu(acac)$_2$ were dissolved in 18 mL of OlAm and 9 mL of DDT upon vigorous stirring under

vacuum at 60°C for 1 h to produce a translucent white dispersion. Thereafter, the flask was filled with N_2 and the temperature was raised to 140°C. With the increase in temperature, the solution became transparent and yellowish-green in colour. Once the required temperature was attained, 1.32 mL (1.32 mmol) of the Se-precursor was injected. In 30 sec after the injection, the reaction mixture was cooled down to room temperature. The crude reaction mixture of $Cu_{2-x}Se$ NCs without any additional modification was used as parent NCs for the exchange with In^{3+} and Zn^{2+} cations (see the next section). An aliquot of 0.2 mL of the reaction mixture was taken out and precipitated by adding methanol followed by centrifugation at a speed of 5100 rpm for 5 min and finally redispersed in toluene and stored for further characterization. For the synthesis of larger CZISe NCs for element mapping, the size of parent $Cu_{2-x}Se$ NCs was increased by an increase in reaction temperature from 140°C to 200°C. The reaction time was also increased to 4 minutes along with a decrease in Cu:Se ratio from 1.5:1 to 1:1.

4.1.2 Synthesis of CZISe NCs

Using the synthesized $Cu_{2-x}Se$ NCs as templates, a mixture of the In- and Zn-precursors was injected for a combined Cu^{+}-to-In^{3+} and Zn^{2+} CE reaction to occur. In-precursor was prepared by dissolving 1.0213 g (3.5 mmol) of $In(OAc)_3$ in 5.25 mL of OctAm, 5.25 mL of OlAm, and 31.5 mL of ODE in a 100 mL flask upon stirring under vacuum at 60°C. Then the flask was filled with N_2 and thereafter the temperature was raised to 150°C to prepare a clear solution. Subsequently, the solution was cooled and 10.5 mL of TOP was added and the precursor was stored in the glovebox. Zn-precursor was prepared by dissolving 1.83g (10 mmol) of $Zn(OAc)_2$ in 5 mL of OlAm and 5 mL of OctAm under vacuum for 1 h at 40°C, thereafter N_2 was passed and the temperature was increased to 100°C for a clear solution to form. Subsequently, the temperature was decreased and, upon reaching room temperature, the precursor solution was transferred to the glovebox. For the exchange, the required amounts of the In- and Zn-precursors were mixed inside the glovebox and then transferred to a flask purged with N_2. The temperature was raised to 220°C and 5 mL (0.3531 mmol) of the crude reaction mixture containing $Cu_{2-x}Se$ NCs were swiftly injected. The temperature was maintained for 20 min along with continuous stirring of the reaction mixture. Thereafter, the reaction mixture was allowed to cool down and was precipitated with methanol followed by centrifugation at 5100 rpm for 5 min. The particles were purified two times by redissolving in toluene and precipitating with methanol. To study the composition dependence of optical properties, various Cu:Zn:In ratios were used: 1:1:1, 1:1:2, 1:1:0.5, 1:2:1, and 1:0.5:1.

4.1.3 Ligand exchange

The OlAm- and DDT-capped NCs underwent ligand exchange with various new ligands. In the first attempt, the long-chain organic ligands were exchanged with small inorganic sulfide ions. For this, approx. 200 mg of CZISe NCs were dispersed in 10 mL of hexane followed by the addition of 10 mL of MFA and 1.5 mL of $(NH_4)_2S$ solution in water. This biphasic solution was kept under stirring overnight and the next day the two phases were separated and the MFA phase containing the NCs was purified two times with hexane to extract excess organic ligands. Thereafter, the MFA phase was precipitated with acetone and toluene followed by centrifugation at 12000 rpm for 5 min with subsequent dispersion of precipitated NCs in 1 mL of DMF to prepare a concentrated solution.

In the second attempt, the parent ligands were exchanged with $ZnBr_2$ and butylamine. 5 mL of 0.1M $ZnBr_2$ solution in methanol were added to 10 mL of NCs in toluene (20 mg/mL) until it turned turbid, followed by the dropwise addition of 7 mL of butylamine until it became transparent again. This mixture was precipitated by addition of 1 mL of methanol followed by centrifugation at 12000 rpm for 5 min. The precipitated NCs were dispersed in 2 mL of chloroform.

In the third attempt, the NCs were subjected to a ligand stripping method reported by Rosen et. al.[142] For this, 200 mg of Et_3OBF_4 were dissolved in 10 mL of acetonitrile inside a nitrogen filled glove box. This solution was added to the NCs dispersed in 10 mL of hexane (20 mg/mL), which resulted in a biphasic mixture. The mixture was kept under stirring overnight and after the NCs phase transfer into acetonitrile, it was precipitated with the addition of chloroform followed by centrifugation at 12000 rpm for 5 min. The precipitated NCs were redispersed in 1 mL of DMF.

4.2 Synthesis of Cu-In-S-based Nanoplatelets via Seed-mediated Approach

4.2.1 Synthesis of CIS NPLs

The synthesis of CIS NPLs was carried out starting with In_2S_3 seeds. For the synthesis of the In_2S_3 seeds, 66.3 mg (0.3 mmol) of $InCl_3$, 5.67 mL of OlAm (or 3.5 mL of OlAm and 2.17 mL of OctAm) were mixed in a three-neck flask, while 6.4 mg (0.2 mmol) of S powder and 1 mL of OlAm were mixed in a small vial inside a nitrogen-filled glovebox. The flask was swiftly transferred under nitrogen flow of a Schlenk line and was kept under stirring until all $InCl_3$ was dissolved. Simultaneously the vial was kept on a shaker until all S was dissolved. After

complete dissolution, the S solution in OlAm was injected into the flask and it was degassed and filled with N_2 alternatingly several times. Thereafter, the mixture was heated to 100°C and the temperature was maintained for 1 h under continuous N_2 flow. The resulting clear yellow solution was cooled down to room temperature. Thereafter, 80 µL, 200 µL, 400 µL, 480 µL, or 600 µL (2, 5, 10, 12, or 15% of In amount respectively) of a 0.075 M solution of [Cu(CH$_3$CN)$_4$]PF$_6$ in acetonitrile (prepared inside the glovebox) were taken in a syringe and injected into the reaction mixture at room temperature. The color immediately changed from yellow to light brown, indicating an immediate formation of CIS NC seeds. The reaction mixture was kept at room temperature overnight to complete the formation of the seeds. Subsequently, the reaction mixture was heated to 180°C for the NPLs to grow. The temperature was maintained for 1 h, and then the mixture was cooled down to room temperature. A color change of the reaction mixture was observed from brownish to reddish upon heating. To stabilize the NPLs, 1 mL of DDT was added and kept at room temperature under stirring for 1 h. An aliquot of this mixture was taken out and precipitated by adding methanol followed by centrifugation at 5100 rpm for 5 min and redissolving in toluene for further characterization.

4.2.2 Synthesis of CZIS NPLs

For incorporation of Zn, an excess (3 mmol) of zinc 2-ethylhexanoate was directly injected into the crude mixture of CIS NPLs synthesized as described above, at room temperature. The temperature was then increased to 180°C and maintained for 1 h. Upon heating, the color of the solution changed from red to orange. The resultant CZIS NPLs were cooled down to room temperature and precipitated by adding methanol followed by centrifugation at 5100 rpm for 5 min. They were purified two times through dissolving in toluene and precipitating with methanol, and then stored for further characterization in toluene.

4.2.3 Synthesis of CZIS/ZnS NPLs

For the ZnS shell growth, 99.8 mg (0.4 mmol) of Zn(DDTC)$_2$ dissolved in 2 mL of OlAm were injected into the as-synthesized CZIS NPLs at 180°C. The temperature was maintained for 1 h. Along with the rapid injection of the Zn-precursor, slow and controlled addition was also carried out using a syringe pump. In this case, once the temperature reached 180°C, the Zn-precursor was added using the syringe pump during 1 h. The resulting CZIS/ZnS core/shell NPLs were cooled down and washed with methanol and toluene. Alternatively, for the shell growth, the core CZIS NPLs were precipitated, which were then redissolved in 9 mL of ODE with 700 µL of OlAm and 400 µL of OctAm.

ZnS shell growth was also carried out using a previously reported procedure of colloidal ionic layer deposition.[143] For this, NPLs were redissolved in hexane and 300 µL of OlAm, then 1 mL of FA and 50 µL of sulfur precursor (1.26 mmol of $(NH_4)_2S$ in 15 mL of FA) were added, followed by shaking this mixture for 5 min. The hexane layer was decanted and washed further with FA. Thereafter, 150 µL of the Zn-precursor (1.26 mmol of $Zn(OAc)_2 \cdot 2H_2O$ in 15 mL of FA), 30 µL of OlAm, and 350µL of FA were added with subsequent shaking for 5 min. The hexane layer was separated, and the entire process was repeated to form another monolayer of ZnS. The NPLs were precipitated using ethanol and redispersed in toluene for further characterization.

4.2.4 Synthesis of CZIS/In₂S₃ core/shell NPLs

For In_2S_3 shell growth, an In-precursor was prepared by dissolving $InCl_3$ (0.6 mmol) in 1.3 mL of THF inside the glovebox. The precursor was added to the as-synthesized CZIS NPLs reaction mixture and was degassed at room temperature. Thereafter, the S-precursor was prepared by dissolving thiourea (0.6 mmol) in 1 mL of triethylene glycol dimethyl ether upon ultrasonication, which was then added over an hour into the reaction mixture using a syringe pump at 170°C. The synthesized NPLs were washed with methanol and toluene.

4.3 Synthesis of Cu-In-Se-based Nanoplatelets via Seed-mediated Approach

4.3.1 Synthesis of CZISeS NCs

This synthesis is based on the synthesis of CZIS NPLs described in the previous section. A S-precursor was prepared beforehand by dissolving 6.41 mg (0.2 mmol) of S powder in 1 mL of OlAm inside the glovebox. Additionally, 0.075 M solution of $[Cu(CH_3CN)_4]PF_6$ in acetonitrile was prepared and was kept under stirring inside the glovebox. An In-precursor was also prepared inside the glovebox by dissolving 66.30 mg (0.3 mmol) of $InCl_3$ in 650 µL of THF and 2.17 mL of OctAm. For the synthesis, 7.89 mg (0.1 mmol) of Se powder and 4 mL of OlAm were loaded in a 25 mL three-neck round-bottom flask equipped with a thermocouple and a magnetic stirrer and the mixture was degassed at room temperature for 30 min. The temperature was then raised to 200°C under a nitrogen flow to dissolve Se. Upon dissolving Se in OlAm a clear light orange solution was obtained. The solution was then cooled down to room temperature and 500 µL (0.1mmol) of the S-precursor and In-precursor (0.3 mmol) were injected. The mixture was again degassed at room temperature for 30 min in order to remove THF. After 30 min the flask was filled with nitrogen and the mixture was heated up to 100°C

and kept for 1 h for the formation of $In_2(SeS)_3$ seeds, which resulted in a clear bright yellow solution. Upon cooling the reaction mixture to room temperature, 200 µL of the Cu-precursor were added for the formation of CISe seeds, which was accompanied by an instantaneous color change to dark red. The flask was then covered with an aluminum foil and kept under N_2 flow overnight at room temperature. On the next day, the reaction mixture was first heated at 180°C for 1 h to form CISeS NPLs. Thereafter, 1 mL of DDT was added at room temperature and the mixture was kept under stirring for 1 h. After 1 h, 1080 µL (3.0 mmol) of zinc 2-ethylhexanoate was injected and the mixture was heated at 180°C for 1 h. Finally, the obtained NCs were purified using methanol and toluene. This synthesis constituted the replacement of 50% of S with 50% Se. Consequently, 75% of Se was employed in the synthesis by using 0.15 mmol of Se and 0.05 mmol of S, followed by 100% Se, i.e., 0.2 mmol of Se.

4.3.2 Synthesis of In_2Se_3 NSs

The synthesis of In_2Se_3 was adopted from the synthesis of In_2S_3 NSs reported by Park et. al.[144] For the synthesis, first, an In-precursor was prepared by mixing 55.29 mg (0.25 mmol) of $InCl_3$ with 3 mL of OlAm inside a nitrogen-filled glovebox. This mixture was kept under rigorous shaking at room temperature until all $InCl_3$ was dissolved in OlAm. In parallel, Se-precursor was prepared by dispersing 29.60 mg (0.375 mmol) of Se powder in 1 mL of OlAm by ultrasonication and then purging the mixture with nitrogen. 5 mL of OlAm were loaded into a 25 mL three-neck round-bottom flask equipped with a thermocouple and a magnetic stirrer and degassed for 30 min at room temperature. Thereafter, the flask was filled with nitrogen and the temperature was raised to 200°C. When the temperature of 200°C was attained, the Se suspension was injected into the flask. After approx. 10 min the Se powder was dissolved in OlAm forming a transparent light orange solution. After the complete dissolution of Se powder, the reaction mixture was cooled down to 115°C and the In-precursor was swiftly injected leading to a color change from light orange to bright yellow. The reaction mixture was maintained at this temperature for 1 h to produce In_2Se_3 seeds. After 1 h the mixture was further heated to 230°C for 1 h to form the In_2Se_3 NSs.

4.3.3 Synthesis of CISe NPLs

For the synthesis of CISe NPLs the above-mentioned steps for the synthesis of In_2Se_3 seeds were carried out. In_2Se_3 seeds were synthesized using varying amounts of $InCl_3$, i.e., 88.4 mg (0.4 mmol), 66.3 mg (0.3 mmol), 33.15 mg (0.15 mmol), and 28.73 mg (0.13 mmol). The amount of Se was kept the same as 15.79 mg (0.2 mmol) of Se powder. Simultaneously, 0.075 M solution of $[Cu(CH_3CN)_4]PF_6$ in acetonitrile was prepared inside the glovebox. After the

synthesis of the In$_2$Se$_3$ seeds, the reaction mixture was cooled down to room temperature and 200 µL of the Cu-precursor were injected, leading to an immediate color change from yellow to brown. The reaction mixture was kept under stirring overnight and on the next day was heated to 230°C for 1 h to promote the growth of CISe NPLs. Subsequently, the reaction mixture was cooled down to room temperature and 1 mL of DDT (previously purged with nitrogen) was added. This mixture was further kept under stirring for 1 h. Aliquots of this mixture were taken and NPLs were precipitated by adding methanol followed by centrifugation and redispersion in toluene. An additional purification step was carried out and the obtained NPLs were dispersed in 2 mL of toluene and stored for further characterization.

4.3.4   Synthesis of CZISe NPLs

For the synthesis of CZISe NPLs, 1080 µL (3 mmol) of zinc 2-ethylhexanoate were added to the as-synthesized CISe NPLs followed by heating to 230 °C for 1 h. After 1 h, the reaction mixture was cooled down to room temperature and the NPLs were precipitated by adding methanol and centrifugation at a speed of 5000 rpm. The supernatant was discarded, and the precipitate was redispersed in toluene and purified once again. Finally, the CZISe NPLs were redispersed in 4 mL of toluene and stored in a refrigerator for further characterization.

4.4   Characterization

4.4.1   Transmission electron microscopy (TEM)

TEM specimen preparations included additional purification of NCs by reprecipitation in methanol and dissolving in toluene to obtain a very dilute solution. The solution was drop-cast onto carbon-coated copper grids with subsequent evaporation of the solvent. To measure the CZIS NPL thickness, drops of acetonitrile were added in the dilute solution of NPLs in toluene to form stacks. Conventional bright-field TEM imaging was carried out on a JEOL JEM 1400 microscope equipped with a thermionic gun (W filament) and operated at an accelerating voltage of 120 kV.

High resolution imaging, high-angle annular dark-field scanning TEM (HAADF-STEM) imaging and spectrum imaging analysis based on energy-dispersive X-ray spectroscopy (EDXS) were performed at 200 kV with a Talos F200X microscope equipped with an X-FEG electron source and a Super-X EDX detector system (FEI). Prior to STEM analysis, the specimen mounted on a high-visibility low background holder was placed for 2 s into a model 1020 Plasma Cleaner (Fischione) to remove potential contamination. For all the STEM-based analyses, the NC solutions were drop-cast onto carbon-coated Ni grids to avoid Cu fluorescence radiation.

4.4.2 Powder X-ray diffraction (XRD) analysis

Samples of $Cu_{2-x}Se$ NCs, CZISe NCs, CZIS NPLs, CZIS/ZnS NPLs, and CZISe NPLs were prepared by drop-casting concentrated NC solutions onto a zero-background silicon wafer under air. Due to the high sensitivity of the In_2S_3 NPLs, In_2Se_3 NSs, CIS NPLs, and CISe NPLs to aerial oxidation, all of these crude reaction mixtures were transferred inside the nitrogen-filled glovebox directly after the synthesis and purified inside it. Thereafter, the sample was drop-cast on a silicon wafer inside the glovebox and was immediately measured. All XRD patterns were recorded on a Bruker D2 Phaser using a Cu source operated at 30 kV and 10 mA.

4.4.3 UV-Vis-NIR absorption spectroscopy

All absorption measurements were carried out using 1 cm path quartz cuvettes. The absorption spectra in the NIR range were recorded by preparing dilute dispersions of NCs in TCE and were recorded on a Cary 5000 UV-vis-NIR spectrophotometer (Varian). For recording absorption spectra in the UV-Vis range samples were prepared by diluting dispersions of NCs in toluene. The absorption spectra were recorded on a Cary 60 UV-Vis spectrophotometer (Varian).

4.4.4 Photoluminescence measurements

For steady-state PL measurements in the NIR range, the samples were prepared by dispersing the NCs in TCE. The PL spectra were recorded on a FluoroLog-3 spectrofluorometer (Horiba Jobin Yvon Inc.) using an excitation wavelength of 450 nm. Absolute PLQY and PL lifetime measurements of NCs emitting in the NIR were carried out using NC dispersions in toluene. Absolute PLQY measurements were performed on an Edinburgh Instruments spectrofluorometer FLS900 (equipped with Xe lamp, PMT-1700 and calibrated integrating sphere). All samples were excited at 700 nm and their concentration was adjusted to optical density of 0.15 at the excitation wavelength. The PLQY values were calculated by Flouracle software. The time-resolved PL (TRPL) traces were collected using an Edinburgh Instruments EPL-510 pulsed laser diode for excitation (λ = 508.2 nm, pulse width = 177.0 ps) and a time-correlated single photon counting (TCSPC) card. Average PL lifetimes were calculated when the initial signal intensity was reduced to 10 000 counts/e.

For PL measurements in the visible range, the samples were prepared by dispersing the NCs in toluene. The PL spectra were recorded on a Fluorolog-3 spectrofluorometer (Horiba Jobin Yvon) using an excitation wavelength of 435 nm. Relative PLQY measurements of CZIS NPLs and CZIS/ZnS NPLs emitting in the visible range were performed using CdSe/CdZnS/ZnS core/shell/shell QDs as a reference with 56.6 % absolute QY determined on

a Fluorolog-3 spectrofluorometer equipped with a Quanta-φ integrating sphere (Horiba Jobin Yvon, Inc.). TRPL traces were collected on the same instrument equipped with a pulsed laser diode (410 nm) and time-correlated single-photon-counting module at room temperature. Average PL lifetimes were calculated when the initial signal intensity was reduced to 10 000 counts/e.

4.4.5 Elemental analysis

The samples of CZISe QDs and CZIS NPLs for inductively coupled plasma optical emission spectroscopy (ICP-OES) were prepared by decomposing the NCs in 2 % aqua regia with subsequent dilution with Milli-Q water. Measurements were carried out on an iCAP 7400 device (Thermo Scientific) with six matrix-matched calibration standard solutions, each containing Cu, In, and Zn with concentrations of 100 mg/L, 50 mg/L, 10 mg/L, 5 mg/L, 1 mg/L, and 0.5 mg/L. For ICP-OES measurements, the ICP multi-element standard solution IV (Merck KGaA, Certipur®) was used. Samples of CZISe NPLs were also prepared using the same procedure as mentioned and the measurements were done on a PerkinElmer Optima 7000DV instrument to quantify the copper, indium, and zinc contents in the synthesized NPLs.

4.4.6 Fourier-transform infrared (FTIR) spectroscopy

Attenuated total reflectance (ATR) FTIR spectra were recorded on a Thermo Scientific Nicolet iS5 FTIR spectrometer. Concentrated solutions of NCs in the respective solvent were directly drop-cast on the ATR crystal and the solvent was left to evaporate before recording the spectra.

5   Results and Discussion

Abstract *Using the synthetic strategies elaborated in Chapter 4, three morphologically varied types of NCs belonging to the I-III-VI group were synthesized in this work. This chapter explores the structural and morphological properties of each of these NCs using TEM, HRTEM, HAADF-STEM, EDXS, and XRD techniques, employing the equipments described in Section 4.4. Subsequently, the study of the optical properties of these differently shaped I-III-VI NCs was carried out using various spectroscopic measurements, including absorption, PL, TRPL spectroscopy, and PLQY measurements. The unique optical properties exhibited by the different NCs, i.e., CZISe NCs discussed in Section 5.1, CZIS NPLs discussed in Section 5.2, and CZISe NPLs discussed in Section 5.3, can be attributed to a combined effect of the difference in confinement, morphology, composition, and shape/size distribution.*

5.1   Cu-Zn-In-Se Nanocrystals Synthesized via Cation Exchange and their Surface Modification for Prospective Applications

5.1.1   Background and Aim

In the I-III-VI group of nanomaterials, most studies have been carried out on CIS-based NCs, which have established them as suitable fluorophores in a wide range of applications.[145] However, the selenide counterparts, i.e., CISe-based NCs, are of particular importance for light-harvesting owing to the smaller bandgap of 1.04 eV of the bulk CISe and a larger exciton Bohr radius of 10.1 nm, as compared to CIS, which has a comparatively larger bandgap of 1.5 eV and smaller Bohr radius of 4.1 nm.[146] These properties have been proven to be extremely instrumental in the development of photovoltaic cells employing CISe NCs, with PCE as high as 10%.[147] Even higher PCE of 11.6% and 13.6% were reported for solar cells, fabricated employing CZISe QDs by Du et al. and Zhang et. al., respectively.[112, 147] Moreover, CISe-based NCs are also explored as light harvesters in LSCs, since the commonly observed large Stokes shift helps in reducing the self-absorption losses, thereby increasing the photon conversion efficiency of the solar cells attached to these LSCs.[11, 12, 99, 148] Along with it, NIR-active CISe NCs are also of importance in biological applications due to their less toxic nature and compatibility with the transparent tissue range.[51] Thus, CISe-based NCs are a suitable material

for a wide range of applications and extending their PL emission further into the NIR unlocks new applications for this material.

In most reported syntheses, however, CISe QDs exhibit low PLQY[65, 110, 145, 149] without the additional shell growth, which means that the NC surface is particularly prone to surface defects thus increasing the number of centers for non-radiative recombination.[150] PLQY of the CISe cores has drastically been increased by overcoating the NCs with wide band gap semiconductors such as ZnS or CdS.[35, 50, 51] In our group, e.g., the previously synthesized core CISe NCs showed no PL without the shell, and only after the deposition of a ZnS shell they exhibited PLQY below 1%.[21] Also, previously reported CISe-based NCs exhibited very broad PL band widths on the order of 300 meV and the underlying reason was attributed to the sample inhomogeneity.[141] Thus, exploration of synthetic pathways to yield high-quality CISe NCs with homogeneous size, shape, and composition, resulting in high PLQY and narrow PL band width is still a topic of research and is the principle motivation behind this work. Additionally, different applications of semiconductor NCs require different surface properties and thus post-synthetic surface modification of the synthesized NCs to make them the best fit for the target prospective application is also of great relevance.

The aim of this part of the work was to develop a synthetic pathway for CISe-based NCs that exhibit good shape and size control which is reflected in good optical properties in the NIR range. Direct synthesis employing conventional hot-injection and heat-up approaches has yielded small CISe NCs with PL tunable in the NIR range.[35, 50, 146, 150] However, due to the disadvantages of this method for the synthesis of Cu-chalcogenide-based multicomponent NCs discussed in *Section 2.5,* the strategy of partial CE was adopted to tackle the lack of control over the reaction. Therefore, to realize the aim, a two-step synthetic pathway for photoluminescent CZISe NCs via a CE approach using $Cu_{2-x}Se$ NCs as templates with subsequent CE employing Zn^{2+} and In^{3+} as guest cations, was developed. The family of Cu-chalcogenides serve as suitable templates for these CE reactions since Cu^+ is easily exchangeable with other cations.[24, 126, 151] In the case of CZISe NCs, the comparable ionic radii of the host cation Cu^+ and guest In^{3+} and Zn^{2+} cations in a given coordination number help in maintaining the structure and morphology of the NCs.[68, 152] Additionally, the presence of a large number of copper vacancies in nanostructured Cu-chalcogenides facilitates the exchange process by providing an additional route for the diffusion of the cations.[69] The aim of this work also constituted augmenting the PLQY of the synthesized NCs without an additional step of shell growth, which was achieved through simultaneous incorporation of Zn and In. Additionally, to deduce a relation between the composition of the as-synthesized NCs and their

optical properties, ratio of the incoming cations involved was varied. Finally, with the aim of expanding the range of prospective applications of the NCs synthesized, possible routes of ligand exchange, wherein the parent long-chain organic ligands on the NC surface are exchanged with shorter new ligands were also explored.

5.1.2 Synthesis of $Cu_{2-x}Se$ NCs

The synthetic pathway developed for the synthesis of CZISe NCs is illustrated in *Figure 5.1*. The first step, involving the synthesis of $Cu_{2-x}Se$ NCs using a hot-injection approach, which serve as templates for the subsequent CE reaction, resulted in small, approx. 5 nm sized particles. The synthesis was carried out using a modification of a previously published protocol.[21, 69, 153, 154] As reported earlier, an initial ratio of Cu:Se of 1.5 and 30 sec reaction time are necessary to grow small-sized $Cu_{2-x}Se$ NCs. However, it was found that a relatively low reaction temperature of 140°C offered a better control over the size of the sythesized NCs as compared to 170°C used earlier.[21] Thus, the reaction conditions employed, i.e., short reaction time and a relatively low temperature, aid the synthesis of small $Cu_{2-x}Se$ NCs. Furthermore, a Cu deficient Cu:Se ratio of 1.5 was chosen to result in non-stoichiometric $Cu_{2-x}Se$ NCs with inherent Cu vacancies, which can then serve as a suitable template for the subsequent partial CE reaction. It has been reported that the presence of vacancies in non-stoichiometric $Cu_{2-x}Se$ NCs significantly accelerates CE as compared to nearly stoichiometric Cu_2Se.[69]
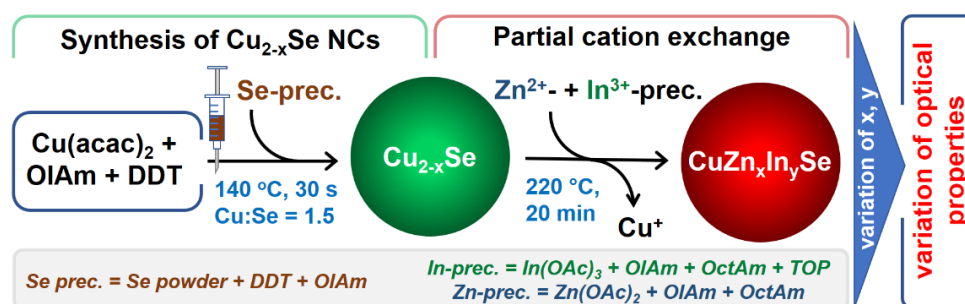
Figure 5.1 *A scheme depicting the synthesis of $Cu_{2-x}Se$ NCs with subsequent partial CE to CZISe NCs, followed by the study of composition dependence of their optical properties.*

As depicted in the TEM image shown in *Figure 5.2*, fairly monodisperse spherical $Cu_{2-x}Se$ NCs were synthesized using this synthetic strategy. The average size of these NCs was 4.44±0.04 nm. The same batch of starting $Cu_{2-x}Se$ NCs was used to carry out all the subsequent exchanges explained in the next section, to eliminate factors such as different size and composition of template NCs, which could possibly influence the properties of the final QDs. Thus variation in composition of the guest cations alone enabled to tune the position of the PL

maxima in the NIR region. XRD pattern depicted in *Figure 5.4* confirms cubic berzelianite crystal structure (ICSD C6-680) of the synthesized $Cu_{2-x}Se$ NCs which is in accordance to the previous report.[21]
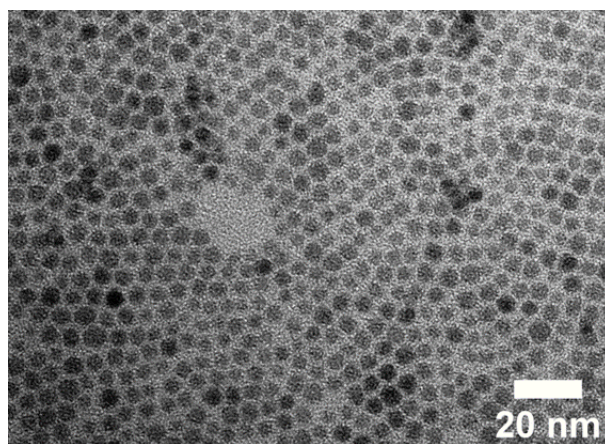
Figure 5.2 *Conventional TEM image of the starting batch of Cu₂₋ₓSe NCs.*

5.1.3 Synthesis of CZISe NCs with varied composition

In the subsequent step, as represented in the scheme in *Figure 5.1* a simultaneous CE of Cu^+-to-In^{3+} and Zn^{2+} was carried out to result in the desired CZISe NCs. For this, the In- and Zn-precursors prepared were mixed and the mixture was heated to 220°C. As soon as the desired temperature was attained, the $Cu_{2-x}Se$ NCs were injected rapidly and the reaction temperature was maintained for 20 min. The addition of the guest cations was accompanied by a colour change from the dark green colour of the template NCs to the dark brown colour indicating a successful CE reaction. The partial CE is faciliated by two factors. As explained in *Section 2.5,* according to the HSAB principle soft acids preferentially bind to soft bases and hard acids preferentially bind to hard bases. In this context, TOP, which is a soft base present in the In-precursor solution, binds preferentially with soft acid Cu^+, leading to its efficient extraction from NC lattice, thus facilitating the incorporation of In^{3+} and Zn^{2+}.[23, 56, 155, 156] Second, the presence of Cu vacancies in the template non-stoichiometric $Cu_{2-x}Se$ NCs aids the CE by providing additional diffusion pathways for the incoming and outgoing cations.[69, 113] It was observed by Akkerman et al. that at an elevated temperature and with simultaneous addition of guest cations homogenously alloyed CZIS NCs could be formed, while upon sequential addition at lower temperatures gradient alloy CZIS NCs with a ZnS-rich surface were obtained.[68] Following this, a relatively high temperature of 220°C was used because at higher temperatures the reactivity of Zn^{2+} increases thus enabling the diffusion of Zn^{2+} cations into the core of the NCs instead of replacing Cu^+ just on the surface. The TEM images of the NCs synthesized reveal their quasi spherical shape and a narrow size distribution (*Figure 5.3a-e*).
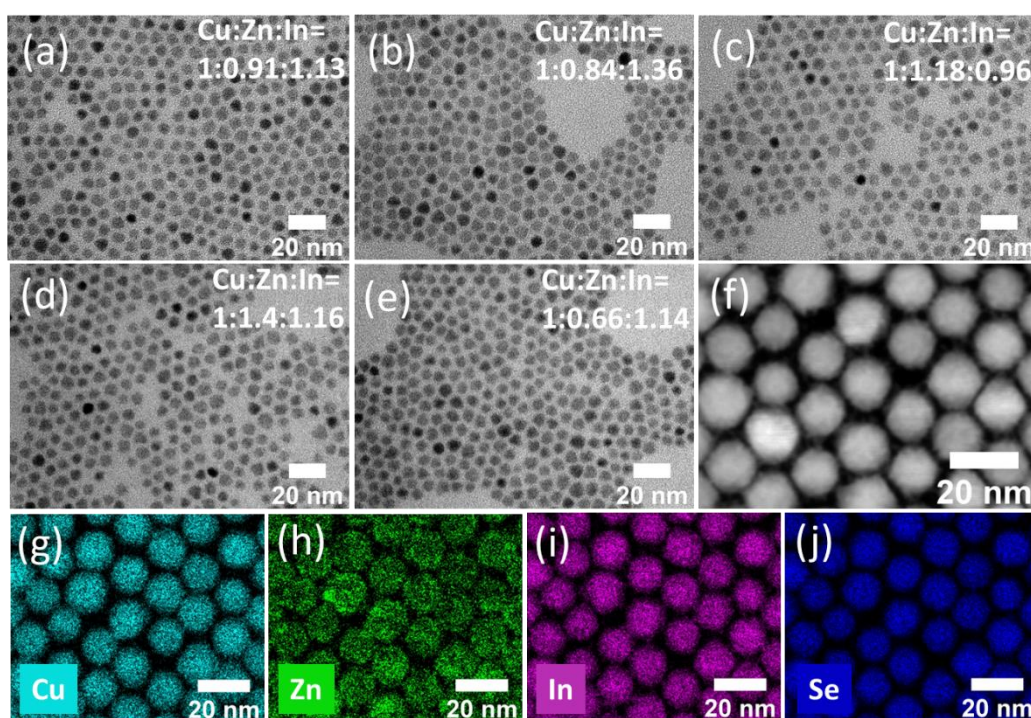
Figure 5.3 *TEM images of CZISe NCs with final Cu:Zn:In ratio = 1:0.91:1.13 (a), 1:0.84:1.36 (b), 1:1.18:0.96 (c), 1:1.41:1.16 (d), 1:0.66:1.14 (e). HAADF-STEM image (f) and EDXS element maps (g-j) of large CZISe NCs with Cu:Zn:In feed ratio of 1:1:1.*

Comparision of the the TEM image of the template $Cu_{2-x}Se$ NCs presented in *Figure 5.2* and the TEM images of CZISe NCs indicates that the morphology did not undergo any change owing to the fact that the anion framework is maintained during the CE reaction.[21] The estimated NC sizes summarized in *Table 5.1* indicate a slight increase in size after the CE reaction, possibly due to their simultaneous growth during the exchange. It should be pointed out that the sizes of all different compositions are similar and therefore the size effect on the resultant properties of the NCs can be neglected. To gather more insight into the morphology and element distribution of the NCs, HAADF-STEM and EDXS were carried out on larger, 12 nm-sized CZISe NCs. The HAADF-STEM image depicted in *Figure 5.3f* shows that these NCs are spherical in shape and the corresponding EDXS element maps shown in *Figure 5.3g-j* indicate rather homogenous distribution of Cu and In, which also corresponds well with the distribution of Se, while Zn appears to be distributed inhomogenously with a greater concentration in the outer layer. Thus, starting with non-stoichiometric $Cu_{2-x}Se$ NCs, the strategy of simultaneous CE to In^{3+} and Zn^{2+} resulted in the growth of gradient alloy-like NCs with In^{3+} replacing Cu^+ in the whole NC, while Zn^{2+} replacing Cu^+ more preferntially on the surface, contrary to homogenously alloyed CZIS NCs obtained via simultaneous CE by Akkerman et al. on Cu_2S NCs[68]

Table 5.1 *Initial feed ratios, final composition, In:Zn ratio, and average sizes of the CZISe NCs.*

Initial ratio Cu:Zn:In	Final ratio Cu:Zn:In	In:Zn	Cu:(In+Zn)	Size (nm)
1:1:1	1:0.91:1.13	1.24	0.48	5.02±0.8
1:1:2	1:0.84:1.36	1.60	0.45	5.2±0.7
1:1:0.5	1:1.18:0.96	0.81	0.46	5.0±0.7
1:2:1	1:1.4:1.16	0.82	0.38	5±0.7
1:0.5:1	1:0.66:1.14	1.72	0.55	5.2±0.6

As seen from the XRD patterns in *Figure 5.4*, the positions and the intensity of the peaks indicate the preservation of the crystal structure, which is expected from a CE approach. This is generally observed in CE reactions, wherein the anion framework remains intact whilst the exchange of host cations by guest cations takes place. In this case, the ionic radii of Cu^+, In^{3+}, and Zn^{2+} are comparable in the both tetrahedral and octahedral coordinations. Considreing this, there is most likely only efficient exchange of the cations while maintaining the integrity of the anion framework.[157] Preserving the integrity of the anion framework in a CE reaction has been used as a tool to synthesize CIS NCs with metastable crystal structures rather than the thermodyamically stable counterparts. In general, CIS(Se) crystallizes in the cubic phase or tetragonal phase derived from the distortion of the zinc-blende phase depending on the reaction temperature and composition.[95] However, metastable hexagonal CIS has been synthesized using a CE pathway by Akkerman et al., wherein they started from hexagonal $Cu_{2-x}S$ NCs in which a subsequent addition of In^{3+} and Zn^{2+} cations did not lead to restructuring, thus resulting in metastable hexagonal CIS and CZIS NCs.[68] The positions of the peaks in the XRD pattern of CZISe NCs in *Figure 5.4* shift slightly to lower Bragg angles compared to the position of the initial $Cu_{2-x}Se$ NCs, which indicates filling of the Cu vacancies by the incoming guest cations.[21]
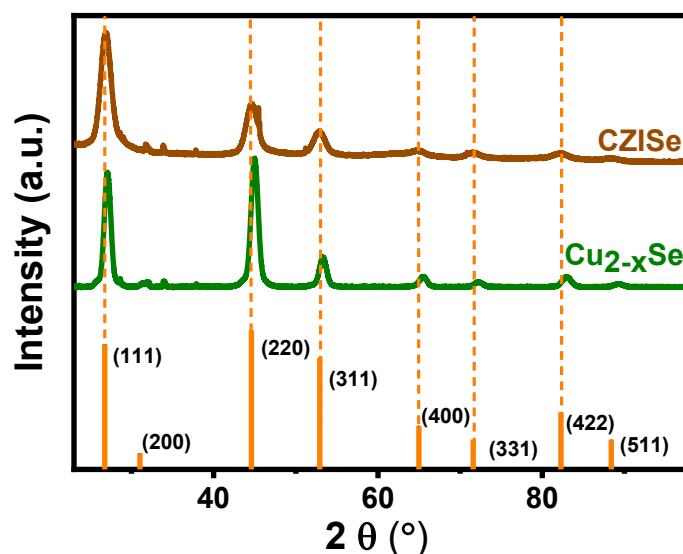
Figure 5.4 *XRD patterns of template Cu$_{2-x}$Se and CZISe NCs after simultaneous partial CE. The experimental XRD patterns are compared to a database powder diffraction file of cubic berzelianite (ICSD C6-680).*

The composition of the final NCs was controlled by a simple variation in the feed ratio of the guest cations. The initial feed ratios, the final composition from ICP-OES, and the corresponding sizes of the different CZISe NCs are summarized in *Table 5.1*. ICP-OES results show that the final ratios of Cu:Zn:In (In:Zn) are 1:0.9:1 (1.2), 1:0.8:1.4 (1.6), 1:1.2:0.9 (0.8), 1:1.4:1 (0.8), and 1:0.6:1.2 (1.7), derived from the corresponding feed ratios of 1:1:1, 1:1:2, 1:1:0.5, 1:2:1, and 1:0.5:1. The feed ratio of Cu:Zn:In of 1:1:1 resulted in Cu:Zn:In ratio of 1:0.91:1.13 with In replacing 37.4% of the Cu ions and Zn replacing 29% of the Cu ions. This indicates that the Cu$^+$-to-In^{3+} exchange is more feasible than Cu$^+$-to-Zn^{2+} one. However, there is also the possibility of Zn^{2+}-to-In^{3+} exchange simultaneously occuring leading to higher amount of In in the NCs. It was also observed by Akkerman et al. that even by using a large excess of a Zn-precursor the Zn content could not be increased after a certain limit, which also supports that Zn^{2+} can only partially replace Cu$^+$ and is less efficient than Cu$^+$-to-In^{3+} CE.[68] In the case of the synthesized CZISe NCs, first, the In amount was increased with feed Cu:Zn:In ratio of 1:1:2 resulting in the final Cu:Zn:In ratio of 1:0.84:1.36. Thus, even by doubling the In-precursor content there was no complete Cu$^+$-to-In^{3+} CE observed with In^{3+} replacing only 42.6% of Cu, while Zn^{2+} replaces 26.4 % of the Cu$^+$ cations. Thus, even though Cu$^+$-to-In^{3+} CE is more feasible, a competition between both exchanges makes it difficult to precisely control the reaction. Subsequently, a decrease in the In-precursor concentration led to a decrease in the amount of In vs. Zn. Thereafter, the Zn content was also varied by using a Cu:Zn:In feed ratio

of 1:2:1, resulting in the final ratio of 1:1.4:1.16. This obviously led to increasing the efficiency of Cu^+-to-Zn^{2+} CE resulting in Zn replacing 39.5% of Cu^+ and In replacing 32% of Cu^+. A decrease in the Zn amount with the Cu:Zn:In feed ratio of 1:0.5:1 led to the decrease in Zn content in the NCs, resulting in final Cu:Zn:In ratio of 1:0.66:1.14. Thus, it can be concluded that while there is a higher feasibilty of Cu^+-to-In^{3+} CE, there exists a competition between both exchanges which cannot be precisely controlled, resulting in varying compositions of the NCs synthesized.

It is also noteworthy that the entire reaction takes place without intermediate NCs purification step thus leaving the possibility of unreacted Cu^+ from the first step interfering in the CE step, thus adding to the difficulty of precise control of composition of the resultant CZISe NCs. Additional purification might lead to the stripping of the parent ligands inducing instability of the NC colloids and detrioration of optical properties and therefore was avoided. When the In:Zn feed ratio is plotted against the the final In:Zn ratio obtained from ICP-OES analysis, we observe that the final ratio corelates well with the feed ratio and an increase in the In:Zn feed ratio results in the corresponding increase in the final In:Zn ratio, as shown in *Figure 5.5*. Additionally, as seen in the graph, the final ratio of the host cations to the combined ratio of the guest cations, i.e., Cu:(In+Zn), against the feed In:Zn ratio did not show significant changes, thus indicating that the ratio between the host and the guest cations was roughly similar for all compositions independent of the varying ratio between the guest cations.
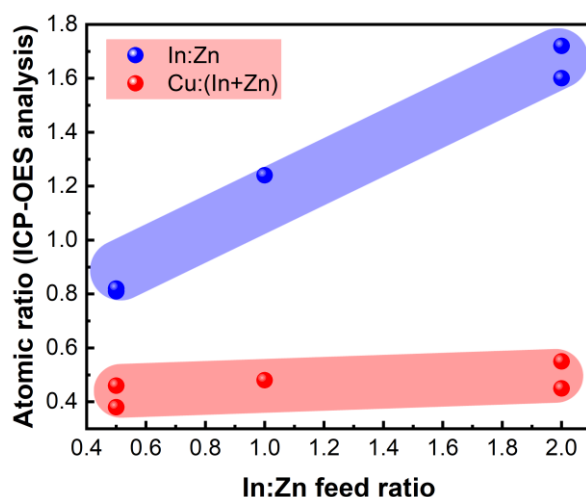
Figure 5.5 *In:Zn and Cu:(In+Zn) atomic ratios as obtained from ICP-OES analysis plotted vs. the feed In:Zn ratio.*

5.1.4 Optical properties of CZISe NCs with varied composition

The optical properties of the synthesized NCs were studied by using absorption and PL spectroscopy. Template $Cu_{2-x}Se$ NCs exhibit a LSPR with a maximum at approx. 1100 nm, as

shown in *Figure 5.6* commonly observed in this material and attributed to the collective oscillation of free holes.[21, 69, 153, 154] These free holes in the valence band originate from a large number of copper vacancies present in the crystal structure.[158, 159] The presence of the vacancies is indeed instrumental for CE with vacancy diffusion driving the exchange along with other factors.
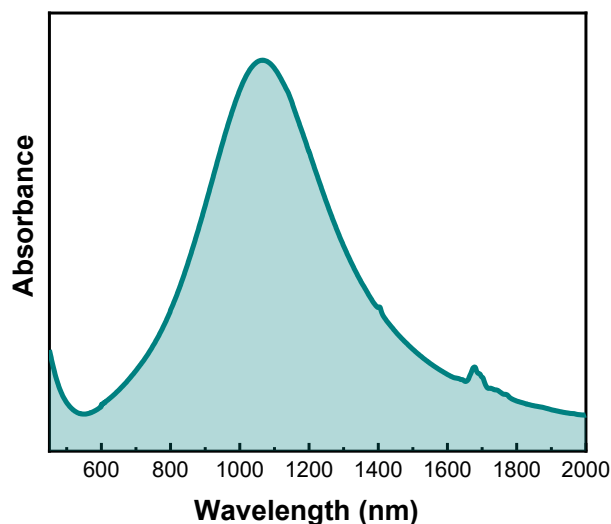
Figure 5.6 *Absorption spectrum of 4.4 nm-sized Cu$_{2-x}$Se NCs.*

Absorption spectra in *Figure 5.7a* indicate dampening of the LSPR, which is a profound indication of the filling of Cu vacancies[69, 153] and thus proves a successful CE reaction. The absorption spectra reveal the presence of a broad shoulder around 900–1000 nm, indicating the first electronic transition, which is generally observed in small CISe NCs.[97, 98] Such shoulder in the absorption spectra of CZISe NCs was also reported by Du et al., wherein their 4 nm-sized NCs exhibited a shoulder around 860–980 nm depending on the synthesis temperature.[147] Featureless absorption generally observed in I-III-VI-based NCs is attributed to the inhomogeneous composition of the NC ensemble.[21, 103] Thus, the presence of excitonic features in the NCs synthesized is an additional indication of their homogenous composition, and uniform size and shape. For higher In:Zn ratios one can distinguish an additional broad shoulder at around 850 nm, which can be attributed to the second electronic transition, a phenomenon practically not observed in I-III-VI-based NCs. As far as the composition dependence of the onset of absorption is concerned, a blue shift with the increase in Zn content was observed. The NCs with the In:Zn ratio of 0.81 and 0.82 exhibited the most blue shifted onset at 1050 nm. For the higher In:Zn ratios, i.e., a lesser amount of Zn, the absorption onset was slightly red shifted. It is a general observation wherein a larger Zn content leads to widening of the band gap and a resulting blue shift of absorption onset. For example, it was

observed by Zhang et al. that the absorption onset of CZISe NCs exhibited a blue shift due to increased Zn amount.[112] Similar widening of the band gap reflected in the blue shift of absorption band was observed by De Trizio et al. by incorporation of Zn^{2+} via partial CE into pre-synthesized CIS NCs.[115]
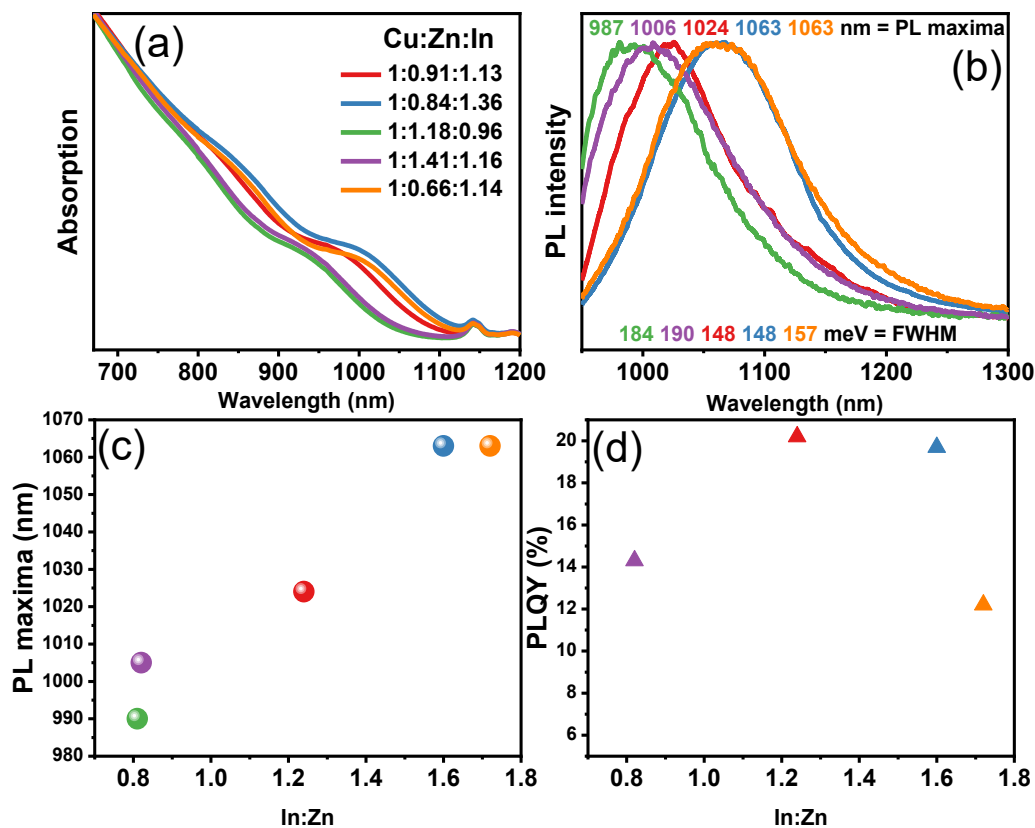
Figure 5.7 *Absorption (a) and PL (b) spectra of CZISe NCs with Cu:Zn:In atomic ratios of 1:0.91:1.13, 1:0.84:1.36, 1:1.18:0.96, 1:1.4:1.16, and 1:0.66:1.14. Trend of PL maxima (c) and PLQY (d) plotted vs. In:Zn atomic ratio. A small peak in (a) at approx. 1140 nm is an absorption feature of the solvent.*

PL spectra of the various compositions of CZISe NCs synthesized are depicted in *Figure 5.7b*. It was interesting to note that the PL band widths obtained were significantly narrower, as compared to spectra generally reported for I-III-VI-based NCs. PL band widths are usually in the range of 300 meV and it was believed to be an intrinsic property of the material.[140, 141] Contrary to this, the single-particle studies pointed towards the underlying reason of the broad PL to be simply the sample heterogeneity. Zang et al. in their single-particle studies suggested that the PL band widths of CIS NCs can be narrowed to approx. 100 meV, the only challenge being the development of synthetic strategies for obtaining such narrow spectra.[141] Hinterding et al. also showed that the single particle linewidths were approximately two times narrower than the ensemble line widths of CIS core and CIS/CdS core/shell NCs.[160] This line broadening

was indeed attributed to the sample inhomogenity originating from polydispersity in size, shape, and composition. The ensemble PL band widths of the synthesized CZISe NCs could be narrowed to the range of 150–190 meV, which can be attributed to the structural homogeneity, also supported by the absence of multiple features in the PL spectra.[12, 111] PLQY values of these NIR-emitting NCs were determined with the highest PLQY of 20.2% observed for CZISe NCs with In:Zn ratio of 1.24. Subsequently, CZISe NCs with In:Zn of 1.60 exhibited PLQY of 19.7% followed by In:Zn ratio of 0.81 with PLQY of 14.3%, and finally In:Zn ratio of 1.72 with PLQY of 12.2%. Thus, PLQY values did not follow a particular trend with varying In:Zn ratio (see *Figure 5.7.d*), but the stoichiometric feed ratio of Cu:In:Zn resulted in the highest value of PLQY.

The PLQY of ternary/quaternary I-III-VI-based NCs can be increased considerably with the growth of a shell. E.g., PLQY as high as 60% has been reported for CISe/ZnS core/shell NCs.[145, 161] An enhanced PL was also observed in the case of sequential CE on Cu_2S NCs resulting in a ZnS-rich surface leading to the formation of a gradient type CZIS/ZnS structure rather than a homogenously alloyed one.[68] However, the authors observed no PL in the case of simultaneous CE. PLQY reported previously by our group for CISe/ZnS NCs was <1%,[21] thus a many-fold increase in PLQY was achieved with this synthetic strategy. The enhancement of the PL efficiency can be directly related to the incorporation of Zn^{2+} as was shown by De Trizio et al. in the case of $Cu_{1-x}InS_2$, wherein partial CE with Zn resulted in record PLQY values of 80%.[115] Zn^{2+} cations tend to fill defects on the NC surface thus eliminating the channels for non-radiative recombination. TRPL traces of these CZISe NCs are presented in *Figure 5.8*. The average PL lifetime values estimated from these TRPL traces are 120 ns, 154 ns, 223 ns, and 115 ns for CZISe NCs with Cu:Zn:In ratios of 1:0.91:1.13, 1:0.84:1.36, 1:1.41:1.16, and 1:0.66:1.14, respectively. In general, Cu-chalcogenide-based NCs exhibit very long PL lifetime values in the range of hundreds of ns.[130, 133] Long radiative lifetimes of these NCs can be attributed to delay due to the complex recombination mechanism proceeding through intra gap states. In addition, the decay curves belonging to Cu-chalcogenide-based NCs cannot be fitted by single exponential functions, which represents multiple recombination pathways existing in the NC ensemble.[130, 136, 162]
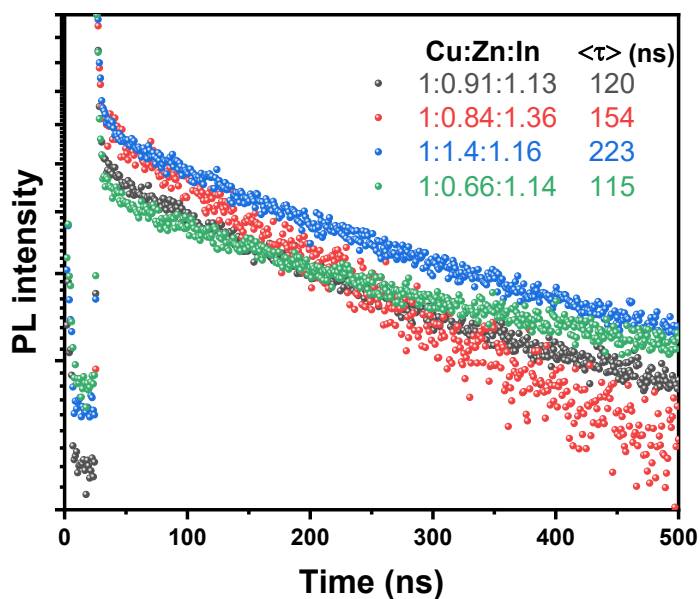
Figure 5.8 *TRPL traces of CZISe NCs with Cu:Zn:In ratio of 1:0.91:1.13, 1:0.84:1.36, 1:1.41:1.16, and 1:0.66:1.14.*

Previous studies have shown that the addition of Zn introduces a blue shift of the PL maxima which is attributed to the widening of the band gap.[115] Consequently, a larger Zn^{2+} content will result in a more pronounced blue shift of PL maxima. For instance, Liu et al. tuned the PL maxima of 2.6 nm-sized CZISe NCs synthesized via aqueous approach in the range of 600–800 nm with larger Zn content leading to a blue shift.[163] However, in this work a simultaneous CE is carried out and the final position of PL maxima would undoubtedly depend on the both In and Zn content, therefore it is reasonable to plot the PL maxima vs. the In:Zn ratio to deduce a possible composition dependence (*see Figure 5.7c*). The ratio of Cu to the sum of total guest cations for all samples was practically constant with the compositions of Cu:Zn:In of 1:0.9:1, 1:0.8:1.4, 1:1.2:0.9, 1:1.4:1, and 1:0.6:1.2 yielding Cu:(In+Zn) of= 0.48, 0.45, 0.46, 0.4, and 0.5, respectively. This means that the variation of optical properties can simply be attributed to the relative ratio of incoming cations. Regarding the composition dependence of the PL, a blue shift with the increase in the Zn content vs. In was observed. For the In:Zn ratio of 0.81 and 0.82 the most blue shifted emission at 987 nm and 1006 nm was observed. With the further increase in In content, leading to a In:Zn ratio of 1.2, the PL maximum was slightly red shifted to 1024 nm. Consequently, an even higher In:Zn ratio of 1.6 and 1.7 led to the most red shifted emission at 1063 nm. Thus, the PL maxima could be tuned from approx. 980 nm to 1060 nm by a simple variation of the ratio of incoming cations in the same size range.

5.1.5 Ligand exchange

The as-synthesized NCs were capped with OlAm and DDT, long-chain organic ligands, revealed by an intensive characteristic C–H band in the FTIR spectrum depicted in *Figure 5.9*. While the presence of ligands on the surface of the NCs is necessary for their growth and stability, the long-chain ligands also act as barriers for charge transfer and reduce electronic coupling between adjacent NCs.[66, 164, 165] Therefore, the long ligands on the surface of the NC core are in fact detrimental for the use of these NCs in various optoelectronic applications where efficient charge transport is required, e.g., in solar cells[66, 97, 147] and field effect transistors[66, 166]. To make CZISe NCs compatible for prospective applications, the parent ligands must be exchanged or removed. Such solution-based ligand exchange also simplifies the process of device fabrication, wherein film deposition via layer-by-layer ligand exchange can be avoided.[66] A ligand exchange can proceed through phase transfer of particles or can also be done in the same phase.
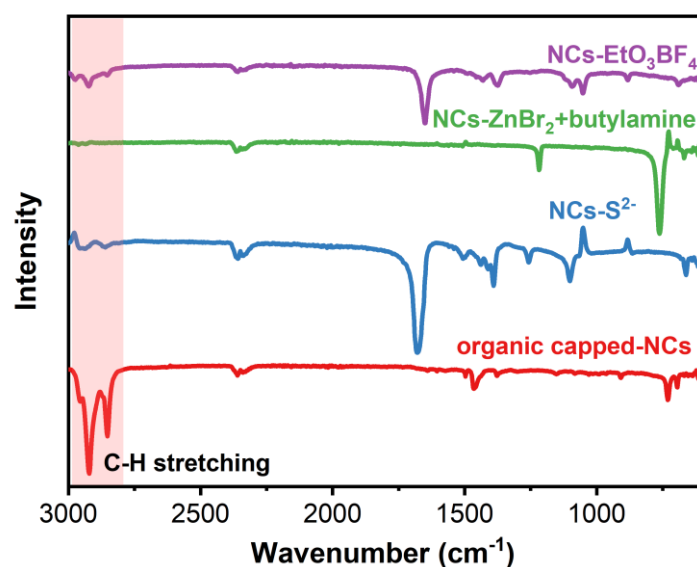
Figure 5.9 *FTIR spectra of CZISe NCs capped with different ligands.*

In the first attempt, the parent organic ligands (OlAm and DDT) were exchanged with inorganic sulfide ligands. For this, the NCs in hexane and ammonium sulfide in n-MFA forming a biphasic mixture were kept under stirring overnight resulting in the transfer of the NCs into the polar n-MFA phase, as shown in *Figure 5.10*.
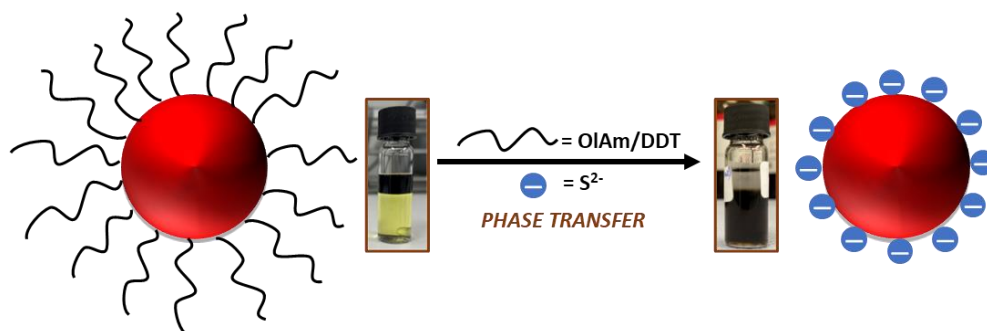
Figure 5.10 *Phase transfer and ligand exchange of CZISe NCs with sulfide ligands.*

The ligand exchange was further confirmed by the significant reduction of the –CH$_2$– band which is quite intense in the FTIR spectrum of as-synthesized NCs (see *Figure5.9*). Concentrated dispersions of CZISe NCs with the new ligands could also be prepared in DMF, which can then be directly used for device fabrication. The optical properties, i.e., absorption and position of PL maximum, remain unchanged after the exchange, as shown in *Figure 5.11a*, while PL intensity dropped due to the introduction of surface defects.
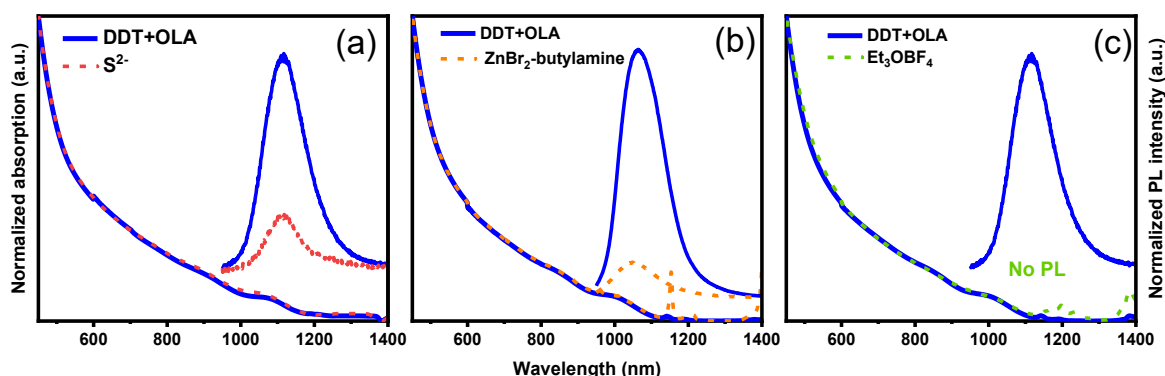
Figure 5.11 *Absorption and PL spectra of CZISe NCs before and after ligand exchange with S^{2-} (a), ZnBr$_2$-butylamine (b), EtOBF$_4$ (c).*

The second strategy was to exchange the parent organic ligands with ZnBr$_2$ and butylamine. ZnBr$_2$ solution in methanol was added to the NCs dispersion in toluene until it turned turbid, indicating the promotion of the ligand exchange. This turbid solution was reversed to a clear solution by adding butylamine. The ligand exchange was reflected in a decreased intensity of the –CH$_2$– band, as shown in the FTIR spectrum in *Figure 5.9*. Concentrated dispersions of ZnBr$_2$–butylamine-capped CZISe NCs could be prepared in chloroform, which might be useful for the fabrication of thin films via solution-based processing. Absorption and PL spectra depicted in *Figure 5.11b* of the QDs before and after exchange indicate that they remain unchanged, while PL intensity drops due to the introduction of surface defects.

The last strategy tested was adopted from Rosen et al., which led to the stripping off of the parent ligands,[142] as proven by the absence of the –CH$_2$– band in the FTIR spectrum (*Figure 5.9*). The NCs capped with BF$_4^-$ could be dispersed in DMF to form concentrated colloids. The absorption spectrum after the exchange remained the same, as depicted in *Figure 5.11c*, while PL intensity was significantly decreased due to the formation of surface defects, which can serve as centers for non-radiative recombination.

Thus, the surface modification of these NCs was possible despite the presence of strongly bound thiol ligands and concentrated batches of CZISe NCs could be prepared. These surface modified NCs could further be used for prospective applications, particularly in solar energy harvesting due to the suitability of the band gap of the material and its nontoxic nature.[97] While solar cells fabricated employing CZISe NCs with PCE of 13.6% have been reported,[112] further efforts to increase the PCE of the devices need to be undertaken.

5.1.6 Conclusions

In conclusion, in this work a simultaneous CE approach was adopted for the synthesis of alloyed CZISe NCs with considerably good PL properties. In particular, the FWHM was reduced to the range of 150–190 meV and the PLQY of the CZISe NCs was increased up to 20%. These properties are quite rarely observed in Cu-chalcogenide-based ternary/quaternary NCs without an additional shell growth. Furthermore, a relation between the optical properties and the composition of CZISe NCs was established. In agreement with the generally observed trend of an increasing blue shift with the increase in the Zn content, a blue shift of the PL maxima could be trigerred by increasing the Zn content. The increase in In content led to an opposite trend, i.e., the PL redshift. Thus, by controlling the ratio of In:Zn it was possible to tune the PL in the range of approx. 980–1060 nm. The organic ligands on the surface of the NCs synthesized could be exchanged with short chain ligands, thus decreasing the distance between adjacent NCs in the solids, which leads to enhanced electronic coupling. This possibility keeps the door for prospective applications of these NCs in solar energy harvesting open.

5.2 Seed-Mediated Synthesis of Cu-Zn-In-S Nanoplatelets with Inherent Photoluminescence in the Visible Range

This Section is based on the publication entitled 'Seed-mediated Synthesis of Photoluminescent Cu-Zn-In-S Nanoplatelets' (Chem. Mater. **2022***, 34, 9251–9260).*

5.2.1 Background and Aim

In the family of I-III-VI semiconductor NCs, most research has been carried out on CIS-based NCs.[21] Although the multiple reactive species present in the direct synthesis of CIS-based NCs result in poor size and shape control of the NC ensemble, rigorous research advances in this material have enabled the production of high-quality CIS-based NCs covered with a shell that have exhibited very high PLQYs.[115] However, 2D NCs of the multicomponent CIS family with well-defined optical properties, possessing strong PL, have very scarcely been researched compared to their 0D counterparts. 2D semiconductor NCs have recently gained significant interest due to their unique anisotropic properties.[20, 81, 116, 122, 167] These properties appear due to the strong quantum confinement in one dimension, because the thickness of these 2D NCs is typically significantly smaller than the corresponding Bohr radius. Also, 2D materials have been employed in a variety of applications, particularly in thin-film photovoltaics and optoelectronics with binary NCs essentially acting as functional units.[119, 123, 124, 168, 169] Thus, in the case of CIS-based NCs, the inherent features of this class of NCs combined with the anisotropy in NPLs/ NSs might result in new effects. Reports in literature for 2D I-III-VI-based NCs are rare, with very few reports of CIS-based 2D NCs that exhibit PL.[129] For instance, the CIS NPLs reported by Chen et al.[128] and Berends et al.[116] did not exhibit any PL. Thus, highly intensive PL originating from 2D morphologies of CIS NCs is an open research topic, which should be explored.

The aim of this project was to synthesize quaternary CZIS NPLs which exhibit inherent PL and better shape control than previously reported I-III-VI-based 2D NCs. With this aim, I-III-VI-based In-rich CZIS NPLs were synthesized wherein first In_2S_3 small NC seeds were synthesized in OlAm or in a mixture of OlAm and shorter chain OctAm. In_2S_3 serves as a suitable template for the synthesis of CIS NCs as was reported by Chen et al.[128] Thereafter, a small amount of Cu was incorporated into the In_2S_3 NCs to form CIS seeds. Consequently, these CIS seeds were then allowed to grow forming CIS NPLs. The obtained CIS NPLs were further subjected to a partial CE with Zn^{2+} leading to the formation of CZIS NPLs. The advantages of using a CE approach for the synthesis of multicomponent compositions has been discussed in *Section 2.5*. To establish the tuneability of the PL spectra, the composition of the NPLs was varied with a variation of the amount of Cu incorporated into the In_2Se_3 seeds. Aiming at the improvement of the stability and optical properties of the synthesized CZIS NPLs, they were covered with a shell of a wide bandgap semiconductor, ZnS.

5.2.2 Synthesis of CIS and CZIS NPLs

The synthesis of CZIS NPLs was carried out with a multistep one-pot method, as illustrated in *Figure 5.12*. The approach developed included the formation of CIS seeds by incorporating Cu^+ into In_2S_3 seeds with their subsequent recrystallization or oriented attachment into CIS NPLs. The CIS NPLs obtained were used to synthesize photoluminescent CZIS NPLs and CZIS/ZnS core/shell NPLs. As the first step of the synthesis procedure, In_2S_3 seeds were synthesized in pure OlAm or a mixture of long-chain (OlAm) and shorter-chain (OctAm) amines using a considerable excess of the In-precursor. The feed ratio was strategically chosen to be In-rich instead of a stoichiometric one to consume all sulfur in the first synthesis step and thus avoid the formation of the $Cu_{2-x}S$ phase in the subsequent steps through the direct reaction between the S- and the Cu-precursors. It was also observed that using a mixture of amines with carbon chains of various lengths resulted in unstacked CIS NPLs. On the other hand, using a single type of amine ligand led mostly to their partial stacking, reflected in the formation of gelly-like precipitates which could be redispersed upon ultrasonication. It was also noted that this reversible stacking in the case of the single ligand synthesis did not affect optical properties of the final NPLs. This demonstrated that the presence of a disordered ligand shell on the NPLs' surface increases C–C σ-bond rotation/bending freedom of the molecules, providing higher solubility of the NPLs.[170, 171] Alkylamines in general also play a significant role in the 2D anisotropic growth of the NCs by preferential attachment to the top and bottom facets, blocking monomer addition on these basal planes.[116]
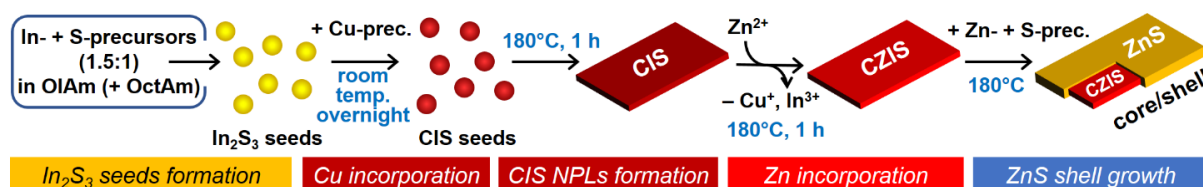
Figure 5.12 *Scheme of the synthesis of CZIS core and CZIS/ZnS core/shell NPLs starting from In_2S_3 seeds.*

In_2S_3 seeds were obtained in the reaction between $InCl_3$ and S powder dissolved in OlAm or a mixture of OlAm and OctAm at 100ºC for 1 h. This was followed with the addition of various amounts of $[Cu(CH_3CN)_4]PF_6$ to the In_2S_3 seeds at room temperature to form CIS seeds with different compositions (i.e., the ratio between Cu and In). This addition of Cu was accompanied by an immediate color change from yellow to light brown that indicated the formation of CIS seeds. Following this, the as-synthesized CIS seeds were kept overnight under stirring at room temperature to eliminate other simultaneous processes which might take place

at higher temperature due to the presence of multiple reactive species. Next day, the CIS NC seeds were heated to 180°C for the growth of the NPLs. The as-synthesized NPLs were unstable, and therefore, 1 mL of DDT was added at room temperature and kept under stirring for 1 h. DDT serves as a reducing agent thus preventing the oxidation of Cu^+, leading to enhancement of their stability. In the next step, partial CE was carried out to improve the optical properties and stability of the NPLs through the incorporation of Zn^{2+} into the as-synthesized CIS NPLs, leading to the formation of alloyed quaternary CZIS NPLs. This partial CE exchange was performed using zinc 2-ethylhexanoate directly injected into the crude reaction mixture with further heating at 180°C for 1 h. As a final step for the augmentation of PL intensity, a ZnS shell was grown around these NPLs using $Zn(DDTC)_2$ which can serve as a single source for both Zn and S. The formation of separate ZnS nanoparticles as a by-product was avoided by slowly adding $Zn(DDTC)_2$ dissolved in OlAm, using a syringe pump that yielded solely CZIS/ZnS core/shell NPLs.

The addition of $[Cu(CH_3CN)_4]PF_6$ to the In_2S_3 seeds is a critical step which changes the path of further crystallization and growth. A control experiment was carried out without the addition of the Cu-precursor but under the same reaction conditions, which resulted in hexagonally shaped In_2S_3 NPLs as shown in *Figure 5.13a*. The morphology of these NPLs was similar to the In_2S_3 NPLs synthesized by Park et al. using a stoichiometric In:S ratio.[144] This control reaction indicates that the addition of even small amounts of the Cu-precursor drastically affects the morphology of the NPLs, which is triggered by the change in the crystal structure from tetragonal β-In_2S_3 to a tetragonal chalcopyrite CIS (*Figure 5.15*). As depicted in *Figure 5.13b-d*, the addition of 2%, 5%, and 10% of Cu wrt In resulted in the formation of thin rectangular NPLs with an average lateral size of 30×8 nm^2. The thickness of the NPLs was difficult to determine precisely, as they did not form sufficiently large stacks where the NPLs can be observed vertically oriented on a grid. Their thickness could be approximated to be about 1 nm by analogy with the thickness of the In_2S_3 NPLs determined by TEM measurements of their stacks.[144] The increase in the Cu-precursor amount above 10% with respect to In led to the formation of small NCs as by-products along with the desired NPLs, as shown in *Figure 5.13e*. A further increase to 15% of the Cu-precursor did not lead to the formation of NPLs, and only small spherical particles were observed (*Figure 5.13f*). This change in the NC growth may be attributed to the significant distortion of the seeds upon adding more copper, which hinders their oriented attachment and thus the formation of the NPLs. As follows from these results, an optimal amount of $[Cu(CH_3CN)_4]PF_6$ is required to form CIS NPLs with a

significant Cu content, while a larger amount of the precursor leads to a change in morphology, resulting in small spherical NCs.
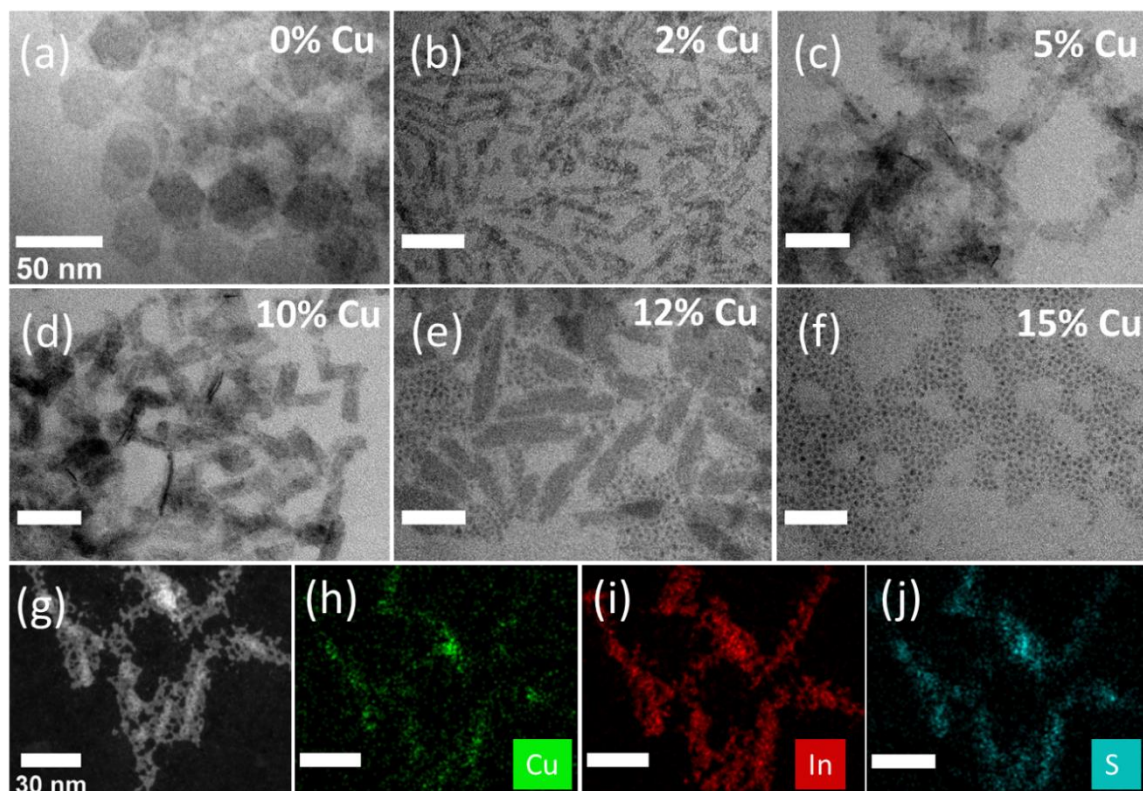
Figure 5.13 *Conventional TEM images of In$_2$S$_3$ NPLs (a), and CIS NPLs with 2% (b), 5% (c), 10% (d), 12% (e), and 15% (f) of Cu relative to In. HAADF-STEM image (g) and corresponding EDXS-based element maps of Cu (h), In (i), and S (j), displaying the element distribution across the CIS NPL. All scale cale bars in (a-f) are 50 nm, and in (g-j) are 30 nm.*

ICP-OES results summarized in *Figure 5.14* and *Table 5.2* show that with increasing Cu/In feed ratio from 0.02, through 0.05 to 0.1, the corresponding Cu/In ratio in the CIS NPLs also increased with final values of 0.09, 0.14, and 0.31, respectively. The STEM-EDXS element maps displayed in *Figure 5.13h-j* further proved the presence of Cu in the NPLs. The distribution of Cu appeared to be rather inhomogeneous with a more homogenous distribution of In and S over individual NPLs. This uneven copper content reflects the mechanism of the NPL formation from small NC seeds, in which copper is most probably located mainly on the surface. After arranging into the CIS NPLs copper ions remain confined.
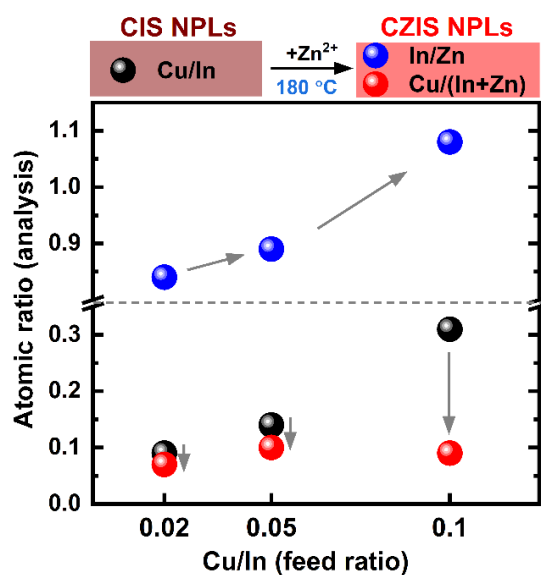
Figure 5.14 *ICP-OES-based analysis of the cation ratios in CIS and CZIS NPLs relative to the feed ratios used in the synthesis.*

Table 5.2 *Final Cu/In and Cu/Zn/In ratios of the CIS NPLs and CZIS NPLs, respectively, from the results of ICP-OES analysis, as well as average sizes of the CZIS NPLs.*

Sample (Cu% relative to In)	Composition (Cu/In) of CIS NPLs	Composition (Cu/Zn/In) of CZIS NPLs	Average lateral size (nm^2)
2% Cu (molar = 1/50)	1/11.1	1/7.7/6.5	31×8
5% Cu (1/20)	1/7.2	1/5.4/4.8	30×8
10% Cu (1/10)	1/3.2	1/5.1/5.5	38×11

Even though I-III-VI-based NCs generally crystallize in a tetragonal or cubic phase depending on their composition and reaction temperature,[95, 104] the existence of a metastable hexagonal wurtzite structure was also observed in the case of nanostructured materials of this group[110]. The CE pathway explained in *Section 2.5* is a feasible route of accomplishing such a metastable crystal structure. In this scenario, a hexagonal binary phase is chosen as the starting template, which is maintained after the addition of guest cations.[95,68] Thermodynamically stable tetragonal phases are generally observed when NCs are produced via direct synthesis involving molecular precursors of all components. Specific ordering of the metal atoms rather than a random distribution of Cu and In atoms leads to the preferential adoption of the tetragonal phase. The tetragonal phase of I-III-VI NCs is derived from the cubic zinc-blende structure in which the tetragonal distortion is introduced due to the different lengths of the I-VI and III-VI

bonds in the crystal.[172] Also for Cu-deficient species, the distortion increases with a decrease in the Cu/In ratio, where the tetragonal distortion becomes more pronounced as the crystal becomes more and more Cu-deficient.[105] Such a tetragonal crystal structure was also observed in the case of the synthesized CIS NPLs which are also Cu-deficient (*Figure 5.15*). The positions of the Bragg reflections match with the CIS chalcopyrite tetragonal phase (JCPDS-ICDD - C38-777) with two pronounced reflections at 27.8° and 48° that correspond to the planes lying in the lateral directions. The strongly asymmetric shape of the first peak can be assumed to be due to the contribution from relatively intensive peak at 32.7°. On the other hand, In_2S_3 NPLs with hexagonal shape crystallized in the tetragonal β-In_2S_3 crystal phase (JCPDS-ICDD - C25-390), as was observed by Park et al.[144] This indicates that the introduction of Cu led to the adoption of the CIS chalcopyrite structure, which in turn led to the formation of differently shaped NPLs.
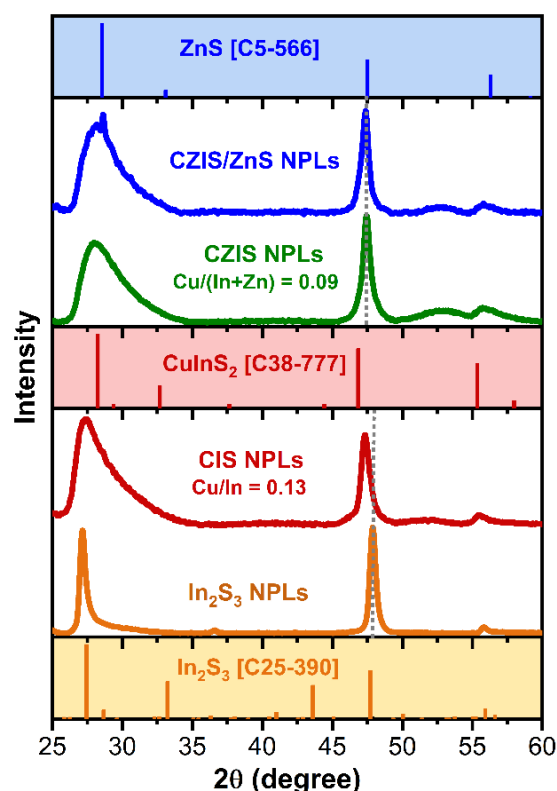
Figure 5.15 *XRD patterns of In_2S_3, CIS, CZIS, and CZIS/ZnS NPLs with corresponding bulk references of In_2S_3 (C25-390), CIS chalcopyrite (C38-777), and ZnS sphalerite (C5-566) structures from the JCPDS-ICDD.*

Incorporation of Zn^{2+} into CIS NPLs via partial CE led to the improvement of their shape, as depicted in the TEM images of *Figure 5.16a–c*. Resulting CZIS NPLs did not form stacks and exhibited a well-defined rectangular morphology. The TEM images reveal that the platelets

are fairly monodispersed with lateral sizes of ~30×10 nm². This better defined shape of the CZIS NPLs allowed the precise determination of their thickness via HRTEM analysis of vertically stacked NPLs, as exemplarily shown in *Figure 5.20a*, with an average value of 1.1±0.08 nm. The incorporation of Zn perhaps fills the surface defects which, along with the enhancement of optical properties, leads to proper development of the NPL shape. Successful embedding of Zn²⁺ was revealed by the STEM-EDXS element mapping indicating its presence along with Cu and In in the CZIS NPLs (*Figure 5.16e–h*). As compared to the CIS NPLs, the distribution of Cu in these NPLs appears to be more homogenous along with the distribution of other cations.
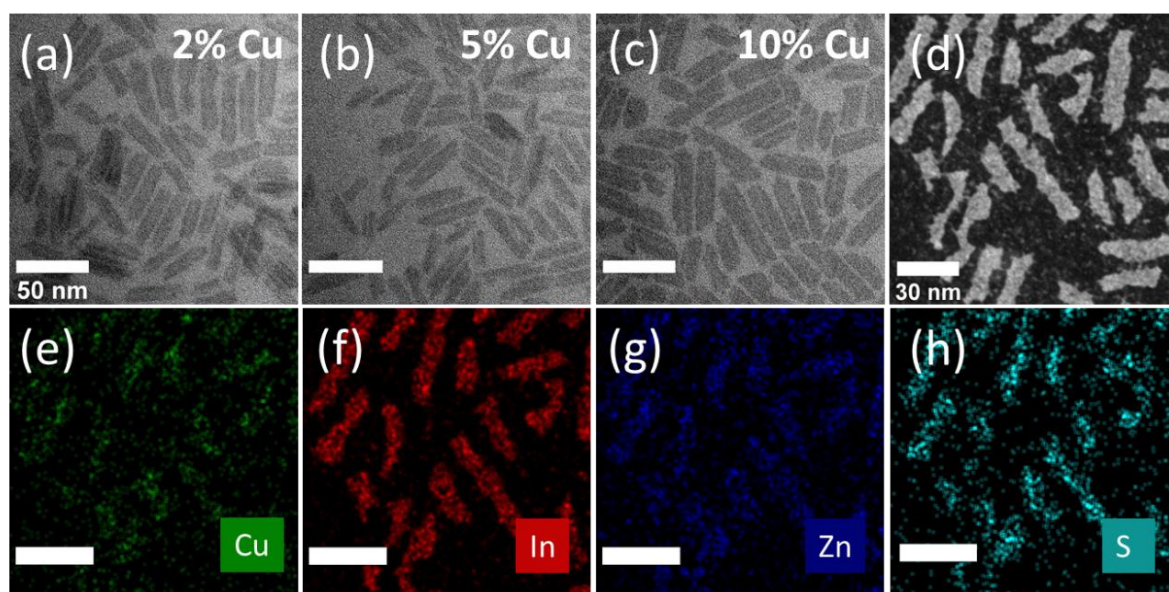
Figure 5.16 *Conventional TEM images of CZIS NPLs with Cu:(In+Zn) ratio of 0.07 (a), 0.09 (b), and 0.1 (c). HAADF-STEM image (d) and corresponding EDXS-based element maps of Cu (e), In (f), Zn (g), and S (h) of CZIS NPLs with Cu/(In+Zn) ratio of 0.09. All scale cale bars in (a-c) are 50 nm, and in (d-h) are 30 nm.*

The surface of the synthesized CZIS NPLs was studied using FTIR spectroscopy. Analysis of the obtained spectrum indicates the presence of both types of the ligands, i.e., thiol- and amine-functionalities on the NPL surface (*Figure 5.17*). Thus, long-chain organics were bound to the surface of the NPLs and consequently, the use of these particles in future applications where an efficient charge transport is essential, would require a post-synthetic surface modification of the NPLs, wherein these ligands are exchanged with other short-chain ligands.
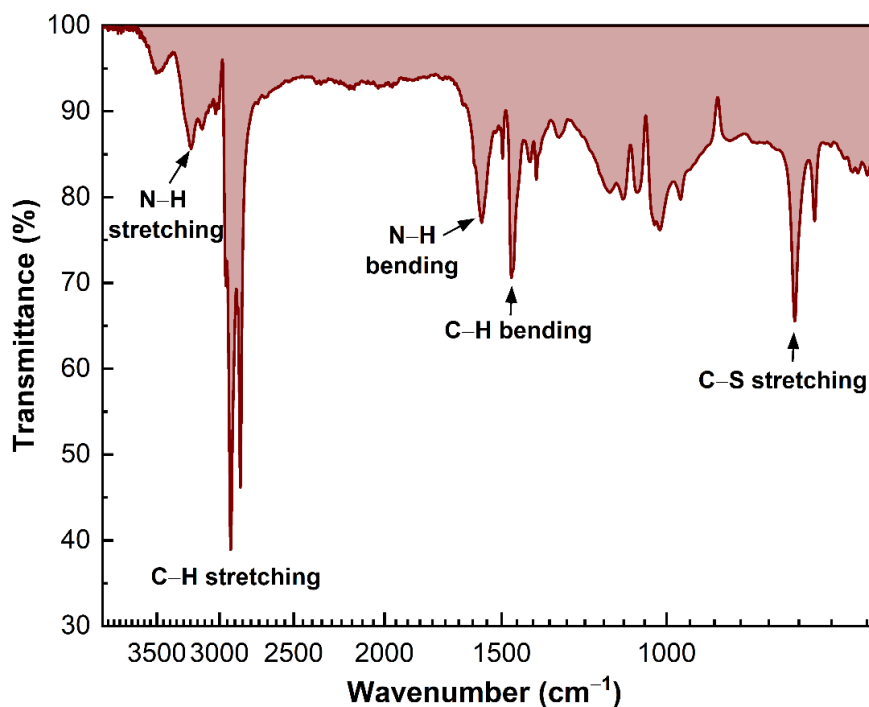
Figure 5.17 *FTIR spectrum of CZIS NPLs.*

As follows from the ICP-OES results presented in *Figure 5.14* and *Table 5.2*, the Cu content decreases upon the incorporation of Zn in the CIS NPLs. While the initial CIS NPLs exhibited Cu/In ratios of 0.09, 0.14, and 0.31, after the treatment with the Zn-precursor the CZIS NPLs had Cu/(In+Zn) ratios of 0.07, 0.10, and 0.09, respectively, revealing more efficient Cu^+-to-Zn^{2+} CE in CIS NPLs. The In/Zn ratio in all CZIS NPLs was in the range of 0.84–1.08. It should be noted that the multistep synthesis was performed in one-pot with successive addition of the necessary precursors and without purification of the product after every stage. Based on this, the probability of multiple competing processes, such as Cu^+-to-Zn^{2+}, In^{3+}-to-Zn^{2+}, Cu^+-to-In^{3+} CE reactions, cannot be neglected which make it challenging to interpret the obtained data.

XRD analysis revealed that the NPLs maintained their crystal structure after the incorporation of Zn (see *Figure 5.15*). This agrees with literature data suggesting that Cu-deficient CZIS crystallizes in the tetragonal phase.[20, 115, 129] As in the case of CIS NPLs, in the diffractogram of the resulting CZIS NPLs, two narrow and pronounced sharp reflections at 27.8° and at 48° correspond to the planes in the lateral direction of the NPLs, while a broad peak at approx. 56° can be assigned to lattice planes lying in the thickness direction. The pattern observed is a result of the formation of anisotropic 2D NCs. This was confirmed with the XRD pattern of CZIS QDs obtained by adding 15% of the Cu-precursor represented in *Figure 5.18* which shows only broad reflections that correspond to isotropic nanoparticles. The change in

composition did not lead to a remarkable shift of the peak positions, while a small shift to larger 2 theta values as compared to the reference is found to be consistent for all compositions, most likely due to the replacement of In^{3+} with Zn^{2+}.
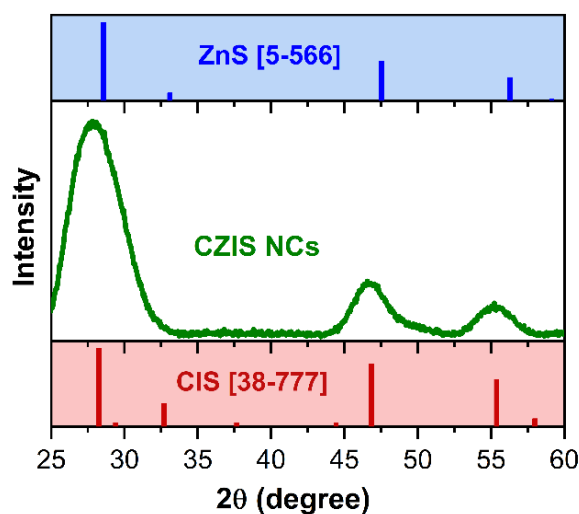
Figure 5.18 *XRD pattern of the sample obtained after adding 15% of the Cu-precursor with subsequent Zn incorporation with corresponding bulk references of CIS chalcopyrite (JCPDS-ICDD - C38-777) and ZnS sphalerite (JCPDS-ICDD - C5-566) structures.*

5.2.3   Synthesis of core/shell NPLs

With the aim of further enhancing the stability and improving optical properties of CZIS NPLs, they were overcoated with a ZnS shell. ZnS was chosen as the shell material because it has a small lattice mismatch with CIS (i.e., 2 %) and a larger band gap, as compared to bulk CIS, which results in a type-I band edge alignment with CIS.[36, 161] Several strategies of the shell growth were tested. In the first one, $Zn(DDTC)_2$ dissolved in OlAm was used as the shell precursor which is highly reactive and serves as a source of both Zn and S. Reactivity of the shell precursor plays an important role in the kinetics of heteroepitaxial growth as well as in homogenous nucleation. The use of a highly reactive precursor for the shell growth promotes the heteroepitaxial nucleation and growth of the shell instead of other competing processes that can take place, such as CE, etching, or alloying.[36] In this work, two approaches of the shell precursor addition were adopted: rapid hot-injection and slow addition. In the first, the Zn-precursor was injected directly into the crude reaction mixture of CZIS NPLs at 180°C and the temperature was maintained for 1 h. It was reported that a higher temperature favors the heteroepitaxial growth of the shell, while lower temperatures favor CE reactions.[36, 173] The highest possible temperature of 180°C was chosen for the shell growth, since the presence of OctAm in the reaction mixture does not allow further increase of the temperature due to its boiling point of 180°C. A TEM image in *Figure 5.19a* shows that after the shell growth, along

with the NPLs, small spherical particles were also formed as by-products. These particles are probably ZnS NCs formed because of the secondary homogenous nucleation along with the heteroepitaxial growth of the ZnS shell.
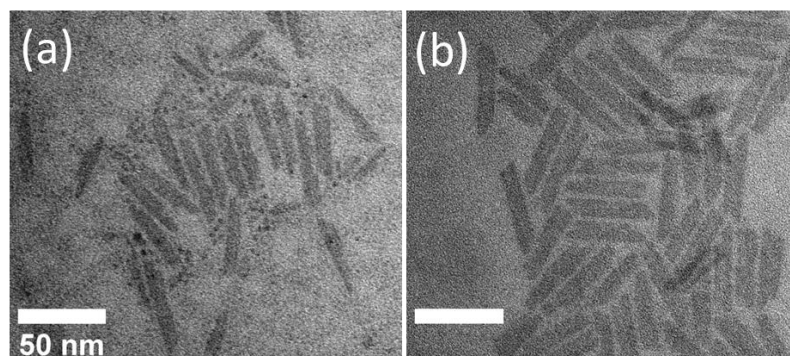
Figure 5.19 *CZIS/ZnS core/shell NPLs synthesized using a rapid injection (a) and a slow injection (b) of the shell growth precursor.*

Therefore, to avoid the formation of additional by-products, instead of a rapid injection of the Zn-precursor, its slow and controlled addition was carried out using a syringe pump. Due to the low monomer concentration, the slow addition should not promote the secondary homogenous nucleation, thus preventing the formation of ZnS NC by-products and result in a narrower size distribution.[45, 46, 111, 136, 174] Indeed, the resulting NPLs were fairly monodisperse with no by-products as indicated by the TEM image of CZIS/ZnS NPLs in *Figure 5.19b*. Along with the shell deposition, the NPLs also grew laterally with an increase in size from 34×8 nm^2 of the parent CZIS NPLs to 42×9 nm^2 of the CZIS/ZnS core/shell NPLs. This increase in their lateral size was perhaps due to the seeded growth of the core since unreacted precursors could still be present in the reaction mixture. The growth of the shell took place preferentially in the thickness direction and was confirmed by HRTEM imaging of vertically oriented stacks of the NPLs before and after the shell growth. As can be seen in HRTEM images displayed in *Figure 5.20*, a pronounced increase in the NPL thickness from 1.1 ± 0.08 nm to 1.6 ± 0.2 nm occurs after the shell growth. This means that the shell thickness was approximately 1 monolayer (i.e., half of the lattice parameter) on each facet of the NPL.[145] As seen in *Figure 5.15*, after the shell growth, the initial crystal structure of the NPLs was maintained, and no shifts of the peak positions were observed in the diffractogram. The positions of the Bragg reflections in both core CZIS NPLs and core/shell CZIS/ZnS NPLs match well with the CIS roquesite (JCPDS-ICDD - C27-159) and ZnS sphalerite (JCPDS-ICDD - C5-566) crystal structures. The peak at 48° in both patterns matches better with the ZnS sphalerite reference, which is due to the

incorporation of Zn in the core and to the fact that the NPLs are Cu-poor, i.e., they have a structure closer to In_2S_3 (see *Figure 5.15*).
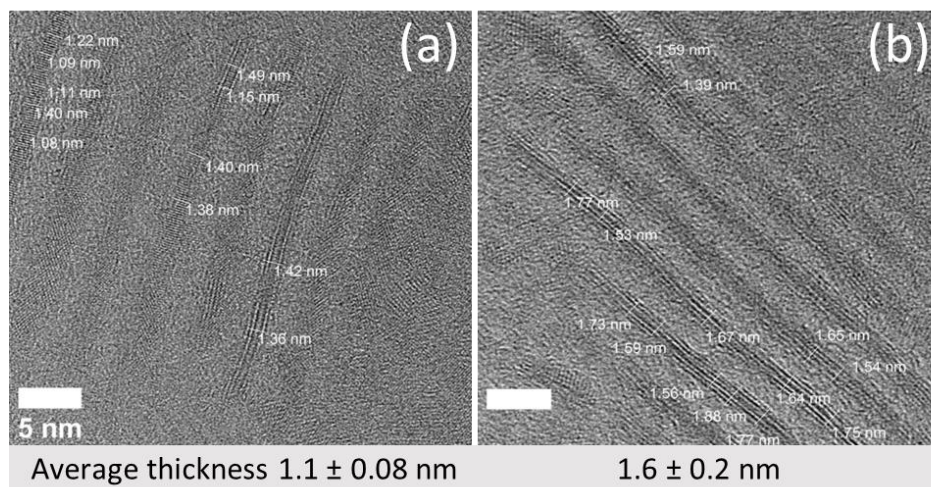
Figure 5.20 *HRTEM images of vertically oriented stacked core CZIS (a) and core/shell CZIS/ZnS (b) NPLs with corresponding average thickness values.*

Since using the abovementioned procedures only 1 monolayer thick shell was grown, subsequent attempts to grow a thicker ZnS shell, which would further enhance the stability and the optical properties of the synthesized NPLs, were carried out. It was speculated that the presence of strongly bound thiol ligands on the NC surface could be the reason for the inability to form a thicker ZnS shell. Berends et al. pointed out that the purification of CIS NCs has a significant impact on the following shell growth process due to the surface chemistry of the NCs and the presence of residual ligands and precursors.[36] Therefore, applying the second strategy of the shell deposition, CZIS NPLs were first purified once and then dissolved in a mixture of ODE, OctAm, and OlAm. This mixture was used for the shell growth upon slow addition of $Zn(DDTC)_2$ in OlAm. However, the TEM image in *Figure 5.21a* reveals etching of the resulting CZIS/ZnS NPLs. The particles were somewhat stacked and did not maintain the morphology of the parent CZIS NPLs. To confirm the role of DDT in the inhibition of the formation of a thicker shell, crude CIS NPLs without addition of DDT and the Zn-precursor were used as the cores in the same procedure. In this case, TEM imaging revealed that the resulting CIS/ZnS NPLs remained stacked, and the growth of a thicker shell was also unsuccessful (see *Figure 5.21b*).
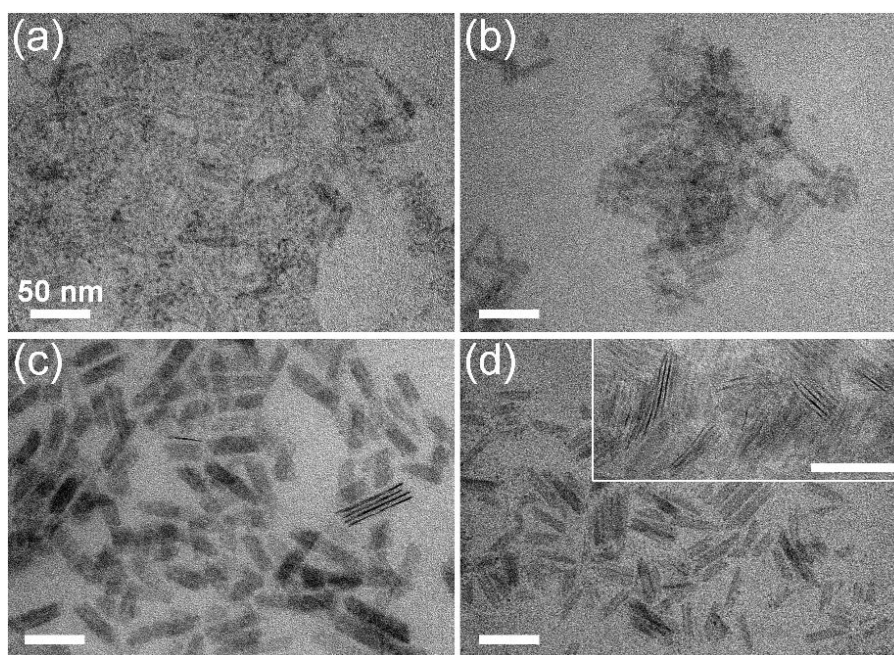
Figure 5.21 *Conventional TEM images of CZIS/ZnS core/shell NPLs (a), CIS/ZnS core/shell NPLs (b), CZIS/ZnS NPLs synthesized via colloidal ionic layer deposition (c), and CZIS/In$_2$S$_3$ NPLs (d). Inset in (d) shows a TEM image of the corresponding NPLs forming stacks. All scale bars are 50 nm.*

In the third strategy, the colloidal ionic layer deposition method for the shell growth reported by Meerbach et al. was employed.[143] This method, wherein a controlled sequential deposition of anion and cation half layers is carried out at room temperature, has a number of advantages: narrow size distribution and shape uniformity, control over surface composition and ligand chemistry, considerable reproducibility of the shell growth at room temperature.[175] A TEM image in *Figure 5.21c* shows product NPLs with a higher contrast and a thickness of about 2 nm indicating that a comparatively thicker shell was grown after the deposition of two ZnS monolayers. Finally, in the fourth strategy, instead of ZnS an In$_2$S$_3$ shell was grown. In$_2$S$_3$ has a larger band gap of 2.0–2.3 eV[128] than CIS with a band gap of 1.5 eV[21] and thus should result in the type I band alignment. TEM image of the synthesized NPLs in *Figure 5.21d* reveals that NPLs with a similar morphology and size were also formed in this case. At the same time, no increase in the thickness of the shell was observed (inset in *Figure 5.21d*). Therefore, it can be concluded that the deposition of a thick shell was impossible in the case of these NPLs, perhaps due to interfacial strain between the core and the shell.

5.2.4   Optical properties of CIS, CZIS, and CZIS/ZnS NPLs

The evolution of the optical spectra from In$_2$S$_3$ to CZIS/ZnS core/shell NPLs is displayed in *Figure 5.22*. As seen in *Figure 5.22a*, the addition of the Cu-precursor to In$_2$S$_3$ seeds led to a

redshift in the absorption spectra, the magnitude of which depends on the precursor amount. The absorption spectra of CIS NPLs with different compositions, shown in *Figure 5.22b*, exhibit a pronounced shoulder at approx. 530 nm representing the first electron transition, which is generally observed in small I-III-VI NCs.[21, 95, 130] Increasing copper content in the NPLs resulted in a small redshift of this shoulder as well as the onset of absorption spectra (*Figure 5.22b*, inset). It also led to the appearance of a pronounced shoulder at approx. 410 nm, whereas the UV-part of the spectra remains practically unchanged. In the NPLs with a Cu/In ratio of 0.09 and 0.14, no PL signal was observed, while the sample containing larger Cu amount (Cu/In = 0.31) possessed a weak emission in the red part of the visible spectrum. It can be assumed that the observed low PL intensities and a broad PL band width are due to the presence of numerous internal and surface defects and not uniform size and inhomogeneous composition of the NPLs discussed above.[130]
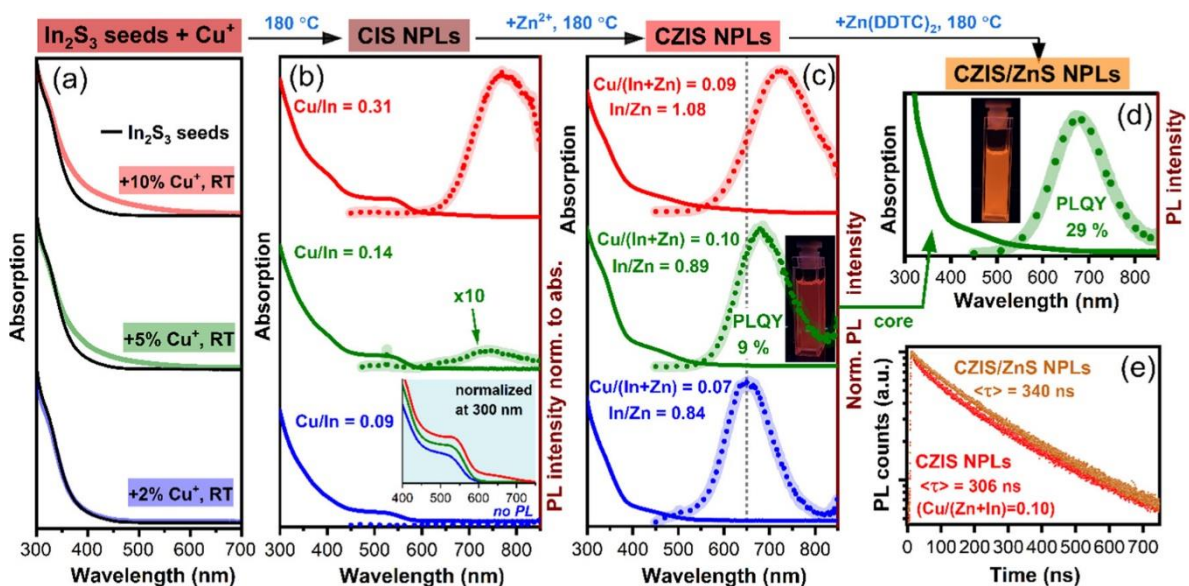
Figure 5.22 *Absorption spectra of In₂S₃ and CIS seeds (a), absorption and PL spectra of CIS (b), CZIS (c) and CZIS/ZnS core/shell (d) NPLs. The inset in (b) displays the absorption spectra of the CIS NPLs normalized at 300 nm. PL lifetime measurements of CZIS and CZIS/ZnS NPLs (e). The insets in (c) and (d) are photos of CZIS and CZIS/ZnS NPL dispersions, respectively, under UV-light.*

Subsequent incorporation of Zn indeed significantly improved the emission intensity of the NPLs, shifting the absorption onsets and the PL maxima to shorter wavelengths, as compared to the CIS NPLs due to the increasing band gap (see *Figure 5.22c*). By this, absorption spectra became practically featureless without the pronounced shoulders observed for CIS NPLs. Here, the positions of the PL spectra demonstrated a blue shift from 721 nm for

Cu/(In+Zn) = 0.09 through 666 nm for Cu/(In+Zn) = 0.10 to approx. 650 nm for the CZIS NPLs sample with the smallest Cu content (Cu/(In+Zn) = 0.07). As seen in *Figure 5.22c*, PL spectra of CZIS NPLs also exhibited large Stokes shifts and significantly broad PL band widths. These features are typically observed in I-III-VI-based NCs. The FWHM values of the synthesized NPLs were 340 meV, 325 meV, and 370 meV for the CZIS NPL samples with Cu/(In+Zn) ratios of 0.07, 0.10, and 0.09, respectively. According to the literature data, small spherical CIS NCs of approx. 2.5 nm size having chalcopyrite structure exhibited broad PL band widths of approx. 300 meV.[136] Similarly, in wurtzite CIS NCs, size-dependent FWHM values were reported ranging from 300 to 320 meV in 2.7–7.2 nm particles.[176] In general, it can be stated that broad PL with FWHM > 300 meV is commonly observed in CIS-based NCs which is mainly attributed to the ensemble heterogeneity of size and composition.[130, 140, 141] Single-particle studies support this claim, wherein a FWHM as narrow as 60 meV was reported for single NCs as compared to the broad FWHM of 300 meV of the ensemble.[141] At the same time, in striking contrast to the corresponding small CZIS NCs, the PL of the CZIS NPLs was dramatically redshifted. For example, 2.4 nm CZIS NCs with a small copper content (Cu/(In+Zn) = 0.05–0.1) were reported to have the PL in the range of 550–580 nm,[177] hundred nm shorter than for the NPLs in this work, despite a remarkably smaller size of the latter in the thickness dimension. This large difference implies the presence of quite strong 1D quantum confinement.

As discussed in *Chapter 3*, the most widely accepted mechanism of the emission process in CIS (CISe)-based NCs is recombination of the photoexcited electron from the conduction band to an intrastate Cu related defect which can be either associated with Cu^+ or Cu^{2+}.[108, 136, 137, 139-141, 178] This recombination mechanism explains the characteristic emission features of I-III-VI-based NCs, viz., broad band widths, large Stokes shift, long radiative lifetimes, etc.[130] Whereas Cd-chalcogenide NPLs are monodisperse in the thickness dimension and show strong quantum confinement leading to considerably narrow emission band widths,[25, 122, 179, 180] contrary to this observation, PL bands observed in these CZIS NPLs were still broad even though the NPLs exhibited extremely small thickness (1.1 nm) and were considerably monodisperse in the thickness dimension. Having in view a Bohr exciton radius of CIS of 4.1 nm,[96] such thin NPLs should be in quite strong quantum confinement regime, similar to that of CdSe NPLs, as implied by the large PL redshift discussed above. However, the radiative recombination in CIS-based NCs is a more complex process than the band-edge recombination, which occurs through the radiative transition of delocalized conduction band electron to randomly positioned Cu-related emission centers, accommodating holes supplied from the

valence band. The random positioning of these centers over a whole NPL caused by a possible inhomogeneity in the composition within individual NPLs, resulting in the heterogeneity of the ensemble, is the most probable reason of such broad PL bands observed.[141]

The ZnS shell growth through slow addition of Zn(DDTC)$_2$ to the crude solution of CZIS NPLs, as expected, further enhanced the PL intensity due to the capping of the surface defects and thus reducing the number of centers of non-radiative recombination.[20, 36] Here, etching of the NCs, diffusion of Zn into the core via CE are possible processes accompanying ZnS shell growth, which lead to a blue shift of PL maxima. On the other hand, leakage of electron to the shell material and an increase in size due to further growth of NCs during the shell deposition result in a red shift of the PL maxima. In the case of CZIS/ZnS NPLs, a pronounced blue shift both in absorption and PL spectra was not observed, as seen in *Figure 5.22c,d*, since the core NPLs already contained a large amount of zinc inhibiting a further CE reaction. A slight redshift in the PL spectra may be the result of electron delocalization over the entire heterostructure. Thus, core/shell NPLs (synthesized with Cu/(In+Zn) ratio of 0.10) exhibited a PLQY of 29% compared to 9% value of the initial core CZIS NPLs (*Figure 5.22c,d*). While PLQY as high as 80% has been reported for small CIS(Se) NCs with ZnS shell,[111, 145] 2D counterparts with high-intensive PL have rarely been reported. For example, Chen et al. reported the synthesis of non-emitting hexagonal CIS NPLs.[128] Addition of Zn in their case resulted in the degradation of the NPLs to 5 nm small NCs which then exhibited PL.

The average lifetime approximated from the PL decay curves in *Figure 5.22e* was 306 ns for CZIS NPLs with Cu/(In+Zn) ratio of 0.10, while CZIS/ZnS NPLs exhibited an average lifetime of 340 ns. A long decay time along with biexponential[133, 136] or triexponential[49] decay curves are generally observed in the case of I-III-VI-based NCs.[105, 130, 162] The various components correspond to either fast decay attributed to emission transition from surface trap-states, or to slow decay attributed to defect-related donor–acceptor pair transitions.[49] The generally observed long decay time in Cu-deficient CIS-based NCs is attributed to the delay due to the complex recombination mechanism.[130, 136] The decay times of core CZIS NPLs and those of core/shell NPLs were similar, implying that they follow a similar radiative decay channel. However, faster decay in the CZIS NPLs sample and its lower QY indicate that this fast decay pathway is plagued by non-radiative recombination.[115] PL dynamics of single thick-shell CIS/ZnS NCs shows monoexponential decay, while multiexponential PL decay is exhibited by a corresponding ensemble.[141] This further supports the claim that one of the principle reasons of the characteristic optical properties of I-III-VI NCs is still the sample heterogeneity.

Optical properties resulting from the attempts to grow a thicker shell are represented in *Figure 5.23*. With slow addition of $Zn(DDTC)_2$ at 180°C to the solution of purified CZIS NPLs, a significant decrease in the PL intensity was observed after the shell growth (see *Figure 5.23b*). Purification apparently leads to the formation of indium oxide on the NPL surface, which in turn results in the formation of defects on the core/shell interface due to a large lattice mismatch between In_2O_3 and ZnS. Deposition via layer-by-layer addition of S- and Zn-precursors resulted in a ZnS shell, which although was somewhat thicker, did not result in a PL enhancement (*Figure 5.23c*). It implies that the multiple phase transfer reactions taking place at room temperature introduced surface defects in the core and the shell material leading to the degradation of optical properties. Finally, the strategy of the shell growth based on the deposition of In_2S_3 instead of ZnS yielded core/shell NPLs with PLQY of 5%.
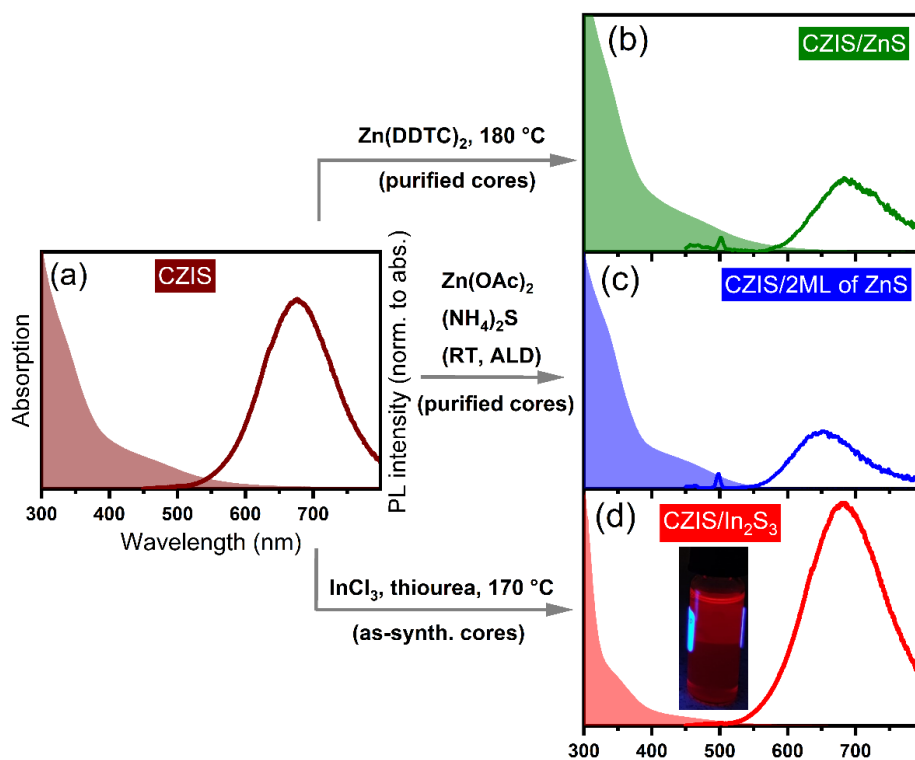
Figure 5.23 *Absorption and PL spectra of as-synthesized CZIS NPLs (using a Cu:In feed ratio of 0.05) (a) and CZIS/ZnS core/shell NPLs synthesized after purifying CZIS core NPLs before the shell growth (b), CZIS/ZnS NPLs synthesized via colloidal ionic layer deposition (c), and CZIS/In_2S_3 core/shell NPLs (d). Inset in (d) shows a photo of a corresponding NPLs dispersion under UV-light.*

5.2.5 Conclusions

Thus, in this work a successful synthesis pathway to obtain rectangular, unstacked CIS, CZIS, and CZIS/ZnS core/shell NPLs with tetragonal crystal phase, exhibiting an inherent PL, was

developed. A synthetic route to obtain CIS NPLs was adopted, wherein the adopted reaction conditions enabled the anisotropic growth of the corresponding CIS seeds leading to the formation of NPLs. The strategy involved the formation of In_2S_3 seeds as the first step, followed by the addition of minimal amount of Cu to form CIS seeds. Thereafter, an increase in temperature led to the anisotropic growth of the CIS seeds to form CIS NPLs with inherent PL in the visible range. Subsequently, an exchange with Zn was carried out to finally produce CZIS NPLs with enhanced PL. The as-synthesized NPLs exhibited a rectangular shape with the thickness of 1.1 nm. Further, it was found that the amount of Cu incorporated plays an important role in the preservation of the NPL shape. As the Cu amount increased more than 10% relative to the In amount, the NPL shape could not be preserved and hence there exists a limit to the maximum amount of Cu that can be incorporated into the NPLs. Additionally, with a variation in the composition of the synthesized NPLs, the PL maxima could be tuned in the range of 650–720 nm with an increase in Cu amount resulting in a red-shift. ZnS shell growth led to a further enhancement of PLQY from 9% in CZIS NPLs to 29 % in CZIS/ZnS NPLs.

5.3 Cu-Zn-In-Se Nanoplatelets with Narrow Photoluminescence in the Near Infrared Range

This Section is based on the manuscript 'Cu-Zn-In-Se Nanoplatelets with Narrow Near Infrared Photoluminescence'. In preparation.

5.3.1 Background and Aim

The previous chapter discussed a synthetic strategy for CZIS NPLs which exhibited inherent PL in the visible range. Moving to longer wavelengths, tuneable optical properties in the NIR window of 1300–1600 nm are of particular interest in telecommunications, while biological window of 800–1100 nm makes NIR emitting NCs in this range best fit for bio-imaging, and the NIR window of 800–2000 nm is important in photovoltaics.[47] Due to extremely narrow bulk band gap and high optical efficiencies of lead and mercury chalcogenide NCs, they have been proven as suitable candidates for a wide range of NIR-based applications.[47, 48, 181-183] However the presence of toxic elements poses a major setback in their widespread use, particularly in those applications involving exposure to biological environments. This has led to the development of synthetic strategies of I-III-VI-based semiconductor NCs as a less toxic earth-abundant metal containing alternative with the potential as NIR emitters, making them a suitable replacement as fluorophores in various applications.[21, 181] In this group, CISe-based NCs with a narrow bulk band gap of 1.04 eV and large exciton Bohr radius of 10 nm are an

interesting and less studied material.[21] While reports of NIR-emitting CISe NCs are abundant, their PL range is limited to 1100–1200 nm and pushing it to even longer wavelengths would unlock a plethora of new applications.[35, 145, 150, 163, 184, 185] CISe-based QDs with tuneable emission in the range of 990–1060 nm were accomplished in this work, as discussed in *Section 5.1*. However, 2D morphologies of this group that exhibit PL are not yet reported in literature. With the emerging applications of 2D materials and unique optical properties exhibited by 2D materials of II-VI group, it is reasonable to explore these morphologies in the case of CISe-based NCs as well.

The aim of this work was to synthesize quaternary CZISe NPLs that exhibit PL in the NIR range. With this aim, the synthetic approach presented in the previous section for CZIS NPLs was optimized to compensate for the reactivity differences of S- and Se-precursors. Starting with the replacement of S with Se in the previous synthetic pathway proved that the same reaction parameters were not favorable for the Se counterpart. Consequently, In_2Se_3 seeds were synthesized first with a modified reaction temperature, followed by the formation of CISe seeds via the addition of a small amount of Cu^+ at room temperature. Thereafter, anisotropic growth of these seeds was promoted by an increase in temperature leading to the formation of CISe NPLs. To enhance the PL intensity and to improve the stability of these NPLs, Zn was incorporated in the subsequent partial CE step. To establish the tuneability of the PL maxima, variation of different parameters, like composition of NPLs and temperature of the synthesis, was carried out. Thus, this section describes a synthetic method that enables the realization of 2D morphologies of photoluminescent CISe-based NCs.

5.3.2   Synthesis and optical properties of CZISeS and CZISe NCs

The procedure adopted in *Section 5.2* for the synthesis of CZIS NPLs was modified to synthesize CZISeS NPLs by adding a Se-precursor in the above mentioned reaction procedure with the final aim of completely replacing S with Se, leading to the formation of CZISe NPLs with emission pushed into the NIR range. First, 50% of Se was added along with 50% of S in the reaction mixture and the reaction conditions were kept same as in the synthesis of CZIS NPLs. In this case, as seen in the TEM image in *Figure 5.24a*, the NPL shape was maintained. Consequently, addition of 75% of Se along with 25% of S, and further complete replacement of S, i.e., addition of 100% of Se were carried out, which resulted in the dissolution of the NPLs into small-sized QDs (*Figure 5.24b-c*). These experiments revealed that the reaction temperature of 100°C used for the seed formation and 180°C used for promoting the anisotropic growth were not suitable for growing 2D CZISe NCs.
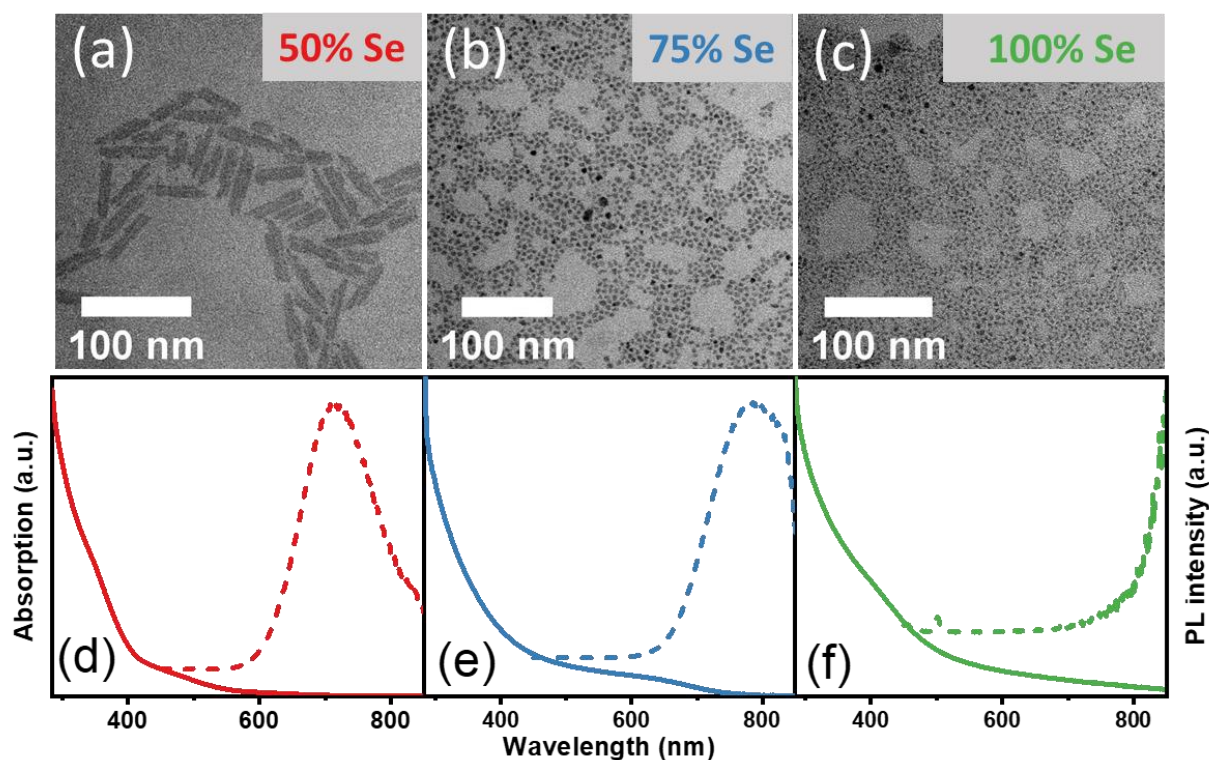
Figure 5.24 *TEM images of CZISeS NCs synthesized with 50% Se (a), 70% Se (b), and CZISe NCs with 100% Se (c). Absorption and PL spectra of CZISeS NCs synthesized with 50% Se (d), 75% Se (e), and CZISe NCs with 100% Se (f).*

The optical properties of the synthesized CZISeS and CZISe NCs are depicted in *Figure 5.24d-f* which shows that with an increase in Se amount a red shift of PL maxima occurred, and the PL of CZISe NCs with 100% Se was shifted to the NIR range. However, shifting the emission in the NIR while maintaining the 2D morphology was a challenge. Thus, the anisotropic growth of the CISe seeds while resulting in emission in the NIR range, required significant optimization of reaction parameters owing to the differences in reactivities of S and Se. This required revisiting the In_2S_3 NPL synthesis and modifying the reaction conditions for In_2Se_3 NPLs. These reaction conditions could then be adopted for the synthesis of CZISe NPLs to maintain the 2D morphology.

5.3.3 Synthesis of In_2Se_3 NSs

In_2Se_3 NSs were synthesized using a modified procedure reported by Park et al. for In_2S_3 NSs (see *Figure 5.25*).[144]
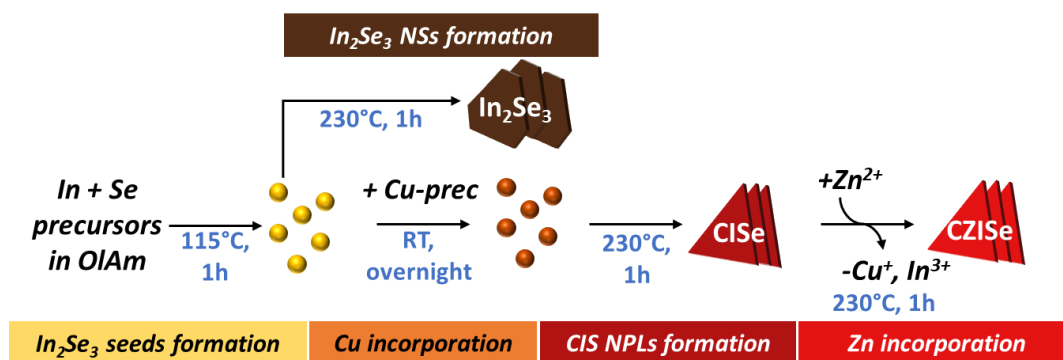
Figure 5.25 Scheme of the synthesis of In$_2$Se$_3$ NSs and CZISe NPLs.

Using 1 equivalent of In and 1.5 equivalents of Se, as was reported by Park et al. in their typical synthesis, the reaction temperature was modified to compensate for the difference in reactivity of the S- and Se-precursors. It has been observed that syntheses with Se precursors typically require higher temperatures and longer reaction times, as compared to syntheses with S-precursors.[95] Therefore, the temperature of the In$_2$Se$_3$ seeds formation was raised to 115°C and the temperature of subsequent step of NPL formation was raised to 230°C. The TEM image of the resultant NPLs depicted in *Figure 5.26* shows the formation of 2D stacked large NCs.
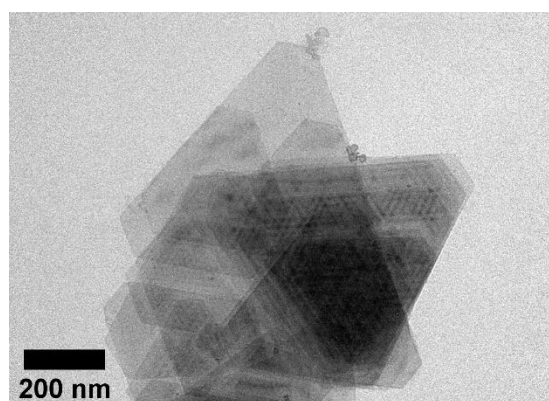
Figure 5.26 TEM image of In$_2$Se$_3$ NSs.

In$_2$Se$_3$ is a polymorphic material, which exists in many crystal phases with three most common ones – α, β and γ phases. In ambient conditions, crystallization in the layered phases of α and β is favoured.[186-188] Hexagonal In$_2$Se$_3$ NSs, crystallizing in β phase synthesized using a selenourea precursor and short aminonitriles as shape controlling agents, were reported by Almeida et al.[169] Additionally, synthesis of low dimensional In$_2$Se$_3$ in different phases and their corresponding applications are discussed in detail in the review by Li et al.[188] The position and intensity of reflexes of α crystal phase of bulk In$_2$Se$_3$ (JCPDS-ICDD- C20-493) depicted in the *Figure 5.31* suggest that the In$_2$Se$_3$ NSs synthesized here crystallize in α phase with the position of reflexes shifted to lower 2 theta values. The successful synthesis of In$_2$Se$_3$ NSs paved the

way to the synthesis of CISe and CZISe NPLs by using the same In_2Se_3 seeds and the modified reaction temperature.

5.3.4 Synthesis of CISe and CZISe NPLs

The synthesis of CZISe NPLs was developed with optimized reaction parameters adopted for the synthesis of In_2Se_3 NPLs. Generally higher temperature and long reaction time are favored for the synthesis of CISe-based NCs as compared to CIS-based NCs to compensate for the difference in reactivity of S- and Se-precursors.[95] Additionally, different reactive Se-precursors, e.g., trimethylsilyl selenide and dodecaneselenol[35, 127] have also been used to synthesize CISe NCs. In this approach, CISe NPLs were grown from CISe seeds under a higher temperature followed by the incorporation of Zn to result in quaternary CZISe NPLs. The first step involved the formation of In_2Se_3 seeds by reaction of $InCl_3$ and Se powder dissolved in OlAm at 115°C for 1 h. OlAm acts a solvent and the sole ligand for the NCs which also helps in breaking the symmetry and promotes the 2D growth of NCs, wherein the preferential attachment of the amine on the facets of the NCs prevents the growth of the NPLs in the thickness direction.[116]

The In_2Se_3 seeds were formed with varying amounts of In to result in varying final compositions of CZISe NPLs. In-rich and near stoichiometric In:Se ratios were used for the synthesis of In_2Se_3 seeds. The formation of In_2Se_3 seeds was followed by the addition of 200 µL of 0.075 M $[Cu(CH_3CN)_4]PF_6$ solution in acetonitrile to incorporate Cu^+ in the In_2Se_3 leading to the formation of CIS seeds. The addition of Cu was accompanied by a colour change from bright yellow to brown, indicating the immediate transformation of In_2Se_3 seeds to CIS seeds. The reaction mixture was kept under stirring overnight to incorporate as much Cu^+ as possible into the In_2Se_3 seeds. In the subsequent step, the temperature was raised to 230°C promoting the growth of the NPLs via attachment of the seeds followed by anisotropic growth. It has been established that the presence of DDT is a crucial step in the synthesis of CISe NCs, since DDT being a reducing agent prevents the oxidation of Cu^+ thus enhancing stability of the NCs synthesized.[21] Therefore, 1 mL of DDT was added at room temperature and the NPLs were kept under stirring. In the final step, Zn was incorporated into the CISe NPLs via a partial CE, forming alloyed quaternary CZISe NPLs.

As seen in the TEM image of CISe NPLs depicted in *Figure 5.27a*, the incorporation of Cu leads to a significant change in the morphology of the NPLs. As compared to the large In_2Se_3 NSs, the CISe NPLs grew smaller and adopted triangular shape. They formed stacks made of several resulting in nanostructures, in which the building blocks were single crystal

NPLs, as revealed from the HRTEM images of CISe NPLs shown in *Figure 5.28a*. This stacked nature of the NPLs can be attributed to the use of a single ligand, which leads to an ordered ligand arrangement resulting in lower solubility of the particles, as compared to a disordered ligand arrangement adopted in the case of a mixture of ligands.[171] The TEM image depicted a polydisperse shape and size distribution and it was difficult to estimate the size of the individual NPLs due to the stacked appearance on the TEM image.
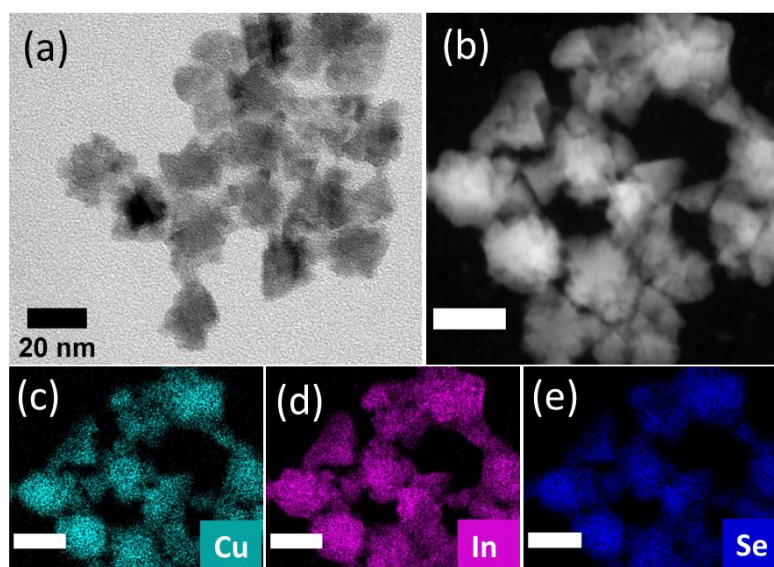
Figure 5.27 *Conventional TEM image (a), HAADF-STEM (b) and corresponding EDXS-based element maps of Cu (c), In (d), and Se (e) of CISe NPLs synthesized at 230°C. All scale bars are 20 nm.*

The thickness of the single NPLs was estimated to be 2 nm from the HRTEM image of vertically oriented stacks of CISe NPLs as shown in *Figure 5.28b*. The HAADF-STEM image shown in *Figure 5.27b* (which mainly depicts atomic-number contrast) further confirmed that the main building blocks of the NCs are triangularly shaped single platelets. Additionally, a few hexagons were observed as well. EDXS element maps (*Figure 5.27c-e*) revealed that the Cu and Se distributions coincide very well, while the In distribution varies, especially at the particle edges.
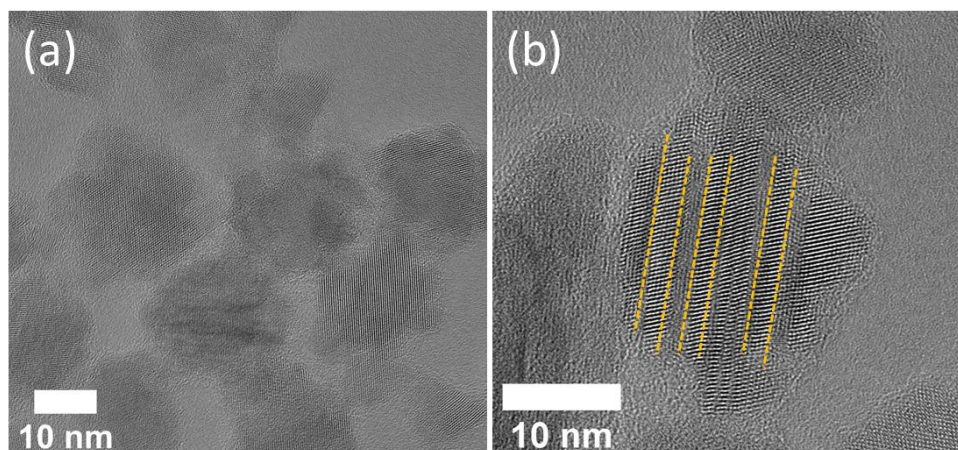
Figure 5.28 *HRTEM image of CISe NPLs (a) and vertically oriented stacks of CISe NPLs*
(b).

To gain more insights into the growth mechanism of the CISe NPLs, the progress of the synthesis was monitored by TEM imaging of samples of the reaction mixture taken when the reaction temperature reached 150°C, 180°C, and 213°C (*Figure 5.29a-c*). From the TEM images it was observed that at these temperatures the NPL formation was not initiated, but the attachment of seeds observed at 150°C became pronounced as the temperature increased. Upon reaching 230°C, the temperature was maintained for 1 h and samples of the reaction mixture were collected at 0 min, 5 min, 10 min, and 20 min for TEM imaging (*Figure 5.29d-g*). According to these TEM images, the CISe NPLs were formed at 230°C, with the attachment of CISe seeds followed by anisotropic growth. The NPL formation mechanism is similar to that proposed by Zhong et al., wherein small CISe nanoparticles were formed at the start of the reaction, and after monomer consumption these nanoparticles dissolved to release monomers which formed the NPLs, a process very similar to the Ostwald ripening.[104] In our case, the CISe seeds attached to form small NCs, which then underwent 2D growth to form triangular NPLs that stacked on each other.
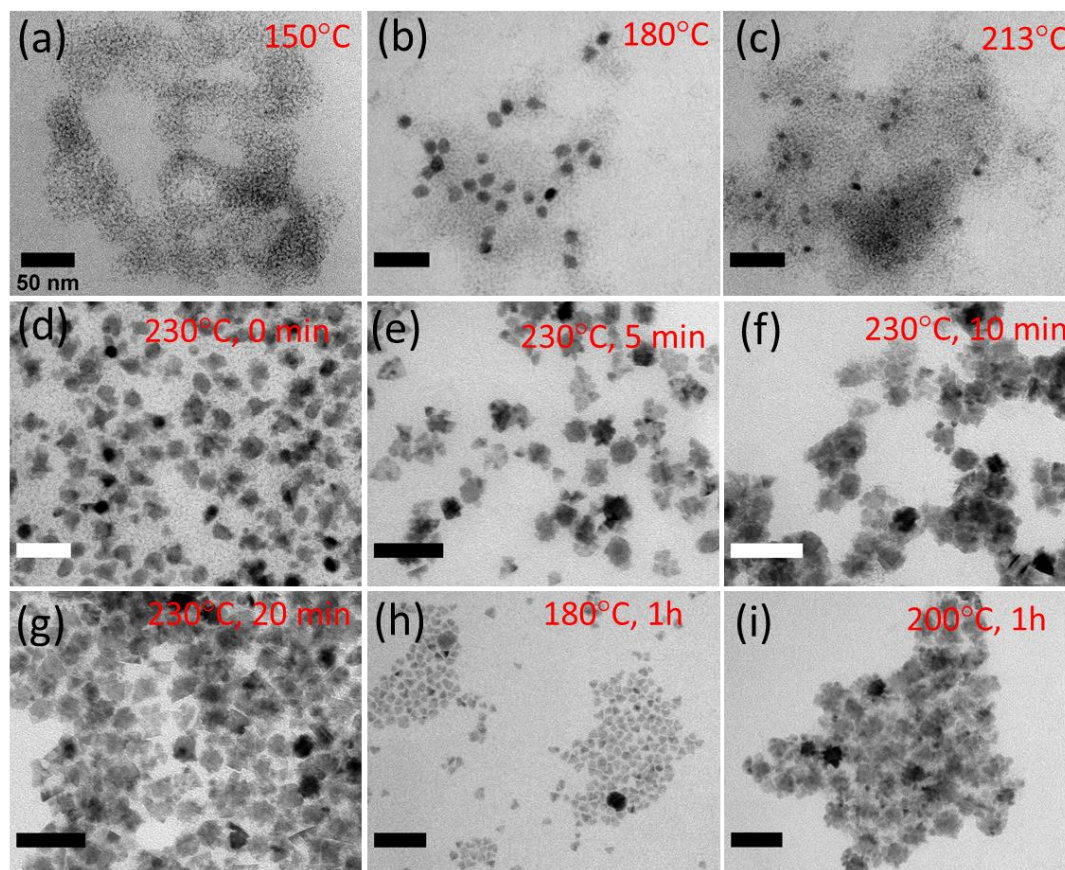
Figure 5.29 *Conventional TEM images of samples from the CISe NPLs synthesis taken when the temperature reached 150°C (a), 180°C (b), 213°C (c), and 230°C (d); 230°C after 5 min (e), 230°C after 10 min (f), and 230°C after 20 min (g). The samples synthesized at 180°C (h) and 200 °C (i). All scale bars are 50 nm.*

The impact of temperature on the formation of CISe NPLs was further studied by employing lower temperatures for the NPL growth. When the synthesis was carried out at 180°C for 1 h, the NPLs were not formed and rather small 0D NCs were observed (*Figure 5.29h*). Subsequently, synthesis at 200°C led to the agglomeration of smaller particles but did not result in well-defined shapes (*Figure 5.29i*). Only at 230°C the NPLs adopt a defined triangular shape, stacking on each other leading to the appearance of irregular shapes (See *Figure 5.27a*). It was observed from ICP-OES results summarized in *Table 5.3* that different temperatures lead to incorporation of different amounts of Cu^+ in the In_2Se_3 seeds, resulting in different compositions (Cu:In:Se) from the same Cu:In:Se feed ratio of 1:20:13. This difference in composition of the resultant particles might be the plausible reason for the difference in morphology.

Table 5.3 *Feed ratio and element ratio (Cu:In:Se) as obtained from ICP-OES of CISe NPLs synthesized at different temperatures.*

Temperature (°C)	Cu:In:Se feed ratio	Cu:In:Se final composition
180	1:20:13	1:1.11:1.02
200		1:1.06:2.10
230		1:2.07:3.70

In the next experiment the time for the formation of CISe seeds, i.e., time for Cu incorporation, was reduced from the overnight process to solely 1 h. TEM image in *Figure 5.30a* reveals that this led to the formation of smaller aggregated NCs with tetrahedral shape. Furthermore, the amount of ligands used was varied to study its effect on the morphology. Instead of 9 mL of OlAm used in general for the synthesis, 4.5 mL OlAm was added, also resulting in the formation of small tetrahedral NCs (*Figure 5.30b*). Lastly, the stacked arrangement of NPLs was attempted to be altered by using a mixture of ligands, i.e., by adding a short ligand (dodecylamine) along with the longer-chain OlAm. However, this led to complete distortion of the 2D morphology yielding only small NCs, as shown in *Figure 5.30c*. Therefore, it can be concluded that the synthetic conditions adopted for the CZISe NPLs were quite crucial for achieving anisotropic shape, where the variation of certain reaction parameters rather led to different morphologies.
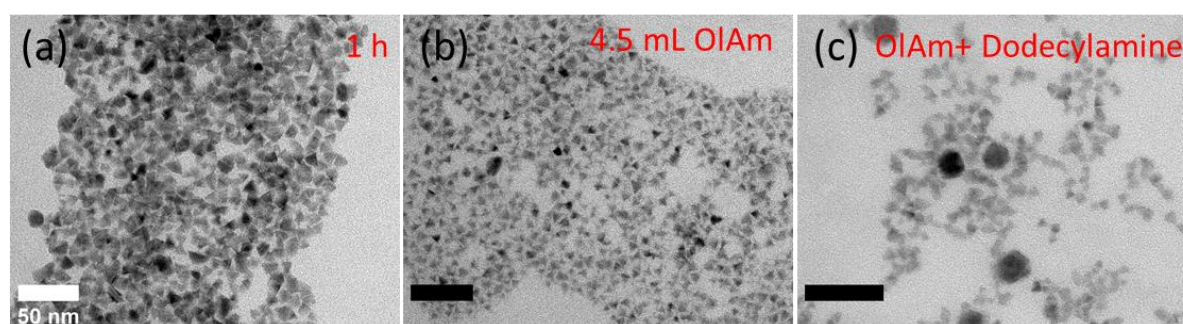
Figure 5.30 *Conventional TEM images of samples from the CISe NPLs synthesis using: 1 h for Cu⁺ incorporation (a), 4.5 mL of OlAm (instead of 9 mL) (b), a mixture of OlAm and dodecylamine (c). All scale bars are 50 nm.*

CISe generally exists in two crystalline phases, tetragonal phase which is the low temperature phase and cubic phase which is the high temperature phase.[104] CISe NPLs in the low temperature tetragonal phase were reported by Tang et al.,[65] Zhong et al.,[104] and Bi et al.[100].

However, hexagonal ultrathin CISe NPLs obtained from tetragonal ungamite CuSe NPLs via CE were also reported for the first time by Berends et al.[127] The synthesized CISe NPLs in this work adopted a tetragonal phase, as was confirmed by the XRD pattern shown in *Figure 5.31*. The positions of the reflexes match well with bulk tetragonal CISe reference (JCPDS- ICDD-C35-1349). The three pronounced reflections at 27°, 45°, and 53° correspond to the planes (112), (204), and (116), respectively, lying in the lateral directions. The lattice parameters calculated from the XRD patterns are as follows: a = b = 0.577 nm, c = 1.158 nm, which are in good agreement with reported data a = b= 0.578 nm, c = 1.161 nm[104]. The crystallite size, as calculated by the Scherrer equation was 8.3 nm. Noteworthy that the addition of Cu triggers the crystallization of the CISe NPLs in a different crystal structure from that of the pure In_2Se_3 NSs. This difference in crystal structure might be the plausible reason for distinct morphologies of In_2Se_3 NPLs and CISe NPLs.
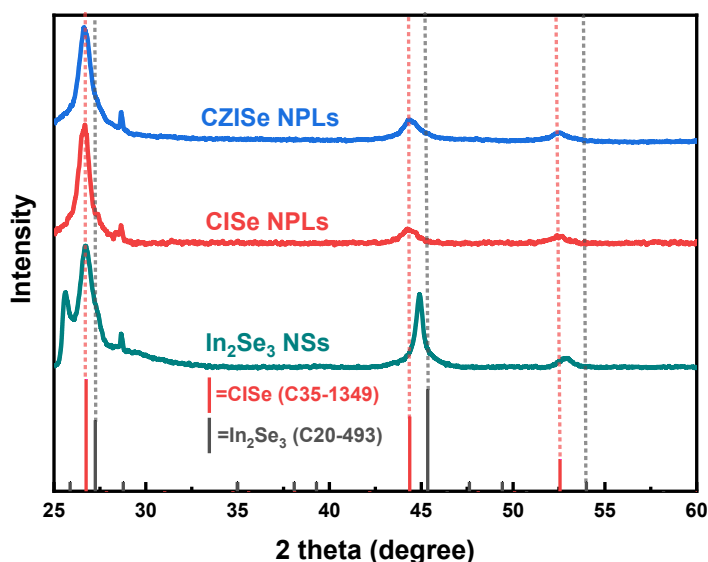
Figure 5.31 *XRD patterns of In_2Se_3 NSs, CISe and CZISe NPLs with corresponding bulk reference structures of CISe (C35-1349) and In_2Se_3 (C20-493) from the JCPDS-ICDD.*

In the final step of the synthesis, CISe NPLs were treated with the Zn-precursor. The addition of Zn made the shape of NPLs more defined with shaper edges, as seen in the TEM images in *Figure 5.32a-d*. However, incorporation of Zn did not lead to further unstacking of the individual platelets. The sizes of the individual NPLs were difficult to calculate precisely due to the formation of stacks which were estimated to be approx. 18 nm. HAADF-STEM image of CZISe NPLs in *Figure 5.32e* further confirmed their triangular shape. EDXS element maps indicated the presence of Cu, In, and Se, whose distribution can be considered

homogenous (*Figure 5.32f-i*). The distribution of Zn, at the same time, was rather inhomogeneous with its location mainly on the particle surface, because of surface-limited CE.
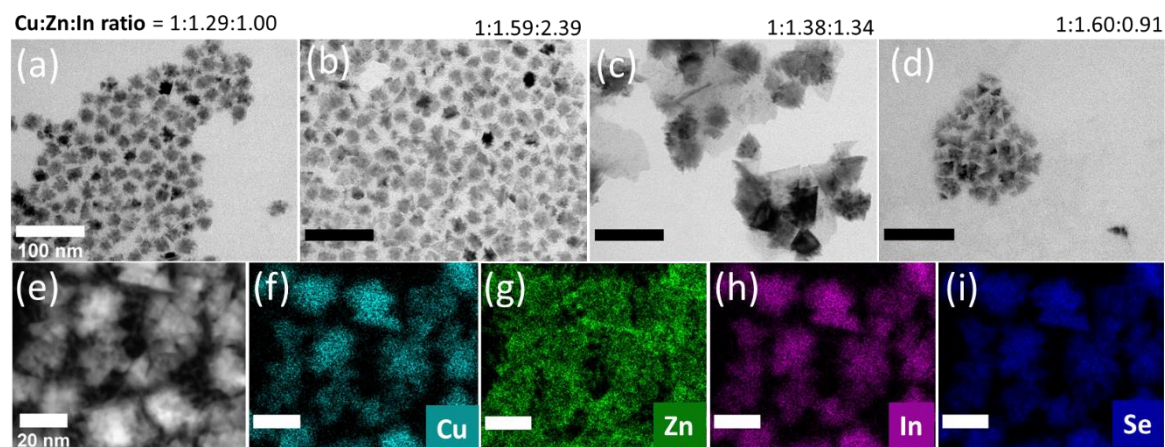
Figure 5.32 *TEM image of CZISe NPLs with Cu:In ratio of 0.794 (a), 0.628 (b), 0.72 (c), and 0.623 (d). HAADF-STEM image (e) and corresponding EDXS-based element maps of Cu (f), Zn (g), In (h), and Se (i) of CZISe NPLs. All scale bars from (a-d) are 100 nm and (e-i) are 20 nm.*

Table 5.4 *ICP-OES results for CZISe NPLs with varying feed amounts of In.*

Cu:In feed ratio	Cu:In final ratio	Cu:In:Zn	In:Zn
0.0375	0.79	1:1.29:1.00	1.28
0.05	0.63	1:1.59:2.39	0.66
0.1	0.72	1:1.38:1.34	1.03
0.115	0.62	1:1.60:0.91	1.10

The effect of difference in composition on NPL morphology and optical properties was further studied by keeping the Cu, Se, and Zn precursors' amounts fixed at 0.015 mmol, 0.2 mmol, and 3 mmol, respectively, while varying the In amount. To this end, 0.4 mmol, 0.3 mmol, 0.15 mmol, and 0.13 mmol of In were employed thereby resulting in Cu:In feed ratios of 0.0375, 0.05, 0.1, and 0.115. The final ratios of Cu:In, Cu:In:Zn, and In:Zn in CZISe NPLs, as obtained from the results of ICP-OES analysis, are presented in *Table 5.4*. From the ICP-OES results it was observed that the lowest Cu:In feed ratio of 0.0375 led to the highest Cu:In ratio of 0.794 in the NCs, while a decrease in the In amount from Cu:In feed ratios of 0.05 through 0.1 to 0.115 consequently led to lower Cu:In ratios of 0.628, 0.72, and 0.623, respectively. It is therefore evident that the final Cu:In ratios did not follow a particular trend, while it can be concluded that in all cases the final Cu:In ratios were in the narrow range of

0.6–0.7. This rather constant composition is most probably due to the fact the entire reaction takes place in the same pot, wherein both Cu and Zn addition was carried out without intermediate purification steps. This leads to competition between all cations involved thereby resulting in different compositions of the CZISe NPLs. The final ratio of the three cations and the respective In:Zn ratio obtained for the different compositions are summarized in *Table 5.4*. The Cu:Se ratio in all compositions (> 0.20) was always much higher than the feed ratio (0.075), which proves the high affinity between Cu(I) and Se and justifies the choice of a low Cu feed amount in the synthesis. Furthermore, a large excess of the Zn-precursor is also necessary for the efficient incorporation of Zn^{2+} (feed ratio of Zn:Se of 10 resulted in final Zn:Se ratio of 0.2–0.5).

The XRD pattern of CZISe NPLs depicted in *Figure 5.31* indicates that the incorporation of Zn did not trigger any change in the crystal structure and the tetragonal crystal structure was preserved, which is generally observed in the case of CE reactions. A slight shift of Bragg reflections to larger angles was observed after the incorporation of Zn, which can be explained by the smaller lattice constant of zinc-blende ZnSe (5.67 Å) compared to chalcopyrite $CuInSe_2$ (5.78 Å).

5.3.5 Optical properties of CISe and CZISe NPLs

The progress of the reaction from the formation of In_2Se_3 seeds to the final CZISe NPLs was monitored by collecting absorption spectra. As seen in *Figure 5.33a*, In_2Se_3 seeds exhibit a featureless absorption with the onset at approx. 400 nm and a small shoulder at approx. 300 nm. In_2Se_3 NSs synthesized from the In_2Se_3 seeds also exhibited a featureless absorption. The incorporation of Cu^+ leading to the formation of CIS seeds triggers a slight redshift of the absorption onset. The formation of CISe NPLs further accentuates the red shift due to the growth of NCs, resulting in the absorption onset at approx. 1000 nm (see *Figure 5.33b*). For all Cu:In feed ratios, i.e., 0.035, 0.05, 0.1, and 0.115, the onset of absorption lies in this range, whereas starting from 500–550 nm the absorption increases towards shorter wavelength. Finally, after adding Zn^{2+} the absorption spectra undergo no significant changes in shape, remaining mainly featureless, with the onset and the short wavelengths absorption region shifting to shorter wavelengths for all compositions of CZISe NPLs (*Figure 5.33c*). The shape of the spectra represented the commonly observed featureless absorption for CIS(Se)-based NCs.
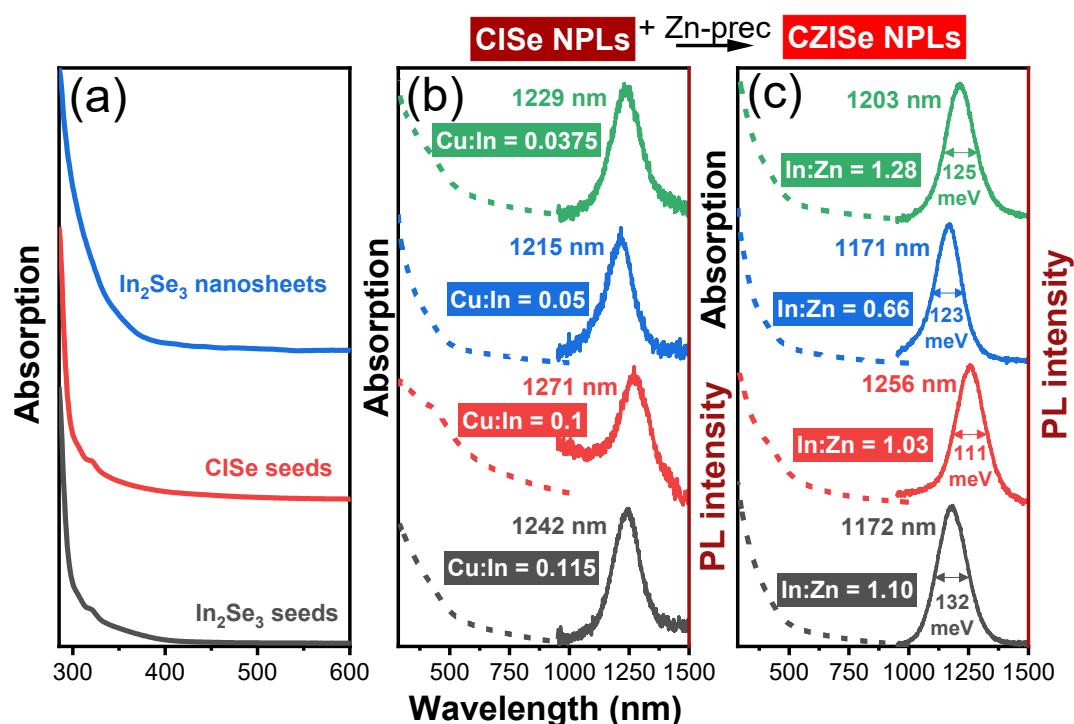
Figure 5.33 *Absorption spectra of In_2Se_3 seeds, CIS seeds, and In_2Se_3 NPLs (a), absorption and PL spectra of CISe NPLs (b) and CZISe NPLs (c) with different compositions.*

Steady state PL spectra of the CISe NPLs were acquired for different compositions and we found that all of them were emitting without the incorporation of Zn, as shown in *Figure 5.33b*. However, the PL intensities were quite low. PL spectra of the CISe NPLs were tuneable in a narrow wavelength range: CISe NPLs with Cu:In feed ratios of 0.035, 0.05, 0.1, and 0.115 exhibited PL maxima at 1229 nm, 1215 nm, 1272 nm, and 1242 nm, respectively. The most red shifted emission was observed for Cu:In ratio of 0.1, while a decrease in the Cu:In feed ratio to 0.05 and 0.035 led to a blue shift of the PL maxima. We can conclude that the position of PL maxima does not change drastically upon changing the Cu:In feed ratio. Increasing the Cu amount to shift the PL instead led to deterioration of the PL intensity.

We monitored the growth of the CISe NPLs over time with PL spectroscopy. PL spectra were recorded for the samples taken at 0, 5, 10, 20, and 60 min during the growth of NPLs at 230°C and from *Figure 5.34a* it is clear that the maximum intensity was attained after 60 min of the growth. Decreasing the time of Cu incorporation to 1 h led to the blue shift of the PL maximum along with the decrease in PL intensity, as depicted in *Figure 5.34b*. Use of a mixture of ligands to unstack the NPLs also caused a blue shift of PL accompanied by a considerable degradation of its intensity, as seen in *Figure 5.34c*. Interestingly, decreased amount of OlAm in the synthesis led to an increase of PL intensity accompanied by a large blue shift (see *Figure*

5.34d). The blue shift of PL maxima in these cases can be attributed to the decreased size of the NCs with different morphologies.
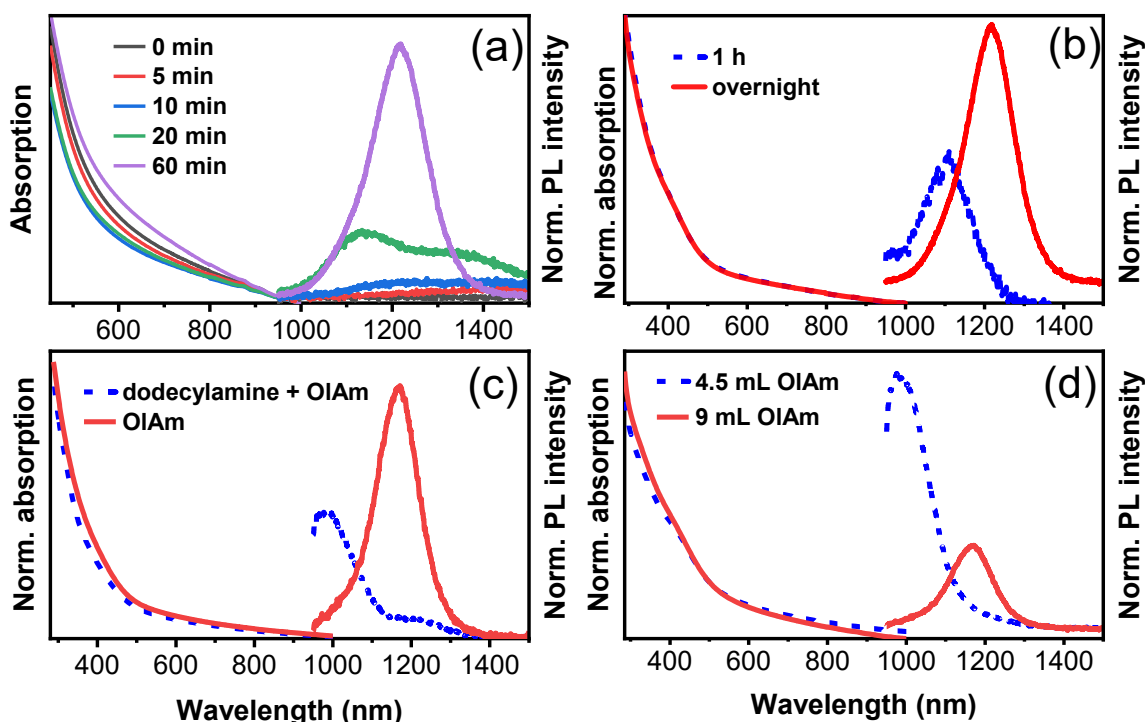
Figure 5.34 *Absorption and PL spectra of samples of CISe NPLs taken at 0, 5, 1, 20, and 60 min of the synthesis (a); CISe NPLs synthesized the Cu incorporation for 1 h and overnight (b), CISe NPLs synthesized with a mixture of ligands and a single ligand (c), CISe NPLs synthesized with 4.5 mL and 9 m L of OlAm (d).*

The addition of Zn led to a slight blue shift of the PL maxima along with the enhancement of the PL intensity. This shift is generally attributed to the enlarged band gap upon incorporation of Zn and a relatively higher PL intensity than that of the CISe NPLs is a result of the healing of crystallite defects, especially those on the surface via the formation of a ZnSe-rich shell.[101] As observed from *Figure 5.33c*, for CZISe NPLs with In:Zn ratio of 1.28 the PL maximum is located at 1203 nm. A decrease in the In:Zn ratio to 0.66 and 1.098 led to a blue shift of PL maxima to 1170 nm. However, the In:Zn ratio of 1.028 led to the maximal red shift with the PL peak reaching 1256 nm. It can be concluded that the change in composition does not lead to a significant variation of the PL peak position, which is tuneable in a narrow wavelength range of 1170–1256 nm. Previously reported in literature, 3–5 nm CISe QDs emit between 600 and 800 nm with broad PL band widths of approx. 250 meV.[146, 189] For approx. 6 nm sized CISe Lox et al. reported PL maximum at 990 nm with PL band width of 160 meV.[21] Approx. 5 nm-sized CZISe NCs discussed in *Section 5.1* also exhibit PL in the range of 980–

1060 nm. Considering that the thicknesses of the CZISe NPLs are reasonably small, i.e., approx. 2 nm, the observed positions of PL maxima are dramatically red shifted. A similar red shift in the case of 1D confinement was observed for the CZIS NPLs described in *Section 5.2*.

Interestingly, these CZISe NPLs exhibited quite narrow band widths contrary to usually broad PL spectra inherent to this class of materials, which generally have FWHM on the order of 300 meV.[141] FWHM values determined for CZISe NPLs were 125 meV, 123 meV, 111 meV, and 132 meV for Cu:In feed ratios of 0.035, 0.05, 0.1, and 0.115, respectively. FWHM values for the CZISe NCs discussed in *Section 5.1* were already lowered to the range of 150–190 meV and in the case of the CZISe NPLs these values were further lowered. With thickness of approx. 2 nm of single CZISe NPLs, much smaller than the exciton Bohr radius of CISe of 10.6 nm, the resultant confinement in this direction is expected to be quite strong, which might be the probable reason for this narrow PL band width. However, when compared to the FWHM values of other anisotropic 2D materials, the PL band widths are still broad. Among the narrowest emitters are CdSe NPLs with FWHM values as low as 20 meV.[25, 190] In the NIR region, PL band widths as narrow as 80 meV have been reported for PbSe NPLs.[121] Nevertheless, the PL band widths obtained for the CZISe NPLs are significantly narrower than that obtained for CZIS NPLs in *Section 5.2,* and are by far the narrowest in this class of materials.

Several reports on CISe-based QDs, especially with an additional growth of a shell that exhibits high PLQY, are present in the literature. For example, Yarema et al. reported the synthesis of CISe/ZnSe NCs reaching 60% PLQY.[145] CISe/ZnS NCs with 50% and 60% PLQY have been reported by Casette et al.[51] and Park et al.,[191] respectively. However, anisotropic Cu-chalcogenide NCs that exhibit PL are rare, with very few reports for CIS-based 2D NCs and none for CISe-based NCs. The NPLs synthesized in this work achieved PLQY of 9% for In:Zn ratio of 0.66. Thus, this is the first report of CISe-based 2D NCs that exhibit PL shifted to the NIR range farther than the reported materials. TRPL characterization of these NPLs revealed an average lifetime of 475 ns, as displayed in *Figure 5.35*. Such long lifetime on the order of hundreds of ns is in accordance with literature data and confirms the complex mechanism of radiative recombination present also in this material.[139, 140]
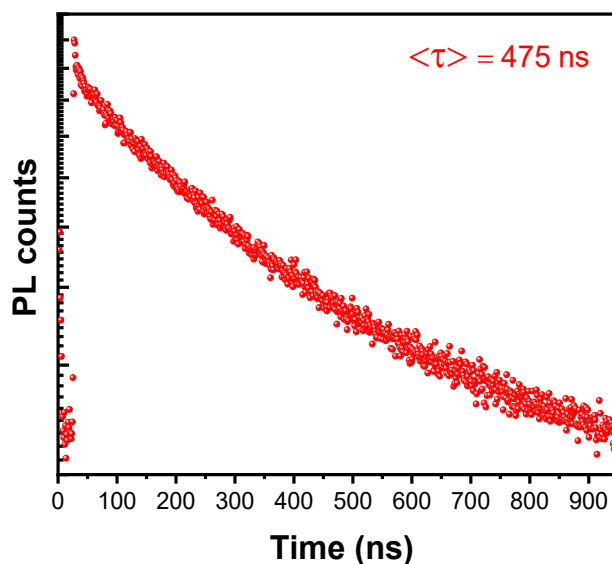
Figure 5.35 *PL lifetime trace of CZISe NPLs.*

5.3.6 Conclusions

In this work, CISe and CZISe NPLs were synthesized by a seed-mediated approach. The NPLs form stacks containing several single particles overlaid on top of each other, and their 2D morphology was proven by the HRTEM and HAADF-STEM imaging revealing triangular platelets with thickness of approx. 2 nm. Both CISe and CZISe NPLs synthesized adopted a tetragonal structure. The CISe NPLs exhibited weak PL in the NIR range, while the incorporation of Zn led to a significant enhancement of their PL intensity achieving 9% QY with PL maxima ranging from 1170 to 1250 nm. Previous reports on the synthesis of CISe based 2D NCs did not show any emission. Thus, to the best of our knowledge this is the first report of CISe-based 2D NCs with inherent PL. Furthermore, significantly narrow PL bands were observed for the synthesized CZISe NPLs with FWHM values lowered to the range of 110–130 meV, which are among the narrowest reported so far for this class of materials.

6   Summary and Outlook

In this work, strategies to synthesize I-III-VI NCs, exhibiting tunable PL in a broad spectral range, were developed. Among them, CZISe NCs were synthesized using a CE approach with $Cu_{2-x}Se$ serving as starting template NCs. This synthetic route, wherein the guest cations, i.e., Zn and In, were injected simultaneously into the $Cu_{2-x}Se$ NCs, yielded alloyed CZISe NCs with a Zn-rich surface that exhibited a high PLQY of 20% without an additional shell growth, which is usually required to enhance PL in CISe-based NCs. The integrity of the starting $Cu_{2-x}Se$ NCs in terms of their shape and crystal structure was preserved after this exchange reaction, which is one of the advantages of this synthetic approach. Composition tuneability enabled the variation of the PL maxima in the wavelength range of 980–1060 nm. The FWHM of the PL bands was lowered significantly to 150–190 meV, contrary to broad PL widths of 300 meV generally exhibited by this class of material. This can be attributed to the substantial elimination of the inhomogeneities in the NC ensemble using the simultaneous CE strategy.

Along with 0D morphologies, the urge to further explore other shapes with 1D confinement led to the development of a synthetic route to CZIS NPLs. Consequently, a seed-mediated approach starting with In_2S_3 seeds followed by the formation of CIS seeds and thereafter anisotropic growth of the seeds to result in ternary CIS NPLs was developed. In this approach, a partial CE step was also involved for the incorporation of Zn, leading to the synthesis of quaternary CZIS NPLs. This offered better shape control over the synthesis resulting in unstacked NPLs. The synthesized CZIS NPLs exhibited tunable PL in the range of 650–720 nm, depending on the amount of Cu incorporated. An additional shell growth on the synthesized NPLs enabled the enhancement of PLQY up to 29% in CZIS/ZnS NPLs from 9% in CZIS NPLs. Such high-quality uniform NPLs with high PLQY have not yet been reported.

Finally, to cater to the applications requiring NIR emission, the synthesis of CISe-based NPLs was explored. Due to the differences in the reactivities of S- and Se-precursors optimization of the reaction parameters was essential for the synthesis. Similar to CIS NPLs, CISe NPLs were synthesized starting with In_2Se_3 seeds followed by Cu incorporation, yielding CIS seeds. Anisotropic growth of the CIS seeds was promoted to result in CISe NPLs, which was followed by a partial CE with Zn to form quaternary CZISe NPLs. The adopted strategy for the synthesis of 2D CZISe NCs resulted in stacked triangular NPLs made of several single platelets, which exhibited exceptionally narrow PL bands, lowered to the range of 110–130 meV. Even though a polydisperse size distribution in terms of lateral dimensions was observed,

the narrow PL band widths indicated strong 1D confinement in the thickness direction. The synthesized NPLs were emissive in the range of 1170–1256 nm and achieved a PLQY of 9%.

Thus, in this thesis several important challenges related to the synthesis of Cu-chalcogenide-based NCs were addressed. Challenges of poor size and shape control leading to broad PL bands and low PL intensity in 0D QDs were solved by using a simultaneous CE approach. Significant advances in the field of 2D NCs of I-III-VI group of semiconductors were also achieved, wherein the routes to emitting Cu-chalcogenide-based 2D materials were developed. The morphologically vivid NCs synthesized, and their respective properties are summarized in *Figure 6.1*.
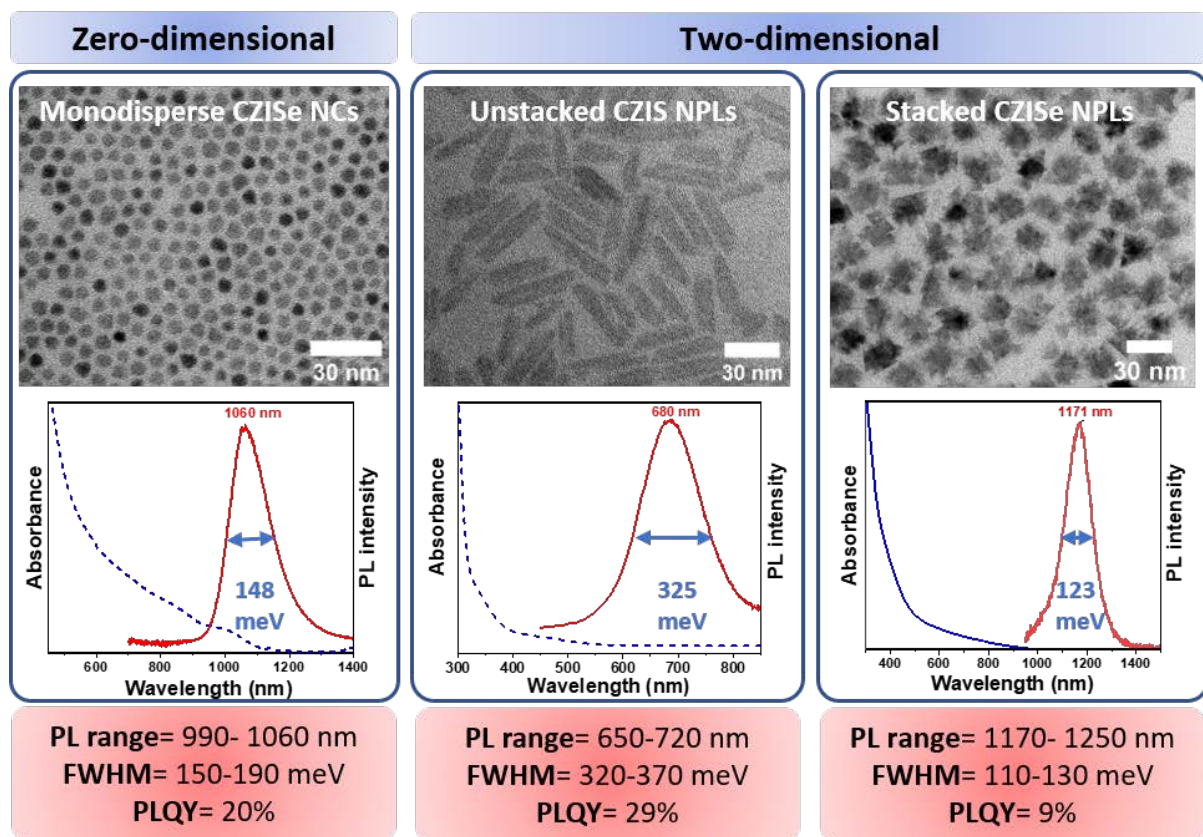
Figure 6.1 Summary of results.

As future prospects of the work performed in this thesis are concerned, an obvious continuation is to use these NCs in various applications, including fabrication of LSCs, solar cells, and photodetectors. The prerequisite for solar cells and photodetectors is the enhancement of charge transport. This can be achieved by post-synthetic surface modification leading to the replacement of long-chain organic ligands with short chain ligands, which should increase coupling between adjacent NCs. Routes for replacing the surface ligands on CZISe NCs have already been explored and efforts in fabricating solar cells and photodetectors

continue for this material. For LSCs, polymer composites of these NCs should be produced followed by their deposition on glass slides, which can act as the LSC and lead to enhanced PCE when combined with conventional Si-solar cells. Due to different absorption ranges of the synthesized NCs, they can be used as fluorophores in a tandem LSC that facilitates harvesting of a broader spectral range. Owing to the less toxic nature of the synthesized NCs, as compared to the best semiconductor emitters that contain Cd and Pb, one of the most appealing applications of these NCs is in biological imaging. NIR-emitting CZISe NCs and CZISe NPLs will be of particular use in this scenario due to a perfect match with a so-named biological window in the NIR spectral range. This would require the NCs to be soluble in aqueous media and can also be achieved through post-synthetic surface modification.

Bibliography

1.   Kovalenko, M. V.; Manna, L.; Cabot, A.; Hens, Z.; Talapin, D. V.; Kagan, C. R.; Klimov, V. I.; Rogach, A. L.; Reiss, P.; Milliron, D. J.; Guyot-Sionnnest, P.; Konstantatos, G.; Parak, W. J.; Hyeon, T.; Korgel, B. A.; Murray, C. B.; Heiss, W., Prospects of Nanoscience with Nanocrystals. *ACS Nano* **2015,** *9*, 1012–1057.

2.   Odom, T. W., Printable stained glass. *Nat. Nanotechnology* **2012,** *7*, 550.

3.   Ekimov, A. I.; Onushchenko, A. A., Quantum size effect in three-dimensional microscopic semiconductor crystals. *JETP Lett.* **1981,** *34*, 363.

4.   Efros, A. L., Interband Light Absorption in Semiconductor Spheres. *Sov. Phys. Semicond.* **1982,** *16*, 772-775.

5.   Itoh, T.; Kirihara, T., Excitons in CuCl Microcrystals Embedded in NaCl. *J. Lumin.* **1984,** *31-32*, 120-122.

6.   Rossetti, R.; Nakahara, S.; Brus, L. E., Quantum size effects in the redox potentials, resonance Raman spectra, and electronic spectra of CdS crystallites in aqueous solution. *J. Chem. Phys.* **1983,** *79*, 1086-1088.

7.   Brus, L., Electronic Wave Functions In Semiconductor Clusters: Experiment and Theory. *J. Phys. Chem.* **1986,** *90*, 2555-2560.

8.   Murray, C. B.; Norris, D. J.; Bawendi, M. G., Synthesis and Characterization of Nearly Monodisperse CdE (E= S, Se, Te) Semiconductor Nanocrystallites. *J. Am. Chem. Soc.* **1993,** *115*, 8706-8715.

9.   Talapin, D. V.; Jong-Soo Lee, J.-S.; Kovalenko, M. V.; Shevchenko, E. V., Prospects of Colloidal Nanocrystals for Electronic and Optoelectronic Applications. *Chem. Rev.* **2010,** *110*, 389-458.

10.   Song, J. H.; Jeong, S., Colloidal quantum dot based solar cells: from materials to devices. *Nano Converg.* **2017,** *4*, 21.

11.   Meinardi, F.; McDaniel, H.; Carulli, F.; Colombo, A.; Velizhanin, K. A.; Makarov, N. S.; Simonutti, R.; Klimov, V. I.; Brovelli, S., Highly efficient large-area colourless luminescent solar concentrators using heavy-metal-free colloidal quantum dots. *Nat. Nanotechnol.* **2015,** *10*, 878-885.

12.   Li, H.; Wu, K.; Lim, J.; Song, H. J.; Klimov, V. I., Doctor-blade deposition of quantum dots onto standard window glass for low-loss large-area luminescent solar concentrators. *Nat. Energy* **2016,** *1*, 1-9.

13. Zhong, H.; Bai, Z.; Zou, B., Tuning the Luminescence Properties of Colloidal I-III-VI Semiconductor Nanocrystals for Optoelectronics and Biotechnology Applications. *J. Phys. Chem. Lett.* **2012,** *3*, 3167-3175.

14. https://news.samsung.com/global/samsung-partners-with-emerging-german-artists-to-produce-the-origin-of-quantum-dot-exhibition-at-ifa.

15. Tang, J.; Kemp, K. W.; Hoogland, S.; Jeong, K. S.; Liu, H.; Levina, L.; Furukawa, M.; Wang, X.; Debnath, R.; Cha, D.; Chou, K. W.; Fischer, A.; Amassian, A.; Asbury, J. B.; Sargent, E. H., Colloidal-quantum-dot photovoltaics using atomic-ligand passivation. *Nat. Mater.* **2011,** *10*, 765-771.

16. Li, L.; Daou, T. J.; Texier, I.; Chi, T. T. K.; Quang Liem, N. Q.; Reiss, P., Highly Luminescent CuInS$_2$/ZnS Core/Shell Nanocrystals: Cadmium-Free Quantum Dots for In Vivo Imaging. *Chem. Mater.* **2009,** *21*, 2422-2429.

17. Bahmani Jalali, H.; De Trizio, L.; Manna, L.; Di Stasio, F., Indium arsenide quantum dots: an alternative to lead-based infrared emitting nanomaterials. *Chem. Soc. Rev.* **2022,** *51*, 9861-9881.

18. Alkadov, D.; Lefrancois, A.; Reiss, P., Ternary and Quaternary Metal Chalcogenide Nanocrystals: Synthesis, Properties and Applications. *J. Mater. Chem. C* **2013,** *1*, 3756-3776.

19. Sapsford, K. E.; Algar, W. R.; Berti, L.; Gemmill, K. B.; Casey, B. J.; Oh, E.; Stewart, M. H.; Medintz, I. L., Functionalizing Nanoparticles with Biological Molecules: Developing Chemistries that Facilitate Nanotechnology. *Chem. Rev.* **2013,** *113*, 1904-2074.

20. Lox, J. F. L.; Dang, Z.; Lê Anh, M.; Hollinger, E.; Lesnyak, V., Colloidal Cu–Zn–In–S-Based Disk-Shaped Nanocookies. *Chem. Mater.* **2019,** *31*, 2873-2883.

21. Lox, J. F. L.; Dang, Z.; Dzhagan, V. M.; Spittel, D.; Martín-García, B.; Moreels, I.; Zahn, D. R. T.; Lesnyak, V., Near-Infrared Cu–In–Se-Based Colloidal Nanocrystals via Cation Exchange. *Chem. Mater.* **2018,** *30*, 2607-2617.

22. Lesnyak, V.; George, C.; Genovese, A.; Prato, M.; Casu, A.; Ayyappan, S.; Scarpellini, A.; Manna, L., Alloyed Copper Chalcogenide Nanoplatelets via Partial Cation Exchange Reactions. *ACS Nano* **2014,** *8*, 8407–8418.

23. De Trizio, L.; Manna, L., Forging Colloidal Nanostructures via Cation Exchange Reactions. *Chem. Rev.* **2016,** *116*, 10852-10887.

24. Beberwyck, B. J.; Surendranath, Y.; Alivisatos, A. P., Cation Exchange: A Versatile Tool for Nanomaterials Synthesis. *J. Phys. Chem. C* **2013,** *117*, 19759-19770.

25.	Ithurria, S.;	Tessier, M. D.;	Mahler, B.;	Lobo, R. P.;	Dubertret, B.; Efros, A. L., Colloidal Nanoplatelets with Two-Dimensional Electronic Structure. *Nat. Mater.* **2011**, *10*, 936-941.

26.	Chang, J.; Waclawik, E. R., Colloidal semiconductor nanocrystals: controlled synthesis and surface chemistry in organic media. *RSC Adv.* **2014**, *4*, 23505-23527.

27.	Rao, M. S. R.; Singh, S., *Nanoscience and Nanotechnology: Fundamentals to Frontiers* Wiley 2013.

28.	Smith, A. M.; Nie, S., Semiconductor Nanocrystals: Structure, Properties, and Band Gap Engineering. *Acc. Chem. Res.* **2010**, *43*, 190-200.

29.	Alivisatos, A. P., Perspectives on the Physical Chemistry of Semiconductor Nanocrystals. *J. Phys. Chem.* **1996**, *100*, 13226-13239.

30.	Buhro, W. E.; Colvin, V. L., Semicondcutor Nanocrystals Shape matters. *Nat. Mater.* **2003,** *2*, 138-139.

31.	Seo, D.-K.; Hofmann, R., Direct and indirect band gap types in one-dimensional conjugated or stacked organic materials. *Theor. Chem. Acc.* **1999,** *102*, 23-32.

32.	Talapin, D. V. L., J. S.; Kovalenko, M. V.; Shevchenko, E.V., Prospects of Colloidal Nanocrystals for Electronic and Optoelectronic Applications. *Chem. Rev.* **2010,** *110*, 389-458.

33.	Boles, M. A.;	Ling, D.;	Hyeon, T.; Talapin, D. V., Erratum: The surface science of nanocrystals. *Nat. Mater.* **2016,** *15*, 364.

34.	Rogach, A. L.;	Talapin, D. V.;	Shevchenko, E. V.;	Kornowski, A.;	Haase, M.; Weller, H., Organization of Matter on Different Size Scales: Monodisperse Nanocrystals and Their Superstructures. *Adv. Funct. Mater.* **2002,** *12*, 653-664.

35.	Allen, P. M.; Bawendi, M. G., Ternary I-III-VI Quantum Dots Luminescent in the Red to Near-Infrared. *J. Am. Chem. Soc.* **2008,** *130*, 9240-9241.

36.	Berends, A. C.;	van der Stam, W.;	Hofmann, J. P.;	Bladt, E.;	Meeldijk, J. D.;	Bals, S.; de Mello Donega, C., Interplay between Surface Chemistry, Precursor Reactivity, and Temperature Determines Outcome of ZnS Shelling Reactions on $CuInS_2$ Nanocrystals. *Chem. Mater.* **2018,** *30*, 2400-2413.

37.	de Mello Donega, C., Synthesis and properties of colloidal heteronanocrystals. *Chem. Soc. Rev.* **2011,** *40*, 1512-1546.

38.	Steckel, J. S.;	Zimmer, J. P.;	Coe-Sullivan, S.;	Stott, N. E.;	Bulović, V.; Bawendi, M. G., Blue Luminescence from (CdS)ZnS Core–Shell Nanocrystals. *Angew. Chem.* **2004,** *116*, 2206-2210.

39.   Swart, I.; Sun, Z.; Vanmaekelbergh, D.; Liljeroth, P., Hole-induced electron transport through core-shell quantum dots: a direct measurement of the electron-hole interaction. *Nano Lett.* **2010,** *10*, 1931-1935.

40.   Ivanov, S. A.; Piryatinski, A.; Nanda, J.; Tretiak, S.; Zavadil, K. R.; Wallace, W. O.; Werder, D.; Klimov, V. I., Type-II Core/Shell CdS/ZnSe Nanocrystals: Synthesis, Electronic Structures, and Spectroscopic Properties. *J. Am. Chem. Soc.* **2007,** *129*, 11708-11719.

41.   Chin, P. T. K.; de Mello Donega, C.; Bavel, S. S. V.; Meskers, S. C. J.; Sommerdijk, N. A. J. M.; Janssen, R. A. J., Highly Luminescent CdTe/CdSe Colloidal Heteronanocrystals with Temperature-Dependent Emission Color. *J. Am. Chem. Soc.* **2007,** *129*, 14880-14886.

42.   Kim, S.; Fisher, B.; Eisler, H.-J.; Bawendi, M., Type-II Quantum Dots: CdTe/CdSe(Core/Shell) and CdSe/ZnTe(Core/Shell) Heterostructures. *J. Am. Chem. Soc.* **2003,** *125*, 11466-11467.

43.   Reiss, P.; Carriere, M.; Lincheneau, C.; Vaure, L.; Tamang, S., Synthesis of Semiconductor Nanocrystals, Focusing on Nontoxic and Earth-Abundant Materials. *Chem. Rev.* **2016,** *116*, 10731-10819.

44.   Yang, Y. A.; Wu, H.; Williams, K. R.; Cao, Y. C., Synthesis of CdSe and CdTe nanocrystals without precursor injection. *Angew. Chem. Int. Ed. Engl.* **2005,** *44*, 6712-6715.

45.   Chen, O.; Zhao, J.; Chauhan, V. P.; Cui, J.; Wong, C.; Harris, D. K.; Wei, H.; Han, H. S.; Fukumura, D.; Jain, R. K.; Bawendi, M. G., Compact High-Quality CdSe-CdS Core-Shell Nanocrystals with Narrow Emission Linewidths and Suppressed Blinking. *Nat. Mater.* **2013,** *12*, 445-451.

46.   Guo, Y.; Marchuk, K.; Sampat, S.; Abraham, R.; Fang, N.; Malko, A. V.; Vela, J., Unique Challenges Accompany Thick-Shell CdSe/nCdS (n > 10) Nanocrystal Synthesis. *J. Phys. Chem. C* **2012,** *116*, 2791-2800.

47.   Tan, T. T.; Selvan, S. T.; Zhao, L.; Gao, S.; Ying, J. Y., Size Control, Shape Evolution, and Silica Coating of Near-Infrared-Emitting PbSe Quantum Dots. *Chem. Mater.* **2007,** *19*, 3112-3117.

48.   Yan, L.; Shen, X.; Zhang, Y.; Zhang, T.; Zhang, X.; Feng, Y.; Yin, J.; Zhao, J.; Yu, W. W., Near-infrared light emitting diodes using PbSe quantum dots. *RSC Adv.* **2015,** *5*, 54109-54114.

49.   Zhong, H.; Zhou, Y.; Ye, M.; He, Y.; Ye, J.; He, C.; Yang, C.; Li, Y., Controlled Synthesis and Optical Properties of Colloidal Ternary Chalcogenide CuInS$_2$ Nanocrystals. *Chem. Mater.* **2008,** *20*, 6434-6443.

50.   Nose, K.; Omata, T.; Otsuka-Yao-Matsuo, S., Colloidal Synthesis of Ternary Copper Indium Diselenide Quantum Dots and Their Optical Properties. *J. Phys. Chem. Lett.* **2009,** *113*, 3455–3460.

51.   Cassette, E.; Pons, T.; Bouet, C.; Helle, M.; Bezdetnaya, L.; Marchal, F.; Dubertret, B., Synthesis and Characterization of Near-Infrared Cu−In−Se/ZnS Core/Shell Quantum Dots for In vivo Imaging. *Chem. Mater.* **2010,** *22*, 6117-6124.

52.   Kovalenko, M. V.; Protesescu, L.; Bodnarchuk, M. I., Properties and potential optoelectronic applications of lead halide perovskite nanocrystals. *Science* **2017,** *358*, 745-750.

53.   Owen, J., The coordination chemistry of nanocrystal surfaces. *Science* **2015,** *347*, 615-616.

54.   Anderson, N. C.; Hendricks, M. P.; Choi, J. J.; Owen, J. S., Ligand exchange and the stoichiometry of metal chalcogenide nanocrystals: spectroscopic observation of facile metal-carboxylate displacement and binding. *J. Am. Chem. Soc.* **2013,** *135*, 18536-18548.

55.   Pearson, R. G., Hard and Soft Acids and Bases. *J. Am. Chem. Soc.* **1963,** *85*, 3533-3539.

56.   Pearson, R. G., Absolute Electronegativity and Hardness: Application to Inorganic Chemistry. *Inorg. Chem.* **1988,** *27*, 734-740.

57.   Parr, R. G.; Pearson, R. G., Absolute Hardness: Companion Parameter to Absolute Electronegativity. *J. Am. Chem. Soc.* **1983,** *105*, 7512-7516.

58.   LaMer, V. K.; Dinegar, R. H., Theory, Production and Mechanism of Formation of Monodispersed Hydrosols. *J. Am. Chem. Soc.* **1950,** *72*, 4847-4854.

59.   Sugimoto, T., Underlying mechanisms in size control of uniform nanoparticles. *J. Colloid Interface Sci.* **2007,** *309*, 106-118.

60.   Ostwald, W., Studien über die Bildung und Umwandlung fester Körper. *J. Phys. Chem* **1897,** *22U*, 289-330.

61.   Peng, X.; Wickham, J.; Alivisatos, A. P., Kinetics of II-VI and III-V Colloidal Semiconductor Nanocrystal Growth: "Focusing" of Size Distributions. *J. Am. Chem. Soc.* **1998,** *120*, 5343-5344.

62.   Pan, D.; An, L.; Sun, Z.; Hou, W.; Yang, Y.; Yang, Z.; Lu, Y., Synthesis of Cu-In-S Ternary Nanocrystals with Tunable Structure and Composition. *J. Am. Chem. Soc.* **2008,** *130*, 5620–5621.

63.   Panthani, M. G.; Akhavan, V.; Goodfellow, B.; Schmidtke, J. P.; Dunn, L.; Dodabalapur, A.; Barbara, P. F.; Korgel, B. A., Synthesis of CuInS$_2$, CuInSe$_2$, and Cu(In$_x$Ga$_{1-x}$)Se$_2$ (CIGS) Nanocrystal "Inks" for Printable Photovoltaics. *J. Am. Chem. Soc.* **2008,** *130*, 16770–16777.

64.   Han, W.; Yi, L.; Zhao, N.; Tang, A.; Gao, M.; Tang, Z., Synthesis and Shape-Tailoring of Copper Sulfide/Indium Sulfide-Based Nanocrystals. *J. Am. Chem. Soc.* **2008,** *130*, 13152–13161.

65.   Tang, J.; Hinds, S.; Kelley, S. O.; Sarge, E. H., Synthesis of Colloidal CuGaSe$_2$, CuInSe$_2$, and Cu(InGa)Se$_2$ Nanoparticles. *Chem. Mater.* **2008,** *20*, 6906-6910.

66.   Lesnyak, V., Chemical Transformations of Colloidal Semiconductor Nanocrystals Advance Their Applications. *J. Phys. Chem. Lett.* **2021,** *12*, 12310-12322.

67.   Rivest, J. B.; Jain, P. K., Cation exchange on the nanoscale: an emerging technique for new material synthesis, device fabrication, and chemical sensing. *Chem. Soc. Rev.* **2013,** *42*, 89-96.

68.   Akkerman, Q. A.; Genovese, A.; George, C.; Prato, M.; Moreels, I.; Cabot, A.; Marras, S.; Curcio, A.; Scarpellini, A.; Pellegrino, T.; Manna, L.; Lesnyak, V., From Binary Cu$_2$S toTernary Cu-In-S and Quaternary Cu-In-Zn-S Nanocrystals with Tunable Composition via Partial Cation Exchange. *ACS Nano* **2015,** *9*, 521–531.

69.   Lesnyak, V.; Brescia, R.; Messina, G. C.; Manna, L., Cu Vacancies Boost Cation Exchange Reactions in Copper Selenide Nanocrystals. *J. Am. Chem. Soc.* **2015,** *137*, 9315-9323.

70.   Coughlan, C.; Ibanez, M.; Dobrozhan, O.; Singh, A.; Cabot, A.; Ryan, K. M., Compound Copper Chalcogenide Nanocrystals. *Chem. Rev.* **2017,** *117*, 5865-6109.

71.   Zhong, X.; Feng, Y.; Zhang, Y.; Gu, Z.; Zou, L., A facile route to violet- to orange-emitting Cd$_x$Zn$_{1-x}$Se alloy nanocrystals via cation exchange reaction. *Nanotechnology* **2007,** *18*, 385606.

72.   Jain, P. K.; Amirav, L.; Aloni, S.; Alivisatos, A. P., Nanoheterostructure Cation Exchange: Anionic Framework Conservation *J. Am. Chem. Soc.* **2010,** *132*, 9997–9999.

73.   Kovalenko, M. V.; Schaller, R. D.; Jarzab, D.; Loi, M. A.; Talapin, D. V., Inorganically functionalized PbS-CdS colloidal nanocrystals: integration into amorphous chalcogenide glass and luminescent properties. *J. Am. Chem. Soc.* **2012,** *134*, 2457-2460.

74.   Zhang, J.; Chernomordik, B. D.; Crisp, R. W.; Kroupa, D. M.; Miller, E. M.; Gao, J.; Beard, M. C., Preparation of Cd/Pb Chalcogenide Heterostructured Janus Particles via Controllable Cation Exchange. *ACS Nano* **2015,** *9*, 7151-7163.

75.   Luther, J. M.; Zheng, H.; Sadtler, B.; Alivisatos, A. P., Synthesis of PbS Nanorods and Other Ionic Nanocrystals of Complex Morphology by Sequential Cation Exchange Reactions. *J. Am. Chem. Soc.* **2009,** *131*, 16851–16857.

76.   Lee, D.; Kim, W. D.; Lee, S.; Bae, W. K.; Lee, S.; Lee, D. C., Direct Cd-to-Pb Exchange of CdSe Nanorods into PbSe/CdSe Axial Heterojunction Nanorods. *Chem. Mater.* **2015,** *27*, 5295-5304.

77.   Li, H.; Zanella, M.; Genovese, A.; Povia, M.; Falqui, A.; Giannini, C.; Manna, L., Sequential cation exchange in nanocrystals: preservation of crystal phase and formation of metastable phases. *Nano Lett.* **2011,** *11*, 4964-4970.

78.   Xia, Y.; Xiong, Y.; Lim, B.; Skrabalak, S. E., Shape-controlled synthesis of metal nanocrystals: simple chemistry meets complex physics? *Angew. Chem. Int. Ed. Engl.* **2009,** *48*, 60-103.

79.   Peng, X., Mechanisms for the Shape-Control and Shape-Evolution of Colloidal Semiconductor Nanocrystals. *Adv. Mater.* **2003,** *15*, 459-463.

80.   Chen, Y.; Fan, Z.; Zhang, Z.; Niu, W.; Li, C.; Yang, N.; Chen, B.; Zhang, H., Two-Dimensional Metal Nanomaterials: Synthesis, Properties, and Applications. *Chem. Rev.* **2018,** *118*, 6409-6455.

81.   Nasilowski, M.; Mahler, B.; Lhuillier, E.; Ithurria, S.; Dubertret, B., Two-Dimensional Colloidal Nanocrystals. *Chem. Rev.* **2016,** *116*, 10934-10982.

82.   Son, J. S.; Yu, J. H.; Kwon, S. G.; Lee, J.; Joo, J.; Hyeon, T., Colloidal synthesis of ultrathin two-dimensional semiconductor nanocrystals. *Adv. Mater.* **2011,** *23*, 3214-3219.

83.   Son, J. S.; Wen, X. D.; Joo, J.; Chae, J.; Baek, S. I.; Park, K.; Kim, J. H.; An, K.; Yu, J. H.; Kwon, S. G.; Choi, S. H.; Wang, Z.; Kim, Y. W.; Kuk, Y.; Hoffmann, R.; Hyeon, T., Large-scale soft colloidal template synthesis of 1.4 nm thick CdSe nanosheets. *Angew. Chem. Int. Ed. Engl.* **2009,** *48*, 6861-6864.

84.   Liu, Y. H.; Wang, F.; Wang, Y.; Gibbons, P. C.; Buhro, W. E., Lamellar assembly of cadmium selenide nanoclusters into quantum belts. *J. Am. Chem. Soc.* **2011,** *133*, 17005-17013.

85.   Bouet, C.; Mahler, B.; Nadal, B.; Abecassis, B.; Tessier, M. D.; Ithurria, S.; Xu, X.; Dubertret, B., Two-Dimensional Growth of CdSe Nanocrystals, from Nanoplatelets to Nanosheets. *Chem. Mater.* **2013,** *25*, 639-645.

86. Pedetti, S.; Nadal, B.; Lhuillier, E.; Mahler, B.; Bouet, C.; Abécassis, B.; Xu, X.; Dubertret, B., Optimized Synthesis of CdTe Nanoplatelets and Photoresponse of CdTe Nanoplatelets Films. *Chem. Mater.* **2013,** *25*, 2455-2462.

87. Son, J. S.; Park, K.; Kwon, S. G.; Yang, J.; Choi, M. K.; Kim, J.; Yu, J. H.; Joo, J.; Hyeon, T., Dimension-controlled synthesis of CdS nanocrystals: from 0D quantum dots to 2D nanoplates. *Small* **2012,** *8*, 2394-2402.

88. Buffard, A.; Nadal, B.; Heuclin, H.; Patriarche, G.; Dubertret, B., ZnS anisotropic nanocrystals using a one-pot low temperature synthesis. *New J. Chem.* **2015,** *39*, 90-93.

89. Du, Y.; Yin, Z.; Zhu, J.; Huang, X.; Wu, X. J.; Zeng, Z.; Yan, Q.; Zhang, H., A general method for the large-scale synthesis of uniform ultrathin metal sulphide nanocrystals. *Nat. Commun.* **2012,** *3*, 1177.

90. Penn, R. L.; Banfield, J. F., Imperfect Oriented Attachment: Dislocation Generation in Defect-Free Nanocrystals. *Science* **1998,** *281*, 969-970.

91. Zhang, J.; Huang, F.; Lin, Z., Progress of nanocrystalline growth kinetics based on oriented attachment. *Nanoscale* **2010,** *2*, 18-34.

92. Schliehe, C.; Juarez, B. H.; Pelletier, M.; Jander, S.; Greshnykh, D.; Nagel, M.; Meyer, A.; Foerster, S.; Kornowski, A.; Klinke, C.; Weller, H., Ultrathin PbS Sheets by Two-Dimensional Oriented Attachment. *Science* **2010,** *329*, 550-553.

93. Omata, T.; Nose, K.; Otsuka-Yao-Matsuo, S., Size dependent optical band gap of ternary I-III-VI$_2$ semiconductor nanocrystals. *J. Appl. Phys.* **2009,** *105*, 073106.

94. van der Stam, W.; Berends, A. C.; de Mello Donega, C., Prospects of Colloidal Copper Chalcogenide Nanocrystals. *ChemPhysChem* **2016,** *17*, 559-581.

95. Yarema, O.; Yarema, M.; Wood, V., Tuning the Composition of Multicomponent Semiconductor Nanocrystals: The Case of I–III–VI Materials. *Chem. Mater.* **2018,** *30*, 1446-1461.

96. Kolny-Olesiak, J.; Weller, H., Synthesis and Application of Colloidal CuInS$_2$ Semiconductor Nanocrystals. *ACS Appl. Mater. Interfaces* **2013,** *5*, 12221-12237.

97. McDaniel, H.; Fuke, N.; Pietryga, J. M.; Klimov, V. I., Engineered CuInSe$_x$S$_{2-x}$ Quantum Dots for Sensitized Solar Cells. *J. Phys. Chem. Lett.* **2013,** *4*, 355-361.

98. Panthani, M. G.; Stolle, C. J.; Reid, D. K.; Rhee, D. J.; Harvey, T. B.; Akhavan, V. A.; Yu, Y.; Korgel, B. A., CuInSe$_2$ Quantum Dot Solar Cells with High Open-Circuit Voltage. *J. Phys. Chem. Lett.* **2013,** *4*, 2030-2034.

99. Wu, K.; Li, H.; Klimov, V. I., Tandem luminescent solar concentrators based on engineered quantum dots. *Nat. Photonics* **2018,** *12*, 105-110.

100.   Bi, W.; Zhou, M.; Ma, Z.; Zhang, H.; Yu, J.; Xie, Y., CuInSe$_2$ Ultrathin Nanoplatelets: Novel Self-Sacrificial Template-Directed Synthesis and Application for Flexible Photodetectors. *Chem. Comm.* **2012,** *48*, 9162-9164.

101.   Guo, W.; Chen, N.; Tu, Y.; Dong, C.; Zhang, B.; Hu, C.; Chang, J., Synthesis of Zn-Cu-In-S/ZnS core/shell quantum dots with inhibited blue-shift photoluminescence and applications for tumor targeted bioimaging. *Theranostics* **2013,** *3*, 99-108.

102.   Castro, S. L.; Bailey, S. G.; Raffaelle, R. P.; Banger, K. K.; Hepp, A. F., Nanocrystalline Chalcopyrite Materials (CuInS$_2$ and CuInSe$_2$) via Low-Temperature Pyrolysis of Molecular Single-Source Precursors. *Chem. Mater.* **2003,** *15*, 3142-3147.

103.   Xie, R.; Rutherford, M.; Peng, X., Formation of High-Quality I-III-VI Semiconductor Nanocrystals by Tuning Relative Reactivity of Cationic Precursors. *J. Am. Chem. Soc.* **2009,** *131*, 5691-5697.

104.   Zhong, H.; Li, Y.; Ye, M.; Zhu, Z.; Zhou, Y.; Yang, C.; Li, Y., A Facile Route to Synthesize Chalcopyrite CuInSe$_2$ Nanocrystals in Non-Coordinating Solvent. *Nanotechnology* **2007,** *18*, 025602.

105.   Chen, B.; Zhong, H.; Zhang, W.; Tan, Z.; Li, Y.; Yu, C.; Zhai, T.; Bando, Y.; Yang, S.; Zou, B., Highly Emissive and Color-Tunable CuInS$_2$-Based Colloidal Semiconductor Nanocrystals: Off-Stoichiometry Effects and Improved Electroluminescence Performance. *Adv. Funct. Mater.* **2012,** *22*, 2081-2088.

106.   Song, W.-S.; Yang, H., Efficient White-Light-Emitting Diodes Fabricated from Highly Fluorescent Copper Indium Sulfide Core/Shell Quantum Dots. *Chem. Mater.* **2012,** *24*, 1961-1967.

107.   Witt, E.; Kolny-Olesiak, J., Recent developments in colloidal synthesis of CuInSe$_2$ nanoparticles. *Chem. Eur. J* **2013,** *19*, 9746-9753.

108.   Jara, D. H.; Stamplecoskie, K. G.; Kamat, P. V., Two Distinct Transitions in Cu(x)InS$_2$ Quantum Dots. Bandgap versus Sub-Bandgap Excitations in Copper-Deficient Structures. *J. Phys. Chem. Lett.* **2016,** *7*, 1452-1459.

109.   Zhong, H.; Lo, S. S.; Mirkovic, T.; Li, Y.; Ding, Y.; Li, Y.; Scholes, G. D., Noninjection Gram-Scale Synthesis of Monodisperse Pyramidal CuInS$_2$ Nanocrystals and Their Size-Dependent Properties. *ACS Nano* **2010,** *4*, 5253-5262.

110.   Norako, M. E.; Brutchey, R. L., Synthesis of Metastable Wurtzite CuInSe$_2$ Nanocrystals. *Chem. Mater.* **2010,** *22*, 1613-1615.

111.   Li, L.; Pandey, A.; Werder, D. J.; Khanal, B. P.; Pietryga, J. M.; Klimov, V. I., Efficient Synthesis of Highly Luminescent Copper Indium Sulfide-Based Core/Shell

Nanocrystals with Surprisingly Long-Lived Emission. *J. Am. Chem. Soc.* **2011,** *133*, 1176-1179.

112.   Zhang, H.; Fang, W.; Wang, W.; Qian, N.; Ji, X., Highly Efficient Zn-Cu-In-Se Quantum Dot-Sensitized Solar Cells through Surface Capping with Ascorbic Acid. *ACS Appl. Mater. Interfaces* **2019,** *11*, 6927-6936.

113.   van der Stam, W.; Berends, A. C.; Rabouw, F. T.; Willhammar, T.; Ke, X.; Meeldijk, J. D.; Bals, S.; de Mello Donega, C., Luminescent CuInS$_2$ Quantum Dots by Partial Cation Exchange in Cu$_{2-x}$S Nanocrystals. *Chem. Mater.* **2015,** *27*, 621-628.

114.   van der Stam, W.; Bladt, E.; Rabouw, F. T.; Bals, S.; de Mello Donega, C., Near-Infrared Emitting CuInSe$_2$/CuInS$_2$ Dot Core/Rod Shell Heteronanorods by Sequential Cation Exchange. *ACS Nano* **2015,** *9*, 11430–11438.

115.   De Trizio, L.; Prato, M.; Genovese, A.; Casu, A.; Povia, M.; Simonutti, R.; Alcocer, M. J. P.; D'Andrea, C.; Tassone, F.; Manna, L., Strongly Fluorescent Quaternary Cu–In–Zn–S Nanocrystals Prepared from Cu1-xInS2 Nanocrystals by Partial Cation Exchange. *Chem. Mater.* **2012,** *24*, 2400-2406.

116.   Berends, A. C.; Meeldijk, J. D.; van Huis, M. A.; de Mello Donega, C., Formation of Colloidal Copper Indium Sulfide Nanosheets by Two-Dimensional Self-Organization. *Chem. Mater.* **2017,** *29*, 10551-10560.

117.   Berends, A. C.; de Mello Donega, C., Ultrathin One- and Two-Dimensional Colloidal Semiconductor Nanocrystals: Pushing Quantum Confinement to the Limit. *J. Phys. Chem. Lett.* **2017,** *8*, 4077-4090.

118.   Kapuria, N.; Patil, N. N.; Ryan, K. M.; Singh, S., Two-dimensional copper based colloidal nanocrystals: synthesis and applications. *Nanoscale* **2022,** *14*, 2885-2914.

119.   Khan, A. H.; Brescia, R.; Polovitsyn, A.; Angeloni, I.; Martín-García, B.; Moreels, I., Near-Infrared Emitting Colloidal PbS Nanoplatelets: Lateral Size Control and Optical Spectroscopy. *Chem. Mater.* **2017,** *29*, 2883-2889.

120.   Tao, X.; Mafi, E.; Gu, Y., Synthesis and Ultrafast Carrier Dynamics of Single-Crystal Two-Dimensional CuInSe$_2$ Nanosheets. *J. Phys. Chem. Lett.* **2014,** *5*, 2857-2862.

121.   Galle, T.; Samadi Khoshkhoo, M.; Martin-Garcia, B.; Meerbach, C.; Sayevich, V.; Koitzsch, A.; Lesnyak, V.; Eychmüller, A., Colloidal PbSe Nanoplatelets of Varied Thickness with Tunable Optical Properties. *Chem. Mater.* **2019,** *31*, 3803-3811.

122.   Bouet, C.; Tessier, M. D.; Ithurria, S.; Mahler, B.; Nadal, B.; Dubertret, B., Flat Colloidal Semiconductor Nanoplatelets. *Chem. Mater.* **2013,** *25*, 1262-1271.

123.   Lhuillier, E.; Pedetti, S.; Ithurria, S.; Nadal, B.; Heuclin, H.; Dubertret, B., Two-Dimensional Colloidal Metal Chalcogenides Semiconductors: Synthesis, Spectroscopy, and Applications. *Acc. Chem. Res.* **2015,** *48*, 22-30.

124.   Koh, W. K.; Dandu, N. K.; Fidler, A. F.; Klimov, V. I.; Pietryga, J. M.; Kilina, S. V., Thickness-Controlled Quasi-Two-Dimensional Colloidal PbSe Nanoplatelets. *J. Am. Chem. Soc.* **2017,** *139*, 2152-2155.

125.   Liu, Y.; Yin, D.; Swihart, M. T., Valence Selectivity of Cation Incorporation into Covellite CuS Nanoplatelets. *Chem. Mater.* **2018,** *30*, 1399-1407.

126.   Shamraienko, V.; Spittel, D.; Hübner, R.; Samadi Khoshkhoo, M.; Weiß, N.; Georgi, M.; Borchert, K. B. L.; Schwarz, D.; Lesnyak, V.; Eychmüller, A., Cation Exchange on Colloidal Copper Selenide Nanosheets: A Route to Two-Dimensional Metal Selenide Nanomaterials. *J. Mater. Chem. C* **2021,** *9*, 16523-16535.

127.   Berends, A. C.; van der Stam, W.; Akkerman, Q. A.; Meeldijk, J. D.; van der Lit, J.; de Mello Donega, C., Anisotropic 2D $Cu_{2-x}Se$ Nanocrystals from Dodecaneselenol and Their Conversion to CdSe and $CuInSe_2$ Nanoparticles. *Chem. Mater.* **2018,** *30*, 3836-3846.

128.   Chen, B.; Chang, S.; Li, D.; Chen, L.; Wang, Y.; Chen, T.; Zou, B.; Zhong, H.; Rogach, A. L., Template Synthesis of $CuInS_2$ Nanocrystals from In_2S_3 Nanoplates and Their Application as Counter Electrodes in Dye-Sensitized Solar Cells. *Chem. Mater.* **2015,** *27*, 5949-5956.

129.   Yuan, Z.; Yang, L.; Han, D.; Sun, G.; Zhu, C.; Wang, Y.; Wang, Q.; Artemyev, M.; Tang, J., Synthesis and Optical Properties of In_2S_3-Hosted Colloidal Zn-Cu-In-S Nanoplatelets. *ACS Omega* **2021,** *6*, 18939-18947.

130.   Berends, A. C.; Mangnus, M. J. J.; Xia, C.; Rabouw, F. T.; de Mello Donega, C., Optoelectronic Properties of Ternary I-III-VI₂ Semiconductor Nanocrystals: Bright Prospects with Elusive Origins. *J. Phys. Chem. Lett.* **2019,** *10*, 1600-1616.

131.   Omata, T.; Nose, K.; Kurimoto, K.; Kita, M., Electronic transition responsible for size-dependent photoluminescence of colloidal $CuInS_2$ quantum dots. *J. Mater. Chem. C* **2014,** *2*.

132.   Leach, A. D.; Macdonald, J. E., Optoelectronic Properties of $CuInS_2$ Nanocrystals and Their Origin. *J. Phys. Chem. Lett.* **2016,** *7*, 572-583.

133.   Knowles, K. E.; Nelson, H. D.; Kilburn, T. B.; Gamelin, D. R., Singlet-Triplet Splittings in the Luminescent Excited States of Colloidal Cu(+):CdSe, Cu(+):InP, and $CuInS_2$ Nanocrystals: Charge Transfer Configurations and Self-Trapped Excitons. *J. Am. Chem. Soc.* **2015,** *137*, 13138-13147.

134.   Shabaev, A.; Mehl, M. J.; Efros, A. L., Energy band structure of CuInS$_2$ and optical spectra of CuInS$_2$ nanocrystals. *Phys. Rev. B* **2015,** *92*, 035431.

135.   Rice, W. D.; McDaniel, H.; Klimov, V. I.; Crooker, S. A., Magneto-Optical Properties of CuInS$_2$ Nanocrystals. *J. Phys. Chem. Lett.* **2014,** *5*, 4105-4109.

136.   Berends, A. C.; Rabouw, F. T.; Spoor, F. C.; Bladt, E.; Grozema, F. C.; Houtepen, A. J.; Siebbeles, L. D.; de Mello Donega, C., Radiative and Nonradiative Recombination in CuInS$_2$ Nanocrystals and CuInS$_2$-Based Core/Shell Nanocrystals. *J. Phys. Chem. Lett.* **2016,** *7*, 3503-3509.

137.   Pinchetti, V.; Lorenzon, M.; McDaniel, H.; Lorenzi, R.; Meinardi, F.; Klimov, V. I.; Brovelli, S., Spectro-Electrochemical Probing of Intrinsic and Extrinsic Processes in Exciton Recombination in I-III-VI$_2$ Nanocrystals. *Nano Lett.* **2017,** *17*, 4508-4517.

138.   Brovelli, S.; Galland, C.; Viswanatha, R.; Klimov, V. I., Tuning radiative recombination in Cu-doped nanocrystals via electrochemical control of surface trapping. *Nano Lett.* **2012,** *12*, 4372-4379.

139.   Fuhr, A. S.; Yun, H. J.; Makarov, N. S.; Li, H.; McDaniel, H.; Klimov, V. I., Light Emission Mechanisms in CuInS$_2$ Quantum Dots Evaluated by Spectral Electrochemistry. *ACS Photonics* **2017,** *4*, 2425-2435.

140.   Whitham, P. J.; Marchioro, A.; Knowles, K. E.; Kilburn, T. B.; Reid, P. J.; Gamelin, D. R., Single-Particle Photoluminescence Spectra, Blinking, and Delayed Luminescence of Colloidal CuInS$_2$ Nanocrystals. *J. Phys. Chem. C* **2016,** *120*, 17136-17142.

141.   Zang, H.; Li, H.; Makarov, N. S.; Velizhanin, K. A.; Wu, K.; Park, Y. S.; Klimov, V. I., Thick-Shell CuInS$_2$/ZnS Quantum Dots with Suppressed "Blinking" and Narrow Single-Particle Emission Line Widths. *Nano Lett.* **2017,** *17*, 1787-1795.

142.   Rosen, E. L.; Buonsanti, R.; Llordes, A.; Sawvel, A. M.; Milliron, D. J.; Helms, B. A., Exceptionally mild reactive stripping of native ligands from nanocrystal surfaces by using Meerwein's salt. *Angew. Chem. Int. Ed. Engl.* **2012,** *51*, 684-689.

143.   Meerbach, C.; Tietze, R.; Voigt, S.; Sayevich, V.; Dzhagan, V. M.; Erwin, S. C.; Dang, Z.; Selyshchev, O.; Schneider, K.; Zahn, D. R. T.; Lesnyak, V.; Eychmüller, A., Brightly Luminescent Core/Shell Nanoplatelets with Continuously Tunable Optical Properties. *Adv. Optical Mater.* **2019,** *7*, 1801478.

144.   Park, K. H.; Jang, K.; Son, S. U., Synthesis, Optical Properties, and Self-Assembly of Ultrathin Hexagonal In$_2$S$_3$ Nanoplates. *Angew. Chem. Int. Ed. Engl.* **2006,** *45*, 4608-4612.

145. Yarema, O.; Bozyigit, D.; Rousseau, I.; Nowack, L.; Yarema, M.; Heiss, W.; Wood, V., Highly Luminescent, Size- and Shape-Tunable Copper Indium Selenide Based Colloidal Nanocrystals. *Chem. Mater.* **2013,** *25*, 3753-3757.

146. Zhong, H.; Wang, Z.; Bovero, E.; Lu, Z.; van Veggel, F. C. J. M.; Scholes, G. D., Colloidal CuInSe$_2$ Nanocrystals in the Quantum Confinement Regime: Synthesis, Optical Properties, and Electroluminescence. *J. Phys. Chem. C* **2011,** *115*, 12396-12402.

147. Du, J.; Du, Z.; Hu, J. S.; Pan, Z.; Shen, Q.; Sun, J.; Long, D.; Dong, H.; Sun, L.; Zhong, X.; Wan, L. J., Zn-Cu-In-Se Quantum Dot Solar Cells with a Certified Power Conversion Efficiency of 11.6%. *J. Am. Chem. Soc.* **2016,** *138*, 4201-4209.

148. Zhou, Y.; Benetti, D.; Fan, Z.; Zhao, H.; Ma, D.; Govorov, A. O.; Vomiero, A.; Rosei, F., Near Infrared, Highly Efficient Luminescent Solar Concentrators. *Adv. Energy Mater.* **2016,** *6*, 1501913- 1501920.

149. Koo, B.; Patel, R. N.; Korgel, B. A., Synthesis of CuInSe2 Nanocrystals with Trigonal Pyramidal Shape. *J. Am. Chem. Soc.* **2009,** *131*, 3134-3135.

150. McDaniel, H.; Koposov, A. Y.; Draguta, S.; Makarov, N. S.; Pietryga, J. M.; Klimov, V. I., Simple yet Versatile Synthesis of CuInSe$_x$S$_{2-x}$ Quantum Dots for Sunlight Harvesting. *J. Phys. Chem. C* **2014,** *118*, 16987-16994.

151. Gupta, S.; Kershaw, S. V.; Rogach, A. L., 25th anniversary article: Ion exchange in colloidal nanocrystals. *Adv. Mater.* **2013,** *25*, 6923-6943.

152. Lide, D. R., *CRC Handbook of Chemistry and Physics, 84th ed*. CRC Press: Boca Raton: 2003-2004.

153. Llorente, V. B.; Dzhagan, V. M.; Gaponik, N.; Iglesias, R. A.; Zahn, D. R. T.; Lesnyak, V., Electrochemical Tuning of Localized Surface Plasmon Resonance in Copper Chalcogenide Nanocrystals. *J. Phys. Chem. C* **2017,** *121*, 18244-18253.

154. Samadi Khoshkhoo, M.; Lox, J. F. L.; Koitzsch, A.; Lesny, H.; Joseph, Y.; Lesnyak, V.; Eychmüller, A., Highly Conductive Copper Selenide Nanocrystal Thin Films for Advanced Electronics. *ACS Appl. Electron. Mater.* **2019,** *1*, 1560-1569.

155. Wolf, A.; Kodanek, T.; Dorfs, D., Tuning the LSPR in copper chalcogenide nanoparticles by cation intercalation, cation exchange and metal growth. *Nanoscale* **2015,** *7*, 19519-19527.

156. Dorfs, D.; Hartling, T.; Miszta, K.; Bigall, N. C.; Kim, M. R.; Genovese, A.; Falqui, A.; Povia, M.; Manna, L., Reversible tunability of the near-infrared valence band plasmon resonance in Cu$_{(2-x)}$Se nanocrystals. *J. Am. Chem. Soc.* **2011,** *133*, 11175-11180.

157.   Williams, M. L., Handbook of Chemistry and Physics. *Occup. Environ. Med* **1996,** *53*, 504-504.

158.   Zhao, Y.; Pan, H.; Lou, Y.; Qiu, X.; Zhu, J.; Burda, C., Plasmonic Cu2-xS Nanocrystals: Optical and Structural Properties of Copper-Deficient Copper(I) Sulfides. *J. Am. Chem. Soc.* **2009,** *131*, 4253-4261.

159.   De Trizio, L.; Gaspari, R.; Bertoni, G.; Kriegel, I.; Moretti, L.; Scotognella, F.; Maserati, L.; Zhang, Y.; Messina, G. C.; Prato, M.; Marras, S.; Cavalli, A.; Manna, L., Cu3-x P Nanocrystals as a Material Platform for Near-Infrared Plasmonics and Cation Exchange Reactions. *Chem. Mater.* **2015,** *27*, 1120-1128.

160.   Hinterding, S. O. M.; Mangnus, M. J. J.; Prins, P. T.; Jobsis, H. J.; Busatto, S.; Vanmaekelbergh, D.; de Mello Donega, C.; Rabouw, F. T., Unusual Spectral Diffusion of Single CuInS2 Quantum Dots Sheds Light on the Mechanism of Radiative Decay. *Nano Lett.* **2021,** *21*, 658-665.

161.   Park, J.; Kim, S. W., CuInS$_2$/ZnS Core/Shell Quantum Dots by Cation Exchange and their Blue-Shifted Photoluminescence. *J. Mater. Chem. C* **2011,** *21*, 3745-3750.

162.   Knowles, K. E.; Hartstein, K. H.; Kilburn, T. B.; Marchioro, A.; Nelson, H. D.; Whitham, P. J.; Gamelin, D. R., Luminescent Colloidal Semiconductor Nanocrystals Containing Copper: Synthesis, Photophysics, and Applications. *Chem. Rev.* **2016,** *116*, 10820-10851.

163.   Liu, H.; Cai, P.; McHugh, K. J.; Perkinson, C. F.; Li, L.; Wang, S.; Wang, W.; Jiao, M.; Luo, X.; Jing, L., Aqueous synthesis of bright near-infrared-emitting Zn-Cu-In-Se quantum dots for multiplexed detection of tumor markers. *Nano Res.* **2022,** *15*, 8351-8359.

164.   Galle, T.; Spittel, D.; Weiss, N.; Shamraienko, V.; Decker, H.; Georgi, M.; Hubner, R.; Metzkow, N.; Steinbach, C.; Schwarz, D.; Lesnyak, V.; Eychmuller, A., Simultaneous Ligand and Cation Exchange of Colloidal CdSe Nanoplatelets toward PbSe Nanoplatelets for Application in Photodetectors. *J. Phys. Chem. Lett.* **2021,** *12*, 5214-5220.

165.   Sonntag, L.; Shamraienko, V.; Fan, X.; Samadi Khoshkhoo, M.; Kneppe, D.; Koitzsch, A.; Gemming, T.; Hiekel, K.; Leo, K.; Lesnyak, V.; Eychmuller, A., Colloidal PbS nanoplatelets synthesized via cation exchange for electronic applications. *Nanoscale* **2019,** *11*, 19370-19379.

166.   Wang, H.; Butler, D. J.; Straus, D. B.; Oh, N.; Wu, F.; Guo, J.; Xue, K.; Lee, J. D.; Murray, C. B.; Kagan, C. R., Air-Stable CuInSe$_2$ Nanocrystal Transistors and Circuits via Post-Deposition Cation Exchange. *ACS Nano* **2019,** *13*, 2324-2333.

167.   Riedinger, A.; Ott, F. D.; Mule, A.; Mazzotti, S.; Knusel, P. N.; Kress, S. J. P.; Prins, F.; Erwin, S. C.; Norris, D. J., An Intrinsic Growth Instability in Isotropic Materials Leads to Quasi-Two-Dimensional Nanoplatelets. *Nat. Mater.* **2017,** *16*, 743-748.

168.   Vikulov, S.; Di Stasio, F.; Ceseracciu, L.; Saldanha, P. L.; Scarpellini, A.; Dang, Z.; Krahne, R.; Manna, L.; Lesnyak, V., Fully Solution-Processed Conductive Films Based on Colloidal Copper Selenide Nanosheets for Flexible Electronics. *Adv. Funct. Mater.* **2016,** *26*, 3670-3677.

169.   Almeida, G.; Dogan, S.; Bertoni, G.; Giannini, C.; Gaspari, R.; Perissinotto, S.; Krahne, R.; Ghosh, S.; Manna, L., Colloidal Monolayer β-In_2Se_3 Nanosheets with High Photoresponsivity. *J. Am. Chem. Soc.* **2017,** *139*, 3005-3011.

170.   Yang, Y.; Qin, H.; Jiang, M.; Lin, L.; Fu, T.; Dai, X.; Zhang, Z.; Niu, Y.; Cao, H.; Jin, Y.; Zhao, F.; Peng, X., Entropic Ligands for Nanocrystals: From Unexpected Solution Properties to Outstanding Processability. *Nano Lett.* **2016,** *16*, 2133-2138.

171.   Yang, Y.; Qin, H.; Peng, X., Intramolecular Entropy and Size-Dependent Solution Properties of Nanocrystal-Ligands Complexes. *Nano Lett.* **2016,** *16*, 2127-2132.

172.   Liu, H.; Jin, Z.; Wang, W.; Li, J., Monodispersed Sphalerite $CuInSe_2$ Nanoplates and Highly (112) Oriented Chalcopyrite Thin Films by Nanoplates Ink Coating. *CrystEngComm* **2011,** *13*, 7198-7201.

173.   Bai, X.; Purcell-Milton, F.; Gun'ko, Y. K., Optical Properties, Synthesis, and Potential Applications of Cu-Based Ternary or Quaternary Anisotropic Quantum Dots, Polytypic Nanocrystals, and Core/Shell Heterostructures. *Nanomaterials* **2019,** *9*, 85.

174.   Li, X.; Tu, D.; Yu, S.; Song, X.; Lian, W.; Wei, J.; Shang, X.; Li, R.; Chen, X., Highly Efficient Luminescent I-III-VI Semiconductor Nanoprobes Based on Template-Synthesized $CuInS_2$ Nanocrystals. *Nano Res.* **2019,** *12*, 1804-1809.

175.   Slejko, E. A.; Sayevich, V.; Cai, B.; Gaponik, N.; Lughi, V.; Lesnyak, V.; Eychmüller, A., Precise Engineering of Nanocrystal Shells via Colloidal Atomic Layer Deposition. *Chem. Mater.* **2017,** *29*, 8111-8118.

176.   Xia, C.; Wu, W.; Yu, T.; Xie, X.; van Oversteeg, C.; Gerritsen, H. C.; de Mello Donega, C., Size-Dependent Band-Gap and Molar Absorption Coefficients of Colloidal $CuInS_2$ Quantum Dots. *ACS Nano* **2018,** *12*, 8350-8361.

177.   Zhang, W.; Lou, Q.; Ji, W.; Zhao, J.; Zhong, X., Color-Tunable Highly Bright Photoluminescence of Cadmium-Free Cu-Doped Zn–In–S Nanocrystals and Electroluminescence. *Chem. Mater.* **2013,** *26*, 1204-1212.

178. Fuhr, A.; Yun, H. J.; Crooker, S. A.; Klimov, V. I., Spectroscopic and Magneto-Optical Signatures of Cu(1+) and Cu(2+) Defects in Copper Indium Sulfide Quantum Dots. *ACS Nano* **2020,** *14*, 2212-2223.

179. Ithurria, S.; Bousquet, G.; Dubertret, B., Continuous Transition from 3D to 1D Confinement Observed During the Formation of CdSe Nanoplatelets. *J. Am. Chem. Soc.* **2011,** *133*, 3070-3077.

180. Bouet, C.; Laufer, D.; Mahler, B.; Nadal, B.; Heuclin, H.; Pedetti, S.; Patriarche, G.; Dubertret, B., Synthesis of Zinc and Lead Chalcogenide Core and Core/Shell Nanoplatelets Using Sequential Cation Exchange Reactions. *Chem. Mater.* **2014,** *26*, 3002-3008.

181. Ma, Y.; Zhang, Y.; Yu, W. W., Near infrared emitting quantum dots: synthesis, luminescence properties and applications. *J. Mater. Chem. C* **2019,** *7*, 13662-13679.

182. Deng, D.; Zhang, W.; Chen, X.; Liu, F.; Zhang, J.; Gu, Y.; Hong, J., Facile Synthesis of High-Quality, Water-Soluble, Near-Infrared-Emitting PbS Quantum Dots. *Eur. J. Inorg. Chem.* **2009,** *23*, 3440-3446.

183. Kovalenko, M. V.; Kaufmann, E.; Pachinger, D.; Roither, J.; Huber, M.; Stangl, J.; Hesser, G.; Schäffler, F.; Heiss, W., Colloidal HgTe Nanocrystals with Widely Tunable Narrow Band Gap Energies: From Telecommunications to Molecular Vibrations. *J. Am. Chem. Soc.* **2006,** *128*, 3516-3517.

184. Jia, Y.; Liu, H.; Cai, P.; Liu, X.; Wang, L.; Ding, L.; Xu, G.; Wang, W.; Jiao, M.; Luo, X., Near-infrared emitting Cu-In-Se/ZnS core/shell quantum dots: aqueous synthesis and sulfur source effects. *Chem. Commun.* **2021,** *57*, 4178-4181.

185. Tong, X.; Kong, X.-T.; Zhou, Y.; Navarro-Pao, F.; Selopal, G. S.; Sun, S.; Govorov, A. O.; Zhao, H.; Wang, Z. M.; Rosei, F., Near-Infrared, Heavy Metal-Free Colloidal "Giant" Core/Shell Quantum Dots. *Adv. Energy Mater.* **2018,** *8*, 1701432.

186. Liu, L.; Dong, J.; Huang, J.; Nie, A.; Zhai, K.; Xiang, J.; Wang, B.; Wen, F.; Mu, C.; Zhao, Z.; Gong, Y.; Tian, Y.; Liu, Z., Atomically Resolving Polymorphs and Crystal Structures of In_2Se_3. *Chem. Mater.* **2019,** *31*, 10143-10149.

187. Tao, X.; Gu, Y., Crystalline-crystalline phase transformation in two-dimensional In_2Se_3 thin layers. *Nano Lett.* **2013,** *13*, 3501-3505.

188. Li, J.; Li, H.; Niu, X.; Wang, Z., Low-Dimensional In_2Se_3 Compounds: From Material Preparations to Device Applications. *ACS Nano* **2021,** *15*, 18683-18707.

189.   Qu, S.; Yuan, X.; Li, Y.; Li, X.; Zhou, X.; Xue, X.; Zhang, K.; Xu, J.; Yuan, C., Aqueous synthesis of composition-tuned defects in CuInSe$_2$ nanocrystals for enhanced visible-light photocatalytic H$_2$ evolution. *Nanoscale Adv.* **2021,** *3*, 2334-2342.

190.   Martinez, B.; Livache, C.; Goubet, N.; Izquierdo, E.; Silly, M., G.; Ithurria, S.; Lhuillier, E., Optoelectronics Using 2D Colloidal Nanocrystals from Wide Band Gap to Narrow Band Gap Materials. *Phys. Status Solidi C* **2017,** *14*, 1700138.

191.   Park, J.; Dvoracek, C.; Lee, K. H.; Galloway, J. F.; Bhang, H. E.; Pomper, M. G.; Searson, P. C., CuInSe/ZnS core/shell NIR quantum dots for biomedical imaging. *Small* **2011,** *7*, 3148-52.

List of Publications

1. **Bora, A**.; Prudnikau, A.; Fu, N.; Hübner, R.; Borchert, K. B. L.; Schwarz, D.; Gaponik, N.; Lesnyak, V. Seed-Mediated Synthesis of Photoluminescent Cu–Zn–In–S Nanoplatelets. *Chem. Mater.* 2022, 34, 20, 9251–9260.

DOI: https://doi.org/10.1021/acs.chemmater.2c02500

2. **Bora, A**.; Lox, J.; Hübner, R.; Weiß, N.; Jalali, H. B.; Stasio, F.D.; Steinbach, C. Gaponik, N.; Lesnyak, V. Composition Dependent Optical Properties of Cu-Zn-In-Se Colloidal Nanocrystals Synthesized via Cation Exchange. *Accepted, Chem. Mater.*

DOI: https://doi.org/10.1021/acs.chemmater.3c00538

3. **Bora, A.;** Fu, N.; Prudnikau, A.; Hübner; Jalali, H. B.; Stasio, F.D.; Gaponik, N.; Lesnyak, V. Cu-Zn-In-Se Nanoplatelets with Narrow Near Infrared Photoluminescence. *In preparation*

4. Li, J.; Hübner, R.; Deconinck, M.; **Bora, A**.; Göbel, M.; Schwarz, D.; Chen, G.; Wang, G.; Yang, S.; Vaynzof, Y.; Gaponik, N.; Lesnyak, V. Colloidal Rhenium-Molybdenum Sulfide Alloy Nanomaterials with Enlarged Interlayer Distance for Hydrogen Evolution Reaction. *Under review.*

Erklarung

Hiermit versichere ich, dass ich die vorliegende Arbeit ohne unzulässige Hilfe Dritter und ohne Benutzung anderer als der angegebenen Hilfsmittel angefertigt habe; die aus fremden Quellen direkt oder indirekt übernommenen Gedanken sind als solche kenntlich gemacht. Die Arbeit wurde bisher weder im Inland noch im Ausland in gleicher oder ähnlicher Form einer anderen Prüfungsbehörde vorgelegt.

Die vorliegende Dissertation wurde in der Zeit von October 2019 bis Mai 2023 an der Professur für Physikalische Chemie der Fachrichtung Chemie & Lebensmittelchemie der Fakultät Mathematik und Naturwissenschaften an der Technischen Universität Dresden unter wissenschaftlicher Betreuung von Prof. Dr. Nikolai Gaponik und Dr. Vladimir Lesnyak angefertigt.

Dresden, 27.07.2023

—————————

Ankita Bora